Fermi National Accelerator Laboratory

FERMILAB-Pub-90/229-E
[E-741/CDF]

A Measurement of $\sigma \cdot B(W \rightarrow e\,\nu)$ and $\sigma \cdot B(Z^0 \rightarrow e^+ e^-)$ in $\bar{p}p$ Collisions at $\sqrt{s}$=1800 GeV *

The CDF Collaboration
Fermi National Accelerator Laboratory
P.O. Box 500
Batavia, Illinois 60510

November 9, 1990

* Submitted to *Phys. Rev. D.*

CDF/PUB/ELECTROWEAK/PUBLIC/1276
Fermilab-PUB-90/229-E

A measurement of $\sigma \cdot B(W \rightarrow e\,\nu)$ and $\sigma \cdot B(Z^0 \rightarrow e^+e^-)$ in $\bar{p}p$ collisions at $\sqrt{s} = 1800$ GeV

F. Abe,[8] D. Amidei,[4] G. Apollinari,[11] M. Atac,[4] P. Auchincloss,[14] A. R. Baden,[6] A. Bamberger,[4],[a] A. Barbaro-Galtieri,[9] V. E. Barnes,[12] F. Bedeschi,[11] S. Behrends,[2] S. Belforte,[11] G. Bellettini,[11] J. Bellinger,[18] J. Bensinger,[2] A. Beretvas,[4] J. P. Berge,[4] S. Bertolucci,[5] S. Bhadra,[7] M. Binkley,[4] R. Blair,[1] C. Blocker,[2] A. W. Booth,[4] G. Brandenburg,[6] D. Brown,[6] E. Buckley,[14] A. Byon,[12] K. L. Byrum,[18] C. Campagnari,[3] M. Campbell,[3] R. Carey,[6] W. Carithers,[9] D. Carlsmith,[18] J. T. Carroll,[4] R. Cashmore,[4],[b] F. Cervelli,[11] K. Chadwick,[4] G. Chiarelli,[5] W. Chinowsky,[9] S. Cihangir,[4] A. G. Clark,[4] D. Connor,[10] M. Contreras,[2] J. Cooper,[4] M. Cordelli,[5] D. Crane,[4] M. Curatolo,[5] C. Day,[4] S. Dell'Agnello,[11] M. Dell'Orso,[11] L. Demortier,[2] P. F. Derwent,[3] T. Devlin,[14] D. DiBitonto,[15] R. B. Drucker,[9] K. Einsweiler,[9] J. E. Elias,[4] R. Ely,[9] S. Errede,[7] B. Esposito,[5] B. Flaugher,[14] G. W. Foster,[4] M. Franklin,[6] J. Freeman,[4] H. Frisch,[3] Y. Fukui,[8] Y. Funayama,[16] A. F. Garfinkel,[12] A. Gauthier,[7] S. Geer,[6] P. Giannetti,[11] N. Giokaris,[13] P. Giromini,[5] L. Gladney,[10] M. Gold,[9] K. Goulianos,[13] H. Grassmann,[11] C. Grosso-Pilcher,[3] C. Haber,[9] S. R. Hahn,[4] R. Handler,[18] K. Hara,[16] R. M. Harris,[9] J. Hauser,[3] T. Hessing,[15] R. Hollebeek,[10] L. Holloway,[7] P. Hu,[14] B. Hubbard,[9] B. T. Huffman,[12] R. Hughes,[10] P. Hurst,[7] J. Huth,[4] M. Incagli,[11] T. Ino,[16] H. Iso,[16] H. Jensen,[4] C. P. Jessop,[6] R. P. Johnson,[4] U. Joshi,[4] R. W. Kadel,[4] T. Kamon,[15] S. Kanda,[16] D. A. Kardelis,[7] I. Karliner,[7] E. Kearns,[6] R. Kephart,[4] P. Kesten,[2] R. M. Keup,[7] H. Keutelian,[7] S. Kim,[16] L. Kirsch,[2] K. Kondo,[16] S. E. Kuhlmann,[1] E. Kuns,[14] A. T. Laasanen,[12] J. I. Lamoureux,[18] S. Leone,[11] W. Li,[1] T. M. Liss,[7] N. Lockyer,[10] C. B. Luchini,[7] P. Maas,[4] M. Mangano[11] J. P. Marriner,[4] R. Markeloff,[18] L. A. Markosky,[18] R. Mattingly,[2] P. McIntyre,[15] A. Menzione,[11] T. Meyer,[15] S. Mikamo,[8] M. Miller,[3] T. Mimashi,[16] S. Miscetti,[5] M. Mishina,[8] S. Miyashita,[16] Y. Morita,[16] S. Moulding,[2] A. Mukherjee,[4] L. F. Nakae,[2] I. Nakano,[16] C. Nelson,[4] C. Newman-Holmes,[4] J. S. T. Ng,[6] M. Ninomiya,[16] L. Nodulman,[1] S. Ogawa,[16] R. Paoletti,[11] A. Para,[4] E. Pare,[6] J. Patrick,[4] T. J. Phillips,[6] R. Plunkett,[4] L. Pondrom,[18] J. Proudfoot,[1] G. Punzi,[11] D. Quarrie,[4] K. Ragan,[10] G. Redlinger,[3] J. Rhoades,[18] M. Roach,[17] F. Rimondi,[4],[c] L. Ristori,[11] T. Rohaly,[10] A. Roodman,[3] A. Sansoni,[5] R. D. Sard,[7] A. Savoy-Navarro,[4] V. Scarpine,[7] P. Schlabach,[7] E. E. Schmidt,[4] M. H. Schub,[12] R. Schwitters,[6] A. Scribano,[11] S. Segler,[4] Y. Seiya,[16] M. Sekiguchi,[16] P. Sestini,[11] M. Shapiro,[6] M. Sheaff,[18] M. Shochet,[3] J. Siegrist,[9] P. Sinervo,[10] J. Skarha,[18] K. Sliwa,[17] D. A. Smith,[11] F. D. Snider,[3] R. St. Denis,[6] A. Stefanini,[11] R. L. Swartz, Jr.,[7] M. Takano,[16] K. Takikawa,[16] S. Tarem,[2] D. Theriot,[4] M. Timko,[15] P. Tipton,[9] S. Tkaczyk,[4] A. Tollestrup,[4] G. Tonelli,[11] J. Tonnison,[12] W. Trischuk,[6] Y. Tsay,[3] F. Ukegawa,[16] D. Underwood,[1] R. Vidal,[4] R. G. Wagner,[1] R. L. Wagner,[4] J. Walsh,[10] T. Watts,[14] R. Webb,[15] C. Wendt,[18] W. C. Wester, III,[9] T. Westhusing,[11] S. N. White,[13] A. B. Wicklund,[1] H. H. Williams,[10] B. L. Winer,[9] A. Yagil,[4] A. Yamashita,[16] K. Yasuoka,[16] G. P. Yeh,[4] J. Yoh,[4] M. Yokoyama,[16] J. C. Yun,[4] F. Zetti[11]

[1] *Argonne National Laboratory, Argonne, Illinois 60439*

[2] *Brandeis University, Waltham, Massachusetts 02254*

[3] *University of Chicago, Chicago, Illinois 60637*

[4] *Fermi National Accelerator Laboratory, Batavia, Illinois 60510*

[5] *Laboratori Nazionali di Frascati, Istituto Nazionale di Fisica Nucleare, Frascati, Italy*

[6] *Harvard University, Cambridge, Massachusetts 02138*

[7] *University of Illinois, Urbana, Illinois 61801*

[8] *National Laboratory for High Energy Physics (KEK), Tsukuba, Ibaraki 305, Japan*

[9] *Lawrence Berkeley Laboratory, Berkeley, California 94720*

[10] *University of Pennsylvania, Philadelphia, Pennsylvania 19104*

[11] *Istituto Nazionale di Fisica Nucleare, University and Scuola Normale Superiore of Pisa, I-56100 Pisa, Italy*

[12] *Purdue University, West Lafayette, Indiana 47907*

[13] *Rockefeller University, New York, New York 10021*

Submitted to Phys. Rev. D, November 9, 1990.

[14] *Rutgers University, Piscataway, New Jersey 08854*
[15] *Texas A&M University, College Station, Texas 77843*
[16] *University of Tsukuba, Tsukuba, Ibaraki 305, Japan*
[17] *Tufts University, Medford, Massachusetts 02155*
[18] *University of Wisconsin, Madison, Wisconsin 53706*

Abstract

An analysis of high transverse momentum electrons using data from the Collider Detector at Fermilab in $\bar{p}p$ collisions at $\sqrt{s} = 1800$ GeV yields values of the production cross section times branching ratio for W and Z^0 bosons of $\sigma(\bar{p}p \rightarrow W\ X \rightarrow e\nu X) = 2.19 \pm 0.04$ (stat) ± 0.21 (sys) nb and $\sigma(\bar{p}p \rightarrow Z^0 X \rightarrow e^+e^- X) = 0.209 \pm 0.013$ (stat) ± 0.017 (sys) nb. Detailed descriptions of the CDF electron identification, background, efficiency, and acceptance are included. Theoretical predictions of the cross sections that include a mass for the top quark larger than the W mass, current values of the W and Z^0 masses, and higher order QCD corrections are in good agreement with these measured values.
PACS numbers: 13.38+c,14.80.Er

1 Introduction

In this paper we present measurements of the production of W bosons with subsequent decay to eν ($\sigma \cdot B(W \rightarrow e\ \nu)$), and the production of Z^0 bosons with decay into e^+e^- ($\sigma \cdot B(Z^0 \rightarrow\ e^+e^-)$), in $\sqrt{s} = 1800$ GeV $\bar{p}p$ collisions at the Collider Detector at Fermilab (CDF). These quantities are tightly constrained in the Standard Model of electroweak interactions [1]. We believe that W and Z^0 bosons are produced in high-energy $\bar{p}p$ collisions at lowest order through the Drell–Yan process [2] ($q + \bar{q} \rightarrow W\ (Z^0)$) as well as through radiative QCD processes ($q + \bar{q} \rightarrow W\ (Z^0) + g$ and $q + g \rightarrow W\ (Z^0) + q$). Theoretical predictions of W and Z^0 production properties therefore depend on the parton momentum distributions in the proton, quark–boson couplings [3], and calculations of the higher–order strong interaction corrections to the zeroth order process [4], as well as the W and Z^0 masses. The decay widths of W and Z^0 bosons to leptons depend on the lepton-boson couplings. The comparison of the measured rates with the predicted rates thus tests many aspects of QCD and the Standard Model.

Because of their large mass, two body decay distribution, and relatively high production cross section, at $\sqrt{s} = 1800$ GeV the W and Z^0 bosons serve as a dominant source of high transverse momentum electrons. These electrons produce distinctive and easily recognizable signatures in the detector. In this paper we describe the identification of W and Z^0 bosons through their decay into electrons, concentrating on electron identification, acceptance, and backgrounds in CDF.

Since electrons from W and Z^0 decays are expected to be kinematically very similar, W and Z^0 candidate events are first selected from a common sample of events which contain at least one well–measured, isolated, high transverse–momentum electron. We then apply highly efficient cuts in identifying the second lepton from the boson decay. For W candidate events, there is a requirement on transverse–momentum imbalance in the calorimeter as a signal for the neutrino. For Z^0 candidate events, there is a requirement of a second electromagnetic cluster identified as an electron.

Section 2 describes the systems of the detector used in the identification of electrons. Sections 3 & 4 contain descriptions of the trigger, electron identification requirements, and the datasets used in the measurement. The discussions of the electron kinematic and geometric acceptance (section 5), electron selection efficiency (section 6), and background subtraction (section 7) follow. Further corrections and the calculation of the integrated luminosity are detailed in sections 8 and 9 respectively. Section 10 closes with a discussion of experimental results for the product of the cross section times branching ratio $\sigma \cdot \mathrm{B}(W \rightarrow \mathrm{e}\,\nu)$ and $\sigma \cdot \mathrm{B}(Z^0 \rightarrow \mathrm{e^+e^-})$ in $\bar{p}p$ collisions at $\sqrt{s} = 1800$ GeV and a comparison to theoretical predictions.

2 Detector Description

The CDF detector is an azimuthally and forward–backward symmetric detector designed to study the physics of $\bar{p}p$ collisions at the Fermi National Accelerator Laboratory (FNAL) Tevatron. Event analysis is based on charged particle tracking, magnetic momentum analysis, and finely segmented calorimeters. Particles produced in $\bar{p}p$ interactions pass through a thin beryllium beam pipe, charged particle tracking chambers, sampling calorimeters, and muon chambers. Figure 1 shows a side view of the CDF detector.

It is beyond the scope of this paper to describe in detail all aspects of the CDF detector. Such a description can be found in reference [5]. We will concentrate on the pertinent aspects for the analysis and detection of $W \rightarrow \mathrm{e}\,\nu$ and $Z^0 \rightarrow \mathrm{e^+e^-}$ events, specifically those concerning energy and momentum measurement.

2.1 Calorimeters

The CDF calorimeter covers 2π in azimuth and from 2° to 178° in polar angle, segmented into projective towers in azimuth and pseudorapidity [6]. The coverage consists of three separate regions - central, plug, and forward. For the measurement of electromagnetic energy, the central region covers the range $|\eta| < 1.1$, the plug region covers $1.1 < |\eta| < 2.4$, and the forward region covers $2.2 < |\eta| < 4.2$. For the measurement of hadronic energy,

the central region covers the range $|\eta| < 1.3$, the plug region covers $1.3 < |\eta| < 2.4$, and the forward region covers $2.3 < |\eta| < 4.2$. The electromagnetic calorimeter systems are summarized in table 1 – a description of the fiducial regions of the electromagnetic calorimeter coverage is given in section 5.1.

Electromagnetic Calorimeters

The central electromagnetic calorimeter [7] (CEM) uses lead sheets interspersed with polystyrene scintillator as the active medium and employs phototube readout. The calorimeter is 18 radiation lengths (0.6 absorption lengths) thick with a projective tower size of $0.1 \times 15°$ in $\eta \times \phi$. The CEM has an energy resolution of $\frac{13.5\%}{\sqrt{E_T}} \oplus 2\%$ (the symbol $\oplus$ signifies that the constant term is added in quadrature in the resolution) [8]. Located approximately 6 radiation lengths into the calorimeter (shower maximum for electromagnetic showers) is a proportional chamber (CES) with strip and wire readout providing shower position measurements in both the Z and $R\phi$ views respectively. The position resolution of this chamber is 0.2 cm by 0.2 cm. The CEM calorimeter is physically segmented into 15° sections in azimuth and along the $\eta = 0$ plane in Z.

The plug electromagnetic calorimeter [9] (PEM) uses lead absorber panels interspersed with gas proportional chambers and cathode pad readout giving a total thickness of 18-21 radiation lengths (0.6-0.7 absorption lengths). The PEM has an energy resolution of $\frac{28\%}{\sqrt{E}} \oplus 2\%$ with a tower size of $0.09 \times 5°$ in $\eta \times \phi$. Shower positions are measured using information from the θ and ϕ pads resulting in a resolution of 0.2 cm by 0.2 cm. The PEM calorimeter is divided into quadrants.

The forward electromagnetic calorimeter [10] (FEM) uses lead absorber panels interspersed with gas proportional chambers and cathode pad readout giving a total thickness of 25 radiation lengths (0.8 absorption lengths). The FEM has an energy resolution of $\frac{25\%}{\sqrt{E}} \oplus 2\%$ with a tower size of $0.1 \times 5°$ in $\eta \times \phi$. Shower positions are measured using

information from the θ and ϕ pads with a resolution of 0.1 cm to 0.4 cm depending upon the location in the calorimeter.

Hadronic Calorimeters

The central hadronic calorimeter (CHA) [11] uses steel absorber interspersed with acrylic scintillator as the active medium. It is 4.5 absorption lengths thick and has an energy resolution of $\frac{75\%}{\sqrt{E_T}} \oplus 3\%$ for isolated pions [5].

The plug (PHA) and forward (FHA) hadronic calorimeters [12,13] use steel absorber interspersed with gas proportional chambers as the active medium. The PHA is 5.7 absorption lengths thick and has an energy resolution of $\frac{90\%}{\sqrt{E}} \oplus 4\%$ for isolated pions [14]. The FHA is 7.7 absorption lengths thick and has an energy resolution of $\frac{130\%}{\sqrt{E}} \oplus 4\%$ for isolated pions [5].

2.2 Tracking

The CDF tracking system covers the angular range $\sim 8°$ to $\sim 172°$ in polar angle ($|\cos\theta| < 0.99$) and is contained within a 1.412 T axial magnetic field. Three dimensional track reconstruction is available in the range 25° to 155° in polar angle ($|\cos\theta| < 0.91$). The tracking detectors consist of two separate systems: an inner radius system of eight small vertex time projection chambers (VTPC) used for charged track position measurement over a large angular range and at larger radii a central tracking chamber (CTC) used for charged particle momenta and position measurements.

Immediately outside of the beam pipe, the VTPC [15] measures charged particle positions over the angular range $\sim 8°$ to $\sim 172°$. Sense wires provide measurements of the track coordinates in $R\,Z$, pads and small angle stereo wires provide measurements in $R\,\phi$. Reconstructed track segments in the VTPC are used to measure the location of the interaction vertex position, Z_{vert}, with a resolution of 1 mm in the Z direction.

The central tracking chamber [16] is a 3.2 m long cylindrical drift chamber with an outer radius of 1.3 m providing precise momentum determination and spatial position in

the range $\sim 25°$ to $\sim 155°$ ($|\eta| < 1.5$). The chamber consists of 84 layers of sense wires, grouped into alternating axial and stereo superlayers. Axial superlayers consist of 12 sense wires; stereo layers have 6 sense wires (tilted at $\pm 3°$ relative to the beam direction). Wires in each superlayer form a vector which makes a 45° angle with respect to the radial direction in order to correct for the Lorentz angle of the electron drift in the magnetic field.

The momentum resolution of the CTC is $\frac{\delta p_T}{p_T} = 0.002 \times p_T$ for isolated tracks (where p_T is in GeV/c). Using the constraint that the track originates at the interaction vertex, the resolution improves to $\frac{\delta p_T}{p_T} = 0.0011 \times p_T$ (in GeV/c) by extending the effective track fitting region from 1 m to 1.3 m [17].

2.3 Luminosity Monitors

CDF uses scintillator planes located 5.8 m from the nominal interaction point as luminosity monitors. Known as the beam-beam counters (BBCs), these counters cover the angular range 0.32° to 4.47° and 175.53° to 179.68° ($3.24 < |\eta| < 5.88$). Coincident hits in the BBCs at opposite ends of the interaction region are used to signal an inelastic collision for the trigger system.

3 Triggering

The hardware trigger system is designed to use the projective nature of the calorimeter towers [18] along with a fast two dimensional hardware track finder (CFT) [19]. Trigger towers have a width of 0.2 in pseudorapidity and 15° in azimuth, mapping the detector into an array of 42 (in η) by 24 (in ϕ) in both electromagnetic and hadronic calorimeters.

The electron trigger makes use of both calorimeter and tracking information. A hardware cluster finder searches the electromagnetic tower array, forming clusters around seed towers. The seed towers are required to have at least 4 GeV of transverse energy (E_T), assuming the vertex position to be at $Z = 0$. Each of the 4 nearest neighbors of each seed tower (along the η and ϕ directions) are then checked and included in the cluster if the tower has $E_T > 3.6$ GeV. Again, each of the 4 nearest neighbor towers of each tower in the cluster are

checked and included in the cluster if the tower has $E_T > 3.6$ GeV. This algorithm repeats until the cluster can no longer be extended. The hadronic E_T in towers included in the cluster is added to the electromagnetic E_T to give a total cluster E_T. These clusters are then matched in azimuth with high transverse momentum tracks from the CFT.

The electron trigger requires that the cluster have more than 12 GeV in electromagnetic E_T (EM E_T), that the ratio of the total cluster E_T to EM E_T be less than 1.125, and that there be a track associated with the cluster with transverse momentum (p_T) greater than 6 GeV/c as measured by the CFT.

4 Event Selection

The analysis for both W and Z^0 candidate events concentrates on the selection of an isolated, well measured, high transverse–momentum electron in the central rapidity region (see table 1) where electron quantities are well measured. For Z^0 candidate events, the second electron candidate (which is not restricted to the central rapidity region) requirements are much less stringent than the first. For W candidate events, the neutrino missing energy signature is used.

In this section we describe the identification of electrons in CDF. Since the different calorimeter elements have different characteristics, the requirements and variables for the central, plug, and forward regions are different. We first describe the variables used in the electron selection in the central, plug, and forward calorimeters. We then describe the selection requirements for the central electron sample and the definitions of the W and Z^0 samples.

4.1 Global Electron Variables

Offline Clustering

The CDF electron identification algorithms begin with the formation of electromagnetic clusters using an array of seed towers with transverse electromagnetic energy (EM E_T) > 3.0 GeV. Neighboring towers are added to the cluster until the maximum cluster

size is reached [20]. The maximum cluster size is limited to 3 towers in pseudorapidity ($\Delta\eta \approx 0.3$) by 1 tower in azimuth ($\Delta\phi = 15°$) in the central region, 5 towers in pseudorapidity ($\Delta\eta \approx 0.5$) by 5 towers in azimuth ($\Delta\phi = 25°$) in the plug region, and 7 towers in pseudorapidity ($\Delta\eta \approx 0.6$) by 7 towers in azimuth ($\Delta\phi = 35°$) in the forward region. The cluster size used for the different calorimeters reflects the variation of shower size and cell size with η. For clustering purposes, $E_T \equiv E \sin\theta$ is defined using the energy (E) measured in the calorimeter and the polar angle ($\sin\theta$) given by the tower center position in the detector and the event vertex.

Electron Cluster Candidates

We require that the EM E_T of the cluster be > 5.0 GeV and that the ratio of hadronic E_T (for towers in the EM cluster) to electromagnetic E_T (Had/Em) be less than 0.125 for the cluster to be considered as an electron candidate.

Isolation

For every cluster passing these cuts, the variable Iso is defined as:

$$Iso = \frac{E_T^{cone} - E_T^{cluster}}{E_T^{cluster}} \quad (1)$$

where E_T^{cone} is the transverse energy in a cone centered on the electron cluster. The cone includes all towers within a radius in $\eta\phi$ space of $R \equiv \sqrt{\Delta\eta^2 + \Delta\phi^2} < 0.4$. This variable provides a measure of the presence of other energetic particles near the electron candidate by quantifying the relative amount of energy in the calorimeter near the electron cluster.

4.2 Central Electron Variables

Both the central electromagnetic calorimeter and the CTC cover the range $|\eta| < 1.1$. We require that there be a three dimensional track (in which all three components of momentum are reconstructed using the stereo information in the CTC) associated with the calorimeter cluster. The transverse energy of the central electron (E_T) is defined using the

direction of this track, as measured at the beam line, and the corrected calorimeter energy (defined in the following section) [21]. The ratio of the corrected calorimeter energy to the track momentum ($E/p = \mathrm{E_T}/\mathrm{p_T}$) is also used for identification purposes.

Electron Response Corrections

The measured energy in the calorimeter is corrected for the following known effects:

- Using the strip cluster position (described below), we correct for the response of a tower as function of the azimuthal and Z position of the shower. This correction has been taken from electron test beam data [22]. Figure 2 shows the relative response map as a function of shower position for a typical tower in the CEM. The correction from the response map is accurate to within 1.1% over the the CEM fiducial region (described in section 5.1).

- We use a sample of $\sim$ 17,000 electrons with $\mathrm{E_T} > 12$ GeV to normalize the calorimeter tower–to–tower response. Using distributions of E/p, the relative response scale for each of the 478 calorimeter towers is determined.

- An overall scale is determined using the W electron sample where we compare the energy of the tower (using the above corrections) to the momentum of the track. E/p distributions for this sample are compared to calculations from a radiative W Monte Carlo [23] and detector simulation which includes both internal and external bremsstrahlung [8] (see figure 3). A check on the uncertainty in the tracking chamber momentum scale is provided by the invariant mass distributions of $\mathrm{J}/\psi \rightarrow \mu^+\mu^-$ and $\Upsilon \rightarrow \mu^+\mu^-$ [8].

Strip Chamber Variables

As described in section 2.1, a gas proportional chamber (CES) is located in the central EM calorimeter at shower maximum. The electron position at shower maximum is

determined from a fit to the shower shapes (using a nominal test beam electron profile) as measured by the CES. We define the strip–track position match in the Z view (ΔZ) and the azimuthal view ($\Delta R\phi$) using this fitted shower position and the extrapolated electron track. The position resolution of the CES is 1.7 mm for 50 GeV electrons at normal incidence. The shower shape is itself a useful discriminator for electrons; we use a chi–squared (χ^2_{Strip}) from this position fit as an additional selection variable.

Lateral Shower Profile

We also use a measure of the lateral shower profile, $Lshr$, to identify electrons. The variable $Lshr$ compares the lateral shower profile to test beam data and is defined by

$$Lshr = 0.14 * \sum_i \frac{E_i^{Adj} - E_i^{Prob}}{\sqrt{0.14^2 * E + (\Delta E_i^{Prob})^2}} \tag{2}$$

where E_i^{Adj} is the measured energy in the tower adjacent to the seed tower; E_i^{Prob} is the expected energy in that tower calculated from the seed energy of the cluster, the impact point from the strip chamber, and the event vertex using a shower profile parameterization from test beam data; E is the EM energy in the cluster; and ΔE_i^{Prob} is the error in E_i^{Prob} associated with a 1 cm error in the impact point measurement [24]. All energies are in GeV. The sum is over the two towers adjacent to the seed tower in the same azimuthal wedge. Since $Lshr$ is a measure of the lateral development of a shower, we expect large differences in this variable when comparing electrons and jets.

4.3 Plug Electron Variables

Electron Response Corrections

As described in section 2.1, the plug EM calorimeter is divided into quadrants. The global energy scale and a response map (taking into account tower–to–tower variations) for one quadrant is derived from test beam data. The relative energy scale (quadrant–to–quadrant) is determined from comparing both the plug $Z^0 \rightarrow e^+e^-$ invariant mass (where

one electron is required to be in the CEM and the second in the PEM) and $W \rightarrow e\nu$ transverse mass distributions for each quadrant to the quadrant which was calibrated in the test beam. The quadrant-to-quadrant corrections are found to vary between -4% and +12%. Transverse energy of electrons in the plug calorimeter is determined using these energy corrections along with the position of the cluster, as measured in the calorimeter, and the location of the event vertex.

Additional Plug Electron Variables

We also use a lateral shower distribution variable in the plug region. This variable, denoted 3x3 χ^2 since it uses a 3x3 array of calorimeter cells and mimics a chi-squared test, measures the deviation of the shower from the predicted shower shape (as seen in an electron test beam). Since the full CTC tracking volume does not cover the plug region (see figure 1), we are unable to use a CTC track requirement in the plug electron identification. The VTPC does give good position information in the θ coordinate, but does not give a momentum measurement because of poor resolution in ϕ. We therefore use it to determine the presence of a charged particle. Given the cluster position and the event vertex, we define a road where we would expect the electron to go through the VTPC active region and look for hits on the wires along this road. The fraction of actual hits to expected hits is used to distinguish electrons from photons.

4.4 Forward Electron Variables

As described in section 2.1, the forward EM calorimeter is divided into quadrants. The global energy scale is determined using data from an electron test beam with one of these quadrants and a comparison of the invariant mass distribution of the forward $Z^0 \rightarrow e^+e^-$ (where one electron is in the CEM and the second in the FEM) candidates to that of the central $Z^0 \rightarrow e^+e^-$ (where both electrons are in the CEM) candidates. The relative energy scale is set by comparison of the forward $Z^0 \rightarrow e^+e^-$ invariant mass distributions in the different quadrants and by a study of neutron induced pulses in each quadrant. This

study assumes the flux of neutrons is independent of azimuth, so that the differential rate of neutrons above a threshold will be dependent only upon the energy scale. Quadrant–to–quadrant corrections are checked by looking at the normalization of these rates in each quadrant. These corrections vary from -4% to +4%. A non-linearity correction taken from a study of test beam and Z^0 data is also applied [25]. Transverse energy of electrons in the forward calorimeter is defined using these energy corrections along with the angle from the position of the cluster in the detector and the location of the event vertex.

Electron identification in the forward region does not use any additional requirements beyond the Had/Em ratio and the Iso requirements.

4.5 Common Central Electron Sample

We define a common central electron sample (with common selection efficiencies and backgrounds) for both W and Z^0 event candidates. We require that the candidate cluster have $|\eta| < 1.1$, $E_T > 20.0$ GeV, $Iso < 0.1$, $Had/Em < 0.055 + 0.045 \times E/100$ where E is the energy of the cluster in GeV, $\chi^2_{Strip} < 15.0$, and $Lshr < 0.2$. In addition, we require a reconstructed 3–dimensional track associated with the cluster with $E/p < 1.5$, $|\Delta Z| < 3.0$ cm, and $|\Delta R\phi| < 1.5$ cm. We also require that the Z vertex position as measured by the VTPC be within 60 cm of the nominal position. These requirements are summarized in table 2. The distributions of these variables, where we applied all the cuts but the one being plotted, are shown in figure 4. There are 5012 events which pass these requirements.

In addition we require that the event pass the electron trigger and that the central electron candidate be in a good fiducial region of the central detector (see section 5.1). From this sample we select W and Z^0 candidate events using the "other" lepton from the boson decay. For W events, this lepton is a neutrino, so we look for a transverse energy imbalance. For Z^0 events, this lepton is an electron, so we look for the presence of another electromagnetic cluster.

W selection

The Missing E_T ($\not\!\!E_T$) is defined to be negative of the vector sum of transverse energy in calorimeter towers over the pseudorapidity range $|\eta| < 3.6$,

$$\not\!\!E_T \equiv - \sum_{|\eta|<3.6} \vec{E}_t. \tag{3}$$

The pseudorapidity range is restricted because the low beta quadrupoles of the Tevatron cover part of the azimuthal regions for $3.6 < |\eta| < 4.2$. To be included in the sum, the towers must pass an energy threshold requirement of 0.1 GeV in the CEM and CHA, 0.3 GeV in the PEM, 0.5 GeV in the PHA and FEM, and 0.8 GeV in the FHA [26]. The distribution of $\not\!\!E_T$ for electron events passing the trigger and fiducial requirements is shown in figure 5. Overlaid on this distribution is the expected distribution for the $\not\!\!E_T$ from Monte Carlo (see section 6.3). We do not apply any corrections to the calculation of $\not\!\!E_T$. For W events, we require that $\not\!\!E_T > 20$ GeV. We also ask that the event not be consistent with being a Z^0 event as defined below. There are 2664 events which pass these requirements.

Z^0 selection

For the Z^0 event selection we require a second electromagnetic cluster located in the good fiducial region (described below) of either the central, plug, or forward detector with $E_T > 10$ GeV, $Iso < 0.1$, and $Had/Em < 0.1$. In the central region, we require the presence of a 3-d track and that $E/p < 2.0$. In the plug region, we ask that the $3x3$ $\chi^2 < 20.0$ and the VTPC hit fraction > 0.5. Distributions of these variables are shown in figure 6.

Once we have two selected clusters, we require that the invariant mass of the clusters be between 70 and 110 GeV/c^2 (see figure 7). There are 243 events which pass these requirements.

5 Geometric and Kinematic Acceptance

The boson selection efficiency can be factored into two terms: the geometric acceptance (a function of the electron fiducial and kinematic cuts) and the efficiency of the electron and neutrino selection requirements (which depends on the electron identification requirements and the $\not\!\!E_T$ resolution). In this section we describe the geometric and kinematic acceptance beginning with the definition of the fiducial regions.

5.1 Fiducial Regions

As described in Section 2, CDF is constructed to be both azimuthally and forward–backward symmetric. A representation in η - ϕ space of one quadrant of the CDF detector is shown in figure 8, with the good fiducial regions for electrons marked. These regions are selected to avoid calorimeter edges and thus ensure well understood electron response. Note that our η - ϕ cuts refer to fixed regions in the calorimeter. The actual η and ϕ for a given electron is smeared by the production vertex distribution and bending in the magnetic field.

In the η coordinate, we require that the electron be located away from regions where the response of the calorimeter is compromised by cracks or detector overlap. These regions are:

- the $\theta = 90°$ crack region where the two halves of the central calorimeter come together ($|\eta| < 0.05$)
- the boundary region of the central and plug calorimeters ($1.0 < |\eta| < 1.3$)
- the overlap region between the plug and forward calorimeters ($2.2 < |\eta| < 2.4$).

We therefore require that the electron be located in the region $0.05 < |\eta| < 1.0$, $1.3 < |\eta| < 2.2$, or $2.4 < |\eta| < 3.7$.

For electrons within the central region, the selection is made using the strip cluster Z position and require that the strip cluster position be more than 9 cm and less than 217 cm

from the $\eta = 0$ plane. (The strip chambers cover the region 6.2 cm $< Z <$ 239.4 cm and the active region of the calorimeter covers 4.2 cm $< Z <$ 246.0 cm [22].)

For electrons in the plug and forward calorimeters, where towers are segmented into roughly 0.1 units of η, the selection is made using the location of the seed tower in the cluster. In the plug region, we require that the seed tower be more than two towers away from the calorimeter η boundaries. In the forward region we require that the seed tower be more than 5 towers away from the large η boundary (closer to the beamline) but make no requirement near the small η boundary.

In the ϕ coordinate, the selection also depends upon the detector region. At the depth of the strip/wire chamber in the central region, the wedge has a width of 48.5 cm, the strip chambers extend to within 1.7 cm of the wedge boundary and the active region of the calorimeter extends to within 1.1 cm [22]. In this region, we require that the strip cluster position be more than 3.2 cm from the wedge boundary. For the plug and forward regions, we require that the seed tower of the cluster be more than 5° from the quadrant boundaries in ϕ. These calorimeters are segmented into towers of 5° in ϕ, so that this requirement excludes the towers adjacent to the boundary.

In addition to these symmetric boundary regions, we have several small irregular regions which are excluded. The region $0.77 < \eta < 1.0$ and $75° < \phi < 90°$ is not instrumented — it is the penetration for the cryogenic connections to the superconducting solenoid. In the plug calorimeter, there were a small number of known regions with dead channels ($\sim$ 2%) and we require that the seed tower not be in one of these regions.

5.2 Monte Carlo Generators

We use a zeroth order Monte Carlo which includes only the Drell–Yan diagram $q + \bar{q} \rightarrow W(Z^0)$ (figure 9) to generate the 4–vectors of the leptons from the boson decay. It includes polarization effects and the correct matrix element for the decays $W \rightarrow e\nu$ and $Z^0 \rightarrow e^+e^-$. The bosons are generated from a relativistic Breit-Wigner line shape truncated at $\pm$ 2 widths

(the results are found to be independent of this cut). We do not include the photon diagrams in the Z^0 Monte Carlo (see section 8.2 below).

We take as input the structure function parameterizations by Martin et al. (MRSB and MRSE) [27], Duke and Owens with $\Lambda_{QCD} = 0.2$ GeV (DO1) [28], and Eichten et al. with $\Lambda_{QCD} = 0.2$ GeV (EHLQ1) [29]. Since the bosons from this Monte Carlo are generated with zero transverse momentum, the transverse momentum spectrum measured from Z^0 candidate events (where the boson 4–vector is reconstructed) is used as an input distribution (figure 10). Systematic uncertainties due to including only zeroth order diagrams are discussed in the following section.

We also use the ISAJET [30] and PAPAGENO [31] Monte Carlos as event generators. These Monte Carlos allow for the inclusion of higher order diagrams such as $q + g \rightarrow W(Z^0) + q$ and $q + \bar{q} \rightarrow W(Z^0) + g$ (figure 11) in the generation. Although these generators are slower than the Monte Carlo described above, they provide a valuable check on the results.

5.3 Detector Model

A simple detector model is used for the study of acceptances. This model uses only the lepton 4–vectors from the Monte Carlos described above. Since the acceptance is defined by requiring the electrons from the boson decays pass only certain geometric and kinematic requirements, it is not necessary to use a complete detector simulation. The electron selection efficiencies (which do not include kinematic and geometric acceptances) are determined using the data and are discussed in section 6.

In the model, an event vertex is chosen from a Gaussian distribution with $\sigma = 30$ cm, truncated at 2σ. The decay electrons are propagated from the vertex through the magnetic field to the calorimeters and position detectors. Electron energies are smeared using Gaussians of the nominal calorimeter resolutions (see section 2.1). Fiducial and kinematic cuts as described above are applied to each electron, and efficiencies are determined as described below.

5.4 Acceptance Results and Systematics

We define the acceptances for W and Z^0 events as follows:

$$A_W = \frac{\#\text{ events with electron in good central fiducial region, } E_T > 20}{\#\text{generated events}}$$

$$A_Z = \frac{\#\text{ events with 1 electron in good central fiducial region, } E_T > 20 \text{ and a second electron in any good fiducial region, } E_T > 10}{\#\text{generated events}}.$$

In addition, for Z^0 events we define the following variables:

$$F_{cc} = \frac{\#\text{ events with second electron in central fiducial region}}{\#\text{ accepted events}}$$

$$F_{cp} = \frac{\#\text{ events with second electron in plug fiducial region}}{\#\text{ accepted events}}$$

$$F_{cf} = \frac{\#\text{ events with second electron in forward fiducial region}}{\#\text{ accepted events}}.$$

These variables represent the fraction of accepted events which have both electrons in the central region (F_{cc} central-central events), one electron in the central region and the second in the plug region (F_{cp} central-plug events), or one electron in the central region and the second in the forward region (F_{cf} central-forward events). They are used in the calculation of the overall selection efficiency for Z^0 events.

In Table 3 we show the values for A_W and A_Z, where we have used our zeroth-order Monte Carlo with p_T taken from a smoothed p_T distribution of the Z^0 candidates (see figure 10). The quoted errors in the table are statistical only. One can see that A_W varies at the 1% level when changing structure functions, whereas A_Z is more stable. We take the uncertainties on A_W and A_Z due to the choice of structure functions to be $\pm$ 1.1% and $\pm$ 0.3% respectively.

The W acceptance is also a function of M_W, changing by approximately 0.8% for a 1 GeV/c^2 change in M_W. The assumed masses were $M_W = 80.0$ GeV/c^2 and $M_Z = 91.1$ GeV/c^2. We have used $\sin^2\theta_W = 0.229 \pm 0.007$ [32] which implies a 360 MeV/c^2 uncertainty in M_W (given the fixed M_Z). We therefore assign an additional $\pm$ 0.3% uncertainty to A_W.

The assumed p_T distribution has little effect on the acceptances. Figure 12 shows A_W and A_Z as a function of p_T. Since scaling the p_T distribution of figure 10 by $\pm$ 20% changes the acceptances by less than 0.4%, we take $\pm$ 0.4% as the systematic uncertainty due to the choice of the p_T distribution chosen.

Finally, higher order QCD corrections are expected to alter the rapidity distributions (see reference [33]) and therefore the acceptances. The acceptance as calculated using ISAJET with only the lowest order Drell–Yan diagram (figure 9), where events from this process pick up transverse momentum from initial state radiation, agrees with our zeroth order Monte Carlo. However, using ISAJET with only higher order diagrams (figure 11) which are only part of the order α_s correction, we see an increase in A_W and A_Z of 3% and 1.4%. We have also studied the effect of higher order corrections by running PAPAGENO with zeroth and first order diagrams. PAPAGENO with only the lowest order Drell–Yan diagram does not give transverse momentum to the bosons. If we again use the p_T distribution from our candidate Z^0 events, we find that the acceptance is the same as from our zeroth order Monte Carlo. Running PAPAGENO with the next order diagrams only and a lower cutoff on the parton p_T of 8 GeV/c (again, these diagrams are only a part of the order α_s corrections), we see an increase in A_W and A_Z of 1.3% and 0.8%.

Our Monte Carlo reproduces the leading order calculations from ISAJET and PAPAGENO, but QCD corrections alter the leading order rapidity distributions. The increases quoted above are from events generated with only the higher order diagrams, so we anticipate a smaller change than those increases. We therefore choose to assign a systematic uncertainty of $\pm$ 0.9% to A_W and $\pm$ 0.4% to A_Z.

Systematic uncertainties in the W and Z^0 acceptances are summarized in Table 4.

5.5 Final Values for the W and Z^0 Geometric Acceptances

We choose to use MRSB structure functions and the results from our zeroth-order Monte Carlo for the values of A_W and A_Z. For the W acceptance, the prediction of this set of structure functions falls in between the values of DO1 and EHLQ1. In the Z^0 case, the acceptances are almost identical (see Table 3). The total geometric acceptance is a combination of kinematic and geometric requirements:

- For the W events, the requirement that the electron pass the kinematic requirement is $\sim$ 81% efficient. Of the electrons that satisfy this criterion, $\sim$ 57% of them are in the central region and, of these, $\sim$ 76% are in a good fiducial region for a total acceptance of $\sim$ 35%.

- For the Z^0 events, the kinematic requirements for the electrons are $\sim$ 88% efficient. Of events satisfying these criteria, $\sim$ 80% have electrons in the central region. Of these central electrons, $\sim$ 83% are in a good fiducial region. Requiring that the second electron be in a good fiducial region anywhere in the detector is then $\sim$ 64% efficient for a total geometric acceptance of $\sim$ 37%.

To summarize, we use the following for A_W and A_Z:

$$A_W = 35.2 \pm 1.5 \text{ \% (stat + sys)}$$
$$A_Z = 37.1 \pm 0.7 \text{ \% (stat + sys).}$$

6 Selection Efficiencies

The efficiency studies can be broken down into three pieces: electron trigger efficiency, electron selection efficiencies, and $\not\!\!E_T$ selection efficiency. All are discussed below.

6.1 Electron Trigger Efficiency

The efficiency of the electron trigger for W and Z^0 events is measured using a data sample which is selected by requiring a large E_T imbalance in the calorimeter. This trigger

(the $\not\!\!E_T$ trigger) is independent of the electron trigger, and will pass some fraction of W events. After identifying an electron in this $\not\!\!E_T$ sample, we measure the efficiency of the electron trigger to be 0.973 ± 0.005.

6.2 Electron Selection Efficiency

The efficiencies for the electron selection requirements are determined directly from the data. To measure the efficiencies properly one would like an unbiased, background free sample of W and Z^0 bosons decaying to electrons. Unfortunately, cuts which are necessary to lower the background may also bias the distributions. We will therefore measure the efficiencies in a number of ways in order to check the results for consistency.

The first method used is to select an independent sample of W events using global event quantities which are independent of electron selection criteria, tagging the decay of the W through the presence of the ν (the $\not\!\!E_T$ selected electron sample). For this sample we require that $|Z_{vert}| < 60$ cm, that there be a large transverse momentum imbalance ($\not\!\!E_T > 20$ GeV), and that this imbalance be significant in comparison to the total energy flow in the event using the cut $\delta \not\!\!E_T \equiv \frac{\not\!\!E_T}{\sqrt{\sum E_T}} > 2.7$, where $\sum E_T$ is the scalar sum of all transverse energy over the same η range as the $\not\!\!E_T$ sum. This cut is more than a 4.5σ deviation in $\delta \not\!\!E_T$ from azimuthally symmetric events where the $\not\!\!E_T$ comes from measurement resolution. In addition, we require that there be one and only one cluster of energy in the event with $E_T > 5$ GeV and $Had/Em < 0.125$ in a good fiducial region as described above. If the cluster is in the plug or forward regions, we also require that the transverse mass [34] be > 50 GeV/c^2. The process $W \rightarrow e\ \nu$ has all of these characteristics. This selection gives us a sample of high p_T electrons without the electron cuts applied.

As a second method, we use a sample of $Z^0 \rightarrow e^+e^-$ events (the Z^0 selected electron sample), where we require there be at least one good central electron candidate as defined in section 4.5, a second cluster with $E_T > 10$ GeV in a good fiducial region, and an invariant mass of the two clusters in the window 81 - 101 GeV/c^2. By looking at the characteristics of the second electron in the event, we are able to measure the electron identification

efficiencies in a second unbiased fashion. This method is used as a check on the efficiencies as determined from the $\not\!\!E_T$ sample.

From these samples, we measure the electron identification efficiencies. Tables 5, 6, 7, and 8 show the individual efficiencies for each of the cuts in the event selection and the combined efficiency for the entire set of cuts from both the $\not\!\!E_T$ selected and Z^0 selected samples. We use the efficiency of the combined set of cuts (which is not equal to the product of the efficiencies for the individual cuts) to account for possible correlations. The efficiencies for both samples are in reasonable agreement. The combined efficiency from the $\not\!\!E_T$ (Z^0) selected sample for the common central electron selection (c_1) is 0.84 $\pm$ 0.03 (0.85 $\pm$ 0.03), for the loose central electron selection (c_2) is 0.93 $\pm$ 0.03 (0.93 $\pm$ 0.03), for the plug electron selection (p) is 0.90 $\pm$ 0.03 (0.92 $\pm$ 0.03), and for the forward electron selection (f) is 0.91 $\pm$ 0.04 (0.89 $\pm$ 0.07). We take as final values for these efficiencies the values from the $\not\!\!E_T$ sample:

$$c_1 = 0.84 \pm 0.03$$

$$c_2 = 0.93 \pm 0.03$$

$$p = 0.90 \pm 0.03$$

$$f = 0.91 \pm 0.04$$

We estimate the residual non-electron backgrounds in the $\not\!\!E_T$ sample to be $< 1\%$ (central region), $< 1\%$ (plug region), and $< 3\%$ (forward region) based on studies of the isolation distribution. From this estimate we extract an additional systematic uncertainty on the efficiencies of the central, plug, and forward electron selection, which is included in the numbers listed above.

6.3 $\not\!\!E_T$ selection efficiency

To measure the efficiency of the $\not\!\!E_T$ requirement, we use the PAPAGENO event generator and a full detector simulation. In other studies, the predictions of this Monte Carlo for kinematic properties of W + jet events agree well with the distributions seen in data [35].

The $\not\!\!E_T$ selection efficiency (ϵ_ν) is defined to be the probability that $\not\!\!E_T > 20$ GeV given that the electron has $E_T > 20$ GeV. We study this probability as a function of the number of energetic jets (excluding the electron candidate) with detected $E_T > 10$ GeV (see reference [36] for the definition of a jet). We find that ϵ_ν decreases with the presence of additional energetic jets in the event. This correlation is a result of both systematic mismeasurement of the jet energy as the jet energy increases [36] and statistical fluctuations in the measurement of the jet energy and hence a broadening of the $\not\!\!E_T$ resolution as a function of the total energy in the event. Fluctuations which result in a lower calculated $\not\!\!E_T$ will therefore lower the efficiency.

Given ϵ_ν as a function of the number of energetic jets, we use the jet multiplicity found in the data to calculate the final value of ϵ_ν. (As an aside we find that the Monte Carlo fraction of events with 0, 1, and ≥ 2 jets is in reasonable agreement to the data.) Using the fraction of events with 0, 1, and ≥ 2 jets as seen in the data for the weighting, the final value for the $\not\!\!E_T$ efficiency is $\epsilon_\nu = 0.96 \pm 0.02$. Table 9 summarizes the results.

6.4 Final Selection Efficiencies

The total efficiency for the W selection is given by $\epsilon_W = \epsilon_\nu \cdot c_1$, accounting for both the $\not\!\!E_T$ and the central electron selection efficiencies, and is found to be $\epsilon_W = 0.81 \pm 0.04$.

The efficiency for the Z^0 selection is a combination of the electron selection efficiencies and the fraction of events with a second electron in various detector regions (as defined in section 5). It is defined as:

$$\epsilon_Z = F_{cc} \cdot c_1 \cdot (2c_2 - c_1) + F_{cp} \cdot c_1 \cdot p + F_{cf} \cdot c_1 \cdot f, \tag{4}$$

where F_{cc}, F_{cp}, and F_{cf} are the expected fractions of events with the second electron in the central, plug, and forward regions as determined from acceptance studies. In Eq (4), we have neglected the contribution to ϵ_Z from events where the second central electron has 10 GeV $<$ E_T $<$ 20 GeV because the rate for this class of events is negligible. The term $2c_2 - c_1$ arises because Z^0 events with both electrons in the central region can have either electron satisfy the common central electron requirement. The final value for ϵ_Z is 0.80 ± 0.03 [37]. The complete efficiencies are summarized in table 10.

7 Backgrounds

Although high p_T, isolated electrons come predominantly from the decay of W and Z^0 bosons, there are other processes which can have such a signal. In the following sections we calculate the contributions from other processes as backgrounds in the selection of W and Z^0 events.

7.1 W Backgrounds

Backgrounds to the W sample can come from physics processes which contain a (real) high p_T electron and missing energy (*e.g.*, heavy quark production and semileptonic decay) and from processes (QCD) which through fluctuations in jet measurement and fragmentation cause a (fake) high p_T electron and missing energy.

W Background from QCD and Heavy Quarks

Given the high rates for QCD processes (multijet events and heavy quark production) in comparison to W production at the Q^2 scale of interest, topologies with even small probabilities can contribute to the W sample background. The background from QCD processes comes from events where one of the produced partons fragments into an electromagnetically rich jet (which passes electron selection criteria) while the other parton jet mimics a neutrino (and hence large $\not\!\!E_T$) through fluctuations in fragmentation and/or measure-

ment. The background from heavy quark decays come from the production of real electrons through the semileptonic decay of the quark.

We study these backgrounds with a sample of central electrons where we have applied all the event selection criteria outlined in section 4.5 except the isolation requirement. We will break the sample into background samples and a high $\not\!\!E_T$ sample. Since we want the background samples to contain little or no W event contamination, we require that the $\not\!\!E_T$ for this samples be less than 10 GeV. We use the distributions of electron isolation and $\not\!\!E_T$ to quantify the background.

If the $\not\!\!E_T$ and isolation are correlated, this requirement could bias the background sample. To first order we expect no correlation between these variables to exist because the regions of the events which determine the isolation and $\not\!\!E_T$ characteristics are physically separated from each other. (In dijet events, one jet fluctuates to fake an electron while fluctuations in the opposite jet dominate the $\not\!\!E_T$. In $\bar{b}b$ events, the c quark jet associated with the electron can affect both the $\not\!\!E_T$ and the isolation measurements; however, since the the electron is required to have a high transverse momentum, the c quark jet is expected to be much softer than the opposite jet and not contribute as much to the $\not\!\!E_T$.) To test this hypothesis, we selected events with a good electron (passing all the central electron cuts except the isolation requirement), and plot the event $\not\!\!E_T$ versus the isolation of the electron (see figure 13). The region with $\not\!\!E_T > 20$ GeV and $Iso < 0.1$ shows a clustering in W signal region. In events with $\not\!\!E_T > 20$ GeV, we see a tail in the isolation distribution stretching out to high values of Iso, but there is no visible correlation between the two variables.

To estimate the background contribution we define 3 samples from the non-isolated electron sample:

- Events with $\not\!\!E_T > 20$ GeV (the $\not\!\!E_T > 20$ sample).
- Events with $\not\!\!E_T < 10$ GeV and a jet with $E_T > 10$ GeV (control sample 1)

- Events with $\not\!\!E_T$ < 10 GeV and a jet with E_T > 20 GeV, which is a subset of control sample 1 (control sample 2).

In all of these samples, we reject events which pass the Z^0 selection. Figure 14 shows the isolation distributions for the three samples. We then estimate the background using the equation:

$$\frac{W \text{ background}}{\#\, Iso > 0.3 \text{ in the } \not\!\!E_T > 20 \text{ sample}} = \frac{\#\, Iso < 0.1 \text{ in control sample 1 or 2}}{\#\, Iso > 0.3 \text{ in control sample 1 or 2}}, \quad (5)$$

taking the average of the answers using the two control samples. We find this background to be 100 ± 50 events.

W Background from $Z^0 \rightarrow e^+e^-$

We next consider the background to the W sample from $Z^0 \rightarrow e^+e^-$ decays where one electron is detected but the other is not identified as an electron in the calorimeter due to detector effects such as cracks or poor EM response. We would then see an electron in conjunction with a large $\not\!\!E_T$. In the region $|\eta| < 1.1$ where we have good (magnetic) tracking we can use the presence of a high p_T track to reject such events. For events where second electron from the Z^0 decay is outside of the central tracking region, we use the ISAJET Monte Carlo with a full detector simulation to estimate the background to the W events, normalizing to the total number of Z^0 events in our sample. From this study, we estimate a total background of 40 ± 15 events from $Z^0 \rightarrow e^+e^-$ decays.

W Background from $Z^0 \rightarrow \tau^+\tau^-$

We also consider the process $Z^0 \rightarrow \tau^+\tau^-$, where one τ decays into an electron and two neutrinos, resulting in a large amount of $\not\!\!E_T$ measured in the detector. We have again used ISAJET with a full detector simulation to estimate this background. Taking into account the branching fraction of $\tau \rightarrow e\, \nu\, \nu$ and normalizing to the number of events in our $Z^0 \rightarrow e^+e^-$ sample, we estimate this background to be 8 ± 4 events.

W Background from heavy TOP

We consider the decay of heavy top into real W 's as a background process. With the preliminary CDF limit that the top mass is larger than 89 GeV/c^2 [38], we take the background contribution to be 0, but with an error equal to the number of events in the W sample for a 90 GeV/c^2 top mass, assuming a 150 pb cross section [39]. Using the ISAJET program and a full detector simulation, we estimate a background of 30 events from the decay

$$t \rightarrow Wb \qquad W \rightarrow \mathrm{e}\,\nu$$
$$\bar{t} \rightarrow W\bar{b} \qquad W \rightarrow \text{anything.}$$

If we also include the decay $W \rightarrow \tau \rightarrow$ e, we estimate a background of $0\ ^{+31}_{-0}$ events from heavy top decays into real W 's.

W Background from $W \rightarrow \tau \rightarrow$ e

We expect a large background source from the decay $W \rightarrow \tau\ \nu$ followed by the decay $\tau \rightarrow$ e $\nu\ \nu$, where the final state is identical to that from the decay $W \rightarrow$ e ν. The main difference between the two processes is that the electron E_T and $\not\!\!E_T$ spectra are much softer in the $W \rightarrow \tau \rightarrow$ e decay. Since $W \rightarrow \tau\ \nu$ has the same branching fraction as $W \rightarrow$ e ν in the Standard Model, a determination of the relative acceptance of direct decays to the sequential decays gives us the fraction of events in the sample which come from $W \rightarrow \tau \rightarrow$ e decays.

To estimate this background, we need to determine the ratio, $R(\frac{e}{\tau})$, of the acceptance for the direct electron from the W decay to the acceptance for the sequential electron from the τ decay. In this ratio, we include the branching fraction of the decay $\tau \rightarrow$ e $\nu\ \nu$. Using the ISAJET program to generate the process $W \rightarrow \tau\ \nu$ and $\tau \rightarrow$ e $\nu\ \nu$ and the detector model discussed in section 5, we find that $R(\frac{e}{\tau}) = 27 \pm 3$. To estimate the background

contribution to our sample, we need to take into account the effect of other backgrounds, since $R(\frac{e}{\tau})$ relates only the $W \rightarrow e\,\nu$ and $W \rightarrow \tau \rightarrow e$ samples.

The total number of W candidate events (W_{cand}) can be written

$$W_{cand} = (W \rightarrow e\,\nu) + (W \rightarrow \tau \rightarrow e) + \text{other background}, \tag{6}$$

where other background is the background estimate from other processes and

$$(W \rightarrow \tau \rightarrow e) = \frac{(W \rightarrow e\,\nu)}{R(\frac{e}{\tau})}. \tag{7}$$

Using our numbers for W_{cand} (2664 events), other background (totaling 148 $\pm$ 48), and $R(\frac{e}{\tau}) = 27 \pm 3$, we estimate the background from the sequential decay $W \rightarrow \tau \rightarrow e$ to be 90 $\pm$ 10 events.

Total W Background

Combining all the backgrounds, we estimate the total background in the W sample is $238 \pm^{62}_{53}$ events. In combination with the W sample of 2664 events, we find the number of W candidate events to be 2426 $\pm$ 52 (stat) $\pm^{53}_{82}$ (sys).

7.2 Z^0 Backgrounds

Since for the Z^0 sample we require two high p_T, isolated electron candidates, we expect that the relative backgrounds will not be as large as they are for the W sample. However, we do expect backgrounds from QCD processes and from the sequential decay $Z^0 \rightarrow \tau^+\tau^-$, where both τ's decay into e's. We will discuss the backgrounds in the order of the size of their contributions.

Z^0 Background from QCD

The dominant background source is from QCD processes, where partons fluctuate to look like electrons. We use the isolation of the electron candidates in conjunction with the invariant mass of the two candidates to estimate the contribution of this background. We

make use of the sample of non-isolated electrons discussed above. In the following, we refer to the central electron candidates in this sample as the first electron. We first pick events which have a second electron candidate which passes all requirements outlined in section 4.5 except for the isolation requirement. The pair mass of this sample is required to be in the window 70 GeV/c^2 - 110 GeV/c^2. As can be seen in figure 15, this sample is dominated by Z^0 events. We define 4 categories of events:

- Events with first electron Iso < 0.1, second electron Iso < 0.1 (the Z^0 sample).
- Events with first electron Iso < 0.1, second electron Iso > 0.2 (the $Iso1$ sample).
- Events with first electron Iso > 0.2, second electron Iso < 0.1 (the $Iso2$ sample).
- Events with first electron Iso > 0.2, second electron Iso > 0.2 (the $NonIso$ sample).

We compute the background to the Z^0 sample as an average of two estimates. The first makes use of the following equation:

$$\frac{Z^0 \text{ background}}{\#\text{ events in the } Iso1 \text{ sample}} = \frac{\#\text{ events in } Iso2 \text{ sample}}{\#\text{ events in } NonIso \text{ sample}} \tag{8}$$

We also use the control samples 1 and 2 used in section 7.1 for the W background and define the Z^0 background as follows:

$$\frac{Z^0 \text{ background}}{\#\, Iso > 0.3 \text{ in the } Iso2 \text{ sample}} = \frac{\#\, Iso < 0.1 \text{ in control sample 1 or 2}}{\#\, Iso > 0.3 \text{ in control sample 1 or 2}} \tag{9}$$

By combining these estimates, we estimate the background in the Z^0 sample to be 5 ± 3 events.

Z^0 Background from $Z^0 \rightarrow \tau^+\tau^-$

We also consider the process $Z^0 \rightarrow \tau^+\tau^-$, where both τ's look like electrons. Using ISAJET and a full detector simulation, we find no events with an invariant mass above 50 GeV/c^2 in a Monte Carlo sample corresponding to roughly twice the size of the data sample. We consider the background contribution from the process $Z^0 \rightarrow \tau^+\tau^-$ to be negligible.

Total Z^0 Background

The total background estimate for the Z^0 sample is 5 $\pm$ 3 events. In combination with the sample of 243 candidate events, we find the number of Z^0 candidates to be 238 $\pm$ 16 (stat) $\pm$ 3 (sys) events.

8 Further Corrections

There are two additional (but small) corrections which we need to apply to our calculation of the efficiencies described in section 6. The first applies to the central electron selection, so it is common to both the W and Z^0 samples, while the second applies only to the Z^0 sample.

8.1 Vertex Correction

In the calculation of the acceptances described in section 5, we used a Gaussian vertex distribution, with σ = 30 cm, cut at 2σ. This distribution and the cut are motivated by the vertex distribution we see in the data. Figure 16 shows the vertex distribution for events with an EM cluster with E_T > 20 GeV. Superimposed on the data is a Gaussian distribution which has a mean = 0 and σ = 30 cm. When we fit the distribution, we find a good fit (χ^2 = 134 with 100 points and 3 parameters in the fit) with a mean of -0.5 $\pm$ 0.3 and σ = 29.7 $\pm$ 0.5 cm. We now need to include the effect of the $|Z_{vert}| < 60$ cm cut in our calculation of the efficiency. From Gaussian statistics, we calculate the efficiency of the vertex cut to be 0.959 $\pm$ 0.005, where the error reflects the uncertainty in the fitted σ.

8.2 Drell-Yan and Z^0 Width Corrections

The experimental signature we use to tag the presence of Z^0 production is the presence of two high p_T, isolated electrons with an invariant mass near the Z^0 mass. The process $\bar{p}p \rightarrow \gamma^* \rightarrow e^+e^-$ has this signature as well. Since what we measure is the production of e^+e^- pairs in the mass range of 70 — 110 GeV/c^2, we have contributions to the total rate from the γ, Z^0, and interference terms. However, theoretical calculations have tradi-

tionally included only the Z^0 diagrams in calculating the total rate. We thus "correct" our measurement in order to compare with theory. In addition, since the Z^0 has a non-zero width, there are e^+e^- events through the Z^0 resonance which fall outside of the chosen mass range.

Integrating the contribution from the matrix element $|Z^0+\gamma|^2$ over the mass range 70 – 110 GeV/c^2 and the contribution from the matrix element $|Z^0|^2$ over the mass range 50 – 150 GeV/c^2, we find that the ratio of the full Z^0 contribution to the limited $Z^0 + \gamma$ contribution is 1.01 ± 0.01. We therefore apply a net multiplicative correction of 1.01 ± 0.01 to the e^+e^- cross section.

9 Luminosity Measurement and Normalization

The luminosity in a collider can be measured either through direct measurement of beam parameters or from the measurement of a process with a known rate. CDF has chosen to use a combination of these methods to measure the integrated luminosity recorded during the 1988-1989 data run.

The Tevatron was run at two different energies, $\sqrt{s} = 546$ GeV and $\sqrt{s} = 1800$ GeV. The majority of running was done at the higher energy, with an integrated luminosity of ~ 4.0 pb^{-1} at $\sqrt{s} = 1800$ GeV and ~ 10 nb^{-1} at $\sqrt{s} = 546$ GeV. All the data discussed in other sections of this paper came with the Tevatron running at the higher beam energy.

We have used the interaction rate as measured in the BBCs at both energies, in conjunction with the beam parameters measured by the Fermilab Accelerator division and the $\bar{p}p$ cross sections measured by UA4 at the S$\bar{p}p$S collider at CERN [40], to calibrate our luminosity measurement. The current method does not depend heavily upon a Monte Carlo calculation since the Monte Carlo enters principally through computation of the ratio of geometric acceptance in the two experiments.

9.1 Luminosity Measurement

The Beam Beam Counters, scintillator planes located 5.8 m from the nominal interaction point along the beam axis, serve as the luminosity monitors for CDF. The CDF trigger system required a coincidence of hits in the east (proton direction) and west (anti-proton direction) BBCs. By monitoring the rate of hits in these counters, we have a process to which we can normalize all other cross section measurements. To get an absolute normalization of the BBC cross section (σ_{BBC}), we use the rate seen in these counters and the luminosity measured with beam parameters. In previous work, CDF has used a nominal value of $\sigma_{BBC} = 44 \pm 6.6$ mb [36].

The transverse profile of the beam is measured with flying wires – wires moved through the beam [41]. Current monitors measures both bunch intensities and the longitudinal profile [42]. The luminosity at CDF is calculated with these parameters and knowledge of the accelerator lattice function. Uncertainties in this calculation come from measurement errors, calibration uncertainty, and uncertainties in the lattice function. The overall uncertainty is estimated to be 10% [43]. This uncertainty is energy independent.

At both $\sqrt{s} = 546$ GeV and $\sqrt{s} = 1800$ GeV, we measure the beam parameters and the rate in the BBCs. We are then able to measure how σ_{BBC} changes with $\sqrt{s}$, via the ratio of the accelerator luminosity calculated from beam parameters. This ratio has a systematic uncertainty free from the overall normalization uncertainty. By normalizing at $\sqrt{s} = 546$ GeV, where previous measurements with similar geometry have been made, we can measure the effective cross section seen by the BBCs at $\sqrt{s} = 1800$ GeV and extract the integrated luminosity recorded.

9.2 Normalization

We have selected a series of accelerator fills where the data are internally consistent. Many of the variables that we are interested in have to be reconstructed from other measurements (e.g. horizontal and vertical emittances of the beam). To do this reconstruction

accurately required an understanding of the accelerator conditions and programs at the time the data were taken [44]. This selection is independent of the detector status at CDF.

In figure 17, we show a distribution of the rate as measured with the BBCs (R_{BBC}) compared to the luminosity as measured with accelerator parameters (L_{acc}) for both $\sqrt{s} = 1800$ GeV and $\sqrt{s} = 546$ GeV. We then use the relation

$$\frac{\sigma_{BBC}^{1800}}{\sigma_{BBC}^{546}} = \frac{R_{BBC}(1800)}{R_{BBC}(546)} \frac{L_{acc}(546)}{L_{acc}(1800)} \tag{10}$$

to extrapolate the σ_{BBC} from 546 GeV to 1800 GeV. The ratio $\frac{R_{BBC}}{L_{acc}}$ at 1800 GeV has been corrected by -3 $\pm$ 2% for dynamic beam–beam interaction effects, which change the focal properties of the Tevatron lattice [45]. These effects predict a linear dependence of the ratio with L, which is seen in the data (figure 18). The correction is extrapolated to low luminosity where the beam–beam effects are found to be negligible.

We use two methods to calculate σ_{BBC}^{546}. The first is to use the luminosity as calculated from beam parameters and the accelerator lattice. This method gives an effective beam beam counter cross section of 32.8 $\pm$ 3.6 mb. The second method is to use values reported by the UA4 collaboration.

The UA4 experiment used trigger counters similar in geometry to the BBCs used by CDF. From their measurements of ρ, σ_{el}, and σ_{tot}, and the double arm fraction (f_{DA}) [46] of the UA4 trigger counters [40], we define

$$\sigma_{UA4}^{obs} = (1 - \frac{\sigma_{el}}{\sigma_{tot}}) \cdot \sigma_{tot} \cdot f_{DA}. \tag{11}$$

We calculate $\sigma_{UA4}^{obs} = 38.9 \pm 1.8$ mb [47]. Using the MBR Monte Carlo [48], we then calculate the relative acceptance of the CDF BBCs in comparison to the UA4 trigger counters. This correction is necessary since the UA4 trigger counters cover a different geometric area ($3.0 < |\eta| < 5.6$) than the BBCs. The correction due to different η coverage is -2.5 $\pm$ 2.5%. We also correct for the inefficiencies in the BBCs due to radiation damage suffered during the course of the data taking. Radiation damage and its effects at 1800 GeV are measured

from data triggered solely on beam crossings. The magnitude of this correction at 1800 GeV is -0.7%. This inefficiency is extrapolated to 546 GeV using the MBR Monte Carlo, giving an inefficiency of 2.2 ± 2.2%. The value for σ_{BBC}^{546} from this method is 37.1 ± 2.1 mb.

To derive the final value of σ_{BBC}^{546}, we average the measurements from the accelerator calculation and the UA4 normalization weighted by their respective errors. In summary, $\sigma_{BBC}^{546} = 36.0 \pm 1.8$ mb, where the answer is dominated by the UA4 normalization. We calculate $\sigma_{BBC}^{1800} = 46.8 \pm 3.2$ mb. We wish to stress that this normalization is not a physical cross section, but a visible cross section not directly related to underlying physics models (because of secondary interactions, photon conversions, etc.). This method depends upon the similarity of the CDF luminosity monitors to the UA4 counters and the ability to use the information from the accelerator measurement of the luminosity.

9.3 Cross Checks

As the instantaneous luminosity grows, the rate of bunch crossings with multiple interactions also grows. Using Poisson statistics, we can estimate the probability of having 2 or 3 interactions in a bunch crossing. We find that the ratio of the probability of having 2 interactions to the probability of having 1 interaction is predicted to be $1.75 \times 10^{-6} \times R_{BBC}$, where R_{BBC} is the rate in the BBCs in Hertz (this number is directly related to the 3.5 μsec between beam crossings). We use this prediction to make a correction (on the order of 9% at 50 kHz) to the measured rate in the BBCs to account for multiple interactions.

The ratio of the number of events with two vertices to those with one vertex as a function of the rate in the BBCs is a check on the BBC cross section. To do this properly, we must first correct for inefficiencies in vertex finding. The CDF vertex finding algorithm has inefficiencies in resolving multiple vertices if the separation of the vertices in Z is too small. We calculate the efficiency for finding secondary vertices using the distribution of the 2 vertex separation from multiple vertex events in the inclusive central electron sample (described in section 4.5), including the assumption that the vertex distribution is Gaussian with $\sigma = 30$ cm. Figure 19 shows the efficiency as a function of the vertex separation.

Figure 20 shows the ratio of the number of events with 2 vertices to those with 1 vertex as a function of the R_{BBC}. The number of 2 vertex events has been corrected for the inefficiency in finding a second vertex. A linear fit gives a slope of $(1.91 \pm 0.08) \times 10^{-6}$, within 2σ of the predicted value of 1.75×10^{-6}.

10 Results and Conclusions

10.1 Cross Sections

The expression for the cross section takes into account the background, efficiencies, acceptances, and integrated luminosity through the following formula

$$\sigma \cdot \mathrm{B}(W \rightarrow \mathrm{e}\,\nu) = \frac{\text{Candidates} - \text{Background}}{\int Ldt \cdot \epsilon \cdot A} \tag{12}$$

where ϵ is the selection efficiency and A is the acceptance. For the measurement of the cross-sections for the production of W ($\sigma \cdot \mathrm{B}(W \rightarrow \mathrm{e}\,\nu)$) and Z^0 ($\sigma \cdot \mathrm{B}(Z^0 \rightarrow \mathrm{e^+e^-})$) bosons, we use the number of candidates, backgrounds, efficiencies, and acceptances as summarized in table 11. A straightforward application of equation 12 leads to the following results.

The final cross section times branching ratio for W production and subsequent decay to electron and neutrino is $\sigma \cdot \mathrm{B}(W \rightarrow \mathrm{e}\,\nu) = 2.19 \pm 0.04$ (stat) $\pm$ 0.21 (sys) nb. The dominant systematic error in the determination of $\sigma \cdot \mathrm{B}(W \rightarrow \mathrm{e}\,\nu)$ is the 6.8% error in the luminosity normalization. The final cross section times branching ratio for Z^0 production and subsequent decay into electrons is $\sigma \cdot \mathrm{B}(Z^0 \rightarrow \mathrm{e^+e^-}) = 0.209 \pm 0.013$ (stat) $\pm$ 0.017 (sys) nb, where the luminosity normalization uncertainty dominates the systematic error.

Figure 21 shows a comparison of the CDF measured values for $\sigma \cdot \mathrm{B}(W \rightarrow \mathrm{e}\,\nu)$ and $\sigma \cdot \mathrm{B}(Z^0 \rightarrow \mathrm{e^+e^-})$ to theoretical predictions [49]. Included on this plot are recent values for $\sigma \cdot B(W \rightarrow e\nu)$ and $\sigma \cdot B(Z^0 \rightarrow e^+e^-$ at $\sqrt{s} = 630$ GeVfrom the UA2 collaboration [50]. The theoretical predictions used $M_W = 80$ GeV/c^2 and $M_Z = 91.1$ GeV/c^2 and assumed that the decay channels into top were closed.

In a previous publication [51], a different assumption on the W branching ratio into

electrons was made (we assumed a top mass of 45 GeV/c^2). This assumption affects the theoretical prediction more than the experimental measurement, since the top mass affects the branching ratio into electrons. Recent measurements by CDF [8,35] and UA2 [52] on both the W and top quark masses have helped reduce theoretical uncertainties in the prediction of the product of the cross section and branching ratio. The changed assumptions increase the predicted cross section, bringing it closer into agreement with previously measured values. The current theoretical predictions agree quite well with the most recent experimental measurements at both $\sqrt{s} = 630$ GeV and $\sqrt{s} = 1800$ GeV.

10.2 The ratio $R = \sigma \cdot B(W \rightarrow e\,\nu)\ /\ \sigma \cdot B(Z^0 \rightarrow e^+e^-)$ and the W width

The ratio, R, of $\sigma \cdot B(W \rightarrow e\,\nu)$ to $\sigma \cdot B(Z^0 \rightarrow e^+e^-)$ and the individual cross sections themselves are interdependent quantities. However, from the perspective of experimental measurement, they can be considered as three separate quantities. In a previous publication [53], CDF has presented a measurement of $R = 10.2 \pm 0.8$ (stat) $\pm$ 0.4 (sys). In that measurement, we applied event selection criteria designed to minimize the systematic uncertainties in the ratio. In order to lower backgrounds and minimize systematic uncertainties, events with energy clusters (jets) other than the electrons from W and Z^0 decays were rejected in the analysis.

Such a requirement is optimal for measuring the cross section ratio, where the numerator and denominator are affected almost equally, but is not adequate for the independent measurements of the numerator and the denominator, as events which contribute to the cross section have been excluded by the 'no jet' cut. Allowing for the presence of energetic clusters in addition to identified electrons has increased the size of the W and Z^0 datasets (thus decreasing the statistical error) but has also increased the levels of background in the samples. Uncertainty in the level of the background also increases significantly. Taking the individual cross sections reported in section 10.1 and taking into account the correlated errors in the two measurements we find a value of $R = 10.5 \pm 0.7$ (stat) $\pm$ 0.6 (sys). Due to the increased systematic error in this new number, we believe that the previous measure-

ment $R = 10.2 \pm 0.8$ (stat) $\pm$ 0.4(sys) documented in reference [53] still contains our best knowledge of the ratio of the cross sections and should be the number used for R.

The ratio, R, can be expressed as [54]

$$R = \frac{\sigma(W \rightarrow e\nu)}{\sigma(Z^0 \rightarrow e^+e^-)} = \frac{\sigma(\bar{p}p \rightarrow WX)}{\sigma(\bar{p}p \rightarrow Z^0X)} \frac{\Gamma(W \rightarrow e\nu)}{\Gamma(Z^0 \rightarrow e^+e^-)} \frac{\Gamma(Z^0)}{\Gamma(W)}. \quad (13)$$

From R, either the ratio of total widths $\Gamma(Z^0)/\Gamma(W)$ or the branching ratio for W into electrons can be extracted with the knowledge of the ratio of production cross sections [55], the partial and total widths of the Z^0, and the partial widths of the W .

Using our value for $R = 10.2 \pm 0.8$ (stat) $\pm$ 0.4 (sys), predicted values of the production cross section ratio $\sigma(\bar{p}p \rightarrow WX)/\sigma(\bar{p}p \rightarrow Z^0X) = 3.23 \pm 0.03$ [55] and $\Gamma(W \rightarrow e\nu)/\Gamma(Z^0 \rightarrow e^+e^-) = 2.70 \pm 0.02$ [56], and the measured value of $\sin^2\theta_W = 0.229 \pm 0.007$ [32], we extract $\Gamma(W)/\Gamma(Z^0) = 0.85 \pm 0.08$. Using the latest value for $\Gamma(Z^0) = 2.496 \pm 0.016$ GeV [57], we extract $\Gamma(W) = 2.12 \pm 0.20$. The Standard Model prediction with $M_W = 80.0$ GeV/c^2, $\alpha_s = 0.13$, and $M_{top} > M_W - M_b$ is $\Gamma(W) = 2.07$ GeV. This value for $\Gamma(W)$ has changed since reference [53] due to the new measurements of $\Gamma(Z^0)$ at LEP.

Recent searches have set preliminary lower limits on M_{top} up to 89 GeV/c^2 assuming Standard Model decays [38,35] and limits up to $\sim$ 46 GeV/c^2 independent of decay mode [57]. Figure 22 shows a prediction for the ratio $\Gamma(W)/\Gamma(W \rightarrow e\nu)$ as a function of the top mass. From the values quoted above and $\Gamma(Z^0 \rightarrow e^+e^-) = 83.7 \pm 0.7$ MeV [57], we find that $\Gamma(W)/\Gamma(W \rightarrow e\nu) = 9.47 \pm 0.86$. This value excludes M_{top} below 49 (44) GeV/c^2 at the 90% (95%) confidence level independent of the decay modes of the top quark [58]. We use the inverse of the branching ratio since it depends only weakly on the W mass. Again, the limit has improved due to the new measurements at LEP of $\Gamma(Z^0)$ and $\Gamma(Z^0 \rightarrow e^+e^-)$.

10.3 Final Numbers

The final cross section times branching ratio for W production and subsequent decay to electron and neutrino is $\sigma \cdot B(W \rightarrow e\,\nu) = 2.19 \pm 0.04$ (stat) $\pm$ 0.21 (sys) nb. The dom-

inant systematic error in the determination of $\sigma \cdot B(W \rightarrow e\ \nu)$ is the 6.8% error in the luminosity normalization. The final cross section times branching ratio for Z^0 production and subsequent decay into electrons is $\sigma \cdot B(Z^0 \rightarrow e^+e^-) = 0.209 \pm 0.013$ (stat) $\pm$ 0.017 (sys) nb, where the luminosity normalization uncertainty dominates the systematic error.

Combining knowledge of the proton structure functions, W and Z^0 couplings, and QCD corrections leads to predictions of the cross section for production and decay of W and Z^0 bosons in $\bar{p}p$ collisions. We have shown that the predictions are consistent with experimentally measured quantities.

11 Acknowledgements

We thank the Fermilab Accelerator Division and the staffs at our individual institutions for their exceptional performance. We thank Norman Gelfand, Jon Rosner, James Stirling, and Alan Martin for advice and encouragement. This work was supported by the U.S. Department of Energy, the National Science Foundation, the Istituto Nazionale di Fisica Nucleare, the Ministry of Science, Culture and Education of Japan, and the A.P. Sloan Foundation.

(a) Permanent address: Albert-Ludwig University, Freiburg, Germany.

(b) Permanent address: University of Oxford, Oxford, England.

(c) Permanent address: University di Bologna, Bologna, Italy.

System	η Range	Energy Resolution	Position Resolution	Thickness
CEM	$\lvert\eta\rvert < 1.1$	$13.5\%/\sqrt{E_T} \oplus 2\%$	0.2 cm by 0.2 cm	18 X_0
PEM	$1.1 < \lvert\eta\rvert < 2.4$	$28\%/\sqrt{E} \oplus 2\%$	0.2 cm by 0.2 cm	18-21 X_0
FEM	$2.2 < \lvert\eta\rvert < 4.2$	$25\%/\sqrt{E} \oplus 2\%$	0.1 cm to 0.4 cm	25 X_0

Table 1: Summary of CDF calorimeter properties. The symbol $\oplus$ signifies that the constant term is added in quadrature in the resolution. Thicknesses are given in radiation lengths.

E_T	>	20.0 GeV
Iso	<	0.1
Had/Em	<	0.055 + 0.045×E/100
χ^2_{Strip}	<	15.0
$Lshr$	<	0.2
E/p	<	1.5
$\lvert\Delta Z\rvert$	<	3.0 cm
$\lvert\Delta R\phi\rvert$	<	1.5 cm
$\lvert Z_{vert}\rvert$	<	60.0 cm

Table 2: Summary of common central electron selection requirements.

P.S.F	$A_W(\%)$	$A_Z(\%)$	F_{cc}	F_{cp}	F_{cf}
MRSE	35.7 ± 0.1	36.5 ± 0.1	0.39	0.47	0.14
MRSB	35.2 ± 0.1	37.1 ± 0.1	0.40	0.47	0.13
DO1	34.0 ± 0.1	37.0 ± 0.1	0.40	0.46	0.14
EHLQ1	35.9 ± 0.1	37.2 ± 0.1	0.39	0.47	0.14

Table 3: Acceptances for the W and Z^0 for various sets of parton structure functions (P.S.F.). We also include the fractions of central–central, central–plug, and central–forward events expected for Z^0 events.

Source of Systematic Error	Uncertainty in A_W	Uncertainty in A_Z
Structure Functions	±1.1%	±0.3%
Mass	±0.3%	
p_T	±0.4%	±0.4%
Higher Order Terms	±0.9%	±0.4%
Total	±1.5%	±0.7%

Table 4: Contributions to systematic uncertainties in the calculation of acceptances.

Quantity	$\not\!\!E_T$ sample (1187 events)	Z^0 sample (87 events)
Iso	0.96 ± 0.01	0.97 ± 0.01
Had/Em	0.99 ± 0.01	0.99 ± 0.01
χ^2_{Strip}	0.97 ± 0.01	0.97 ± 0.01
$Lshr$	0.97 ± 0.01	0.99 ± 0.01
E/p	0.93 ± 0.01	0.93 ± 0.02
ΔZ	0.98 ± 0.01	0.99 ± 0.01
$\Delta R\phi$	0.97 ± 0.01	0.97 ± 0.01
Trigger	0.973 ± 0.005	0.973 ± 0.005
All	0.84 ± 0.03	0.85 ± 0.03

Table 5: The individual electron selection efficiencies for the $\not\!\!E_T$ selected sample and the Z^0 samples for the common central electron selection, c_1. The efficiency for the combination of all the cuts, including the trigger, is 0.84 ± 0.03.

Quantity	$\not\!\!E_T$ sample (1187 events)	Z^0 sample (87 events)
Iso	0.96 ± 0.01	0.97 ± 0.01
Had/Em	0.99 ± 0.01	0.99 ± 0.01
E/p	0.97 ± 0.01	0.96 ± 0.02
All	0.93 ± 0.03	0.93 ± 0.03

Table 6: The electron selection efficiencies for the $\not\!\!E_T$ selected sample and the Z^0 samples for the loose central electron selection, c_2. Listed in the table are the individual efficiencies for each cut. The combined efficiency is 0.93 ± 0.03.

Quantity	$\not\!\!E_T$ sample (500 events)	Z^0 sample (76 events)
Iso	0.96 ± 0.01	0.93 ± 0.03
Had/Em	0.99 ± 0.01	0.99 ± 0.01
$3x3$ χ^2	0.94 ± 0.01	0.99 ± 0.01
VTPC Hit Fraction	0.93 ± 0.02	0.96 ± 0.02
All	0.90 ± 0.03	0.92 ± 0.03

Table 7: The electron selection efficiencies for the $\not\!\!E_T$ selected sample and the Z^0 samples for the plug electron selection, p.

Quantity	$\not\!\!E_T$ sample (135)	Z^0 sample (19 events)
Iso	0.91 ± 0.03	0.90 ± 0.07
Had/Em	1.00 ± 0.01	0.95 ± 0.05
All	0.91 ± 0.04	0.89 ± 0.07

Table 8: The electron selection efficiencies for the $\not\!\!E_T$ selected sample and the Z^0 samples for the forward electron selection, f.

	0 Jets	1 Jet	$\geq$ 2 Jets
ϵ_ν	0.98 $\pm$ 0.01	0.90 $\pm$ 0.02	0.88 $\pm$ 0.02
Fraction (data)	72%	20%	8%
Fraction (Monte Carlo)	74%	21%	5%

Table 9: The $\not\!\!E_T$ efficiency as a function of the number of jets with $E_T > 10$ GeV in the event and the fraction of events with 0, 1, or $\geq$ 2 jets.

	Efficiency
c_1	0.84 $\pm$ 0.03
c_2	0.93 $\pm$ 0.03
p	0.91 $\pm$ 0.03
f	0.91 $\pm$ 0.04
ϵ_ν	0.96 $\pm$ 0.02
ϵ_W	0.81 $\pm$ 0.04
ϵ_Z	0.80 $\pm$ 0.03

Table 10: The selection efficiencies for the W and Z^0 samples.

	W Events	Z Events
Candidates	2664	243
Background		
QCD	100 ± 50	5 ± 3
$W \rightarrow \tau\ \nu$	90 ± 10	-
$Z^0 \rightarrow e^+e^-$	40 ± 15	-
$Z^0 \rightarrow \tau^+\tau^-$	8 ± 4	< 0.5
top	0 + 31 - 0	-
Total	238 + 62 - 53	5 ± 3
Signal	$2426 \pm 52 + 53 - 62$	$238 \pm 16 \pm 3$
Acceptance	0.352 ± 0.015	0.371 ± 0.007
F_{cc}	-	0.40
F_{cp}	-	0.47
F_{cf}	-	0.13
c_1	0.84 ± 0.03	0.84 ± 0.03
c_2	-	0.93 ± 0.03
p	-	0.91 ± 0.03
f	-	0.91 ± 0.04
ϵ_ν	0.96 ± 0.02	-
ϵ_W, ϵ_Z	0.81 ± 0.04	0.80 ± 0.03
Drell-Yan Correction	-	1.01 ± 0.01
Z-vertex Efficiency	0.959 ± 0.005	0.959 ± 0.005
Luminosity	4.05 ± 0.28 pb^{-1}	4.05 ± 0.28 pb^{-1}
Cross Sections	$2.19 \pm 0.04 \pm 0.21$ nb	$0.209 \pm 0.013 \pm 0.017$ nb

Table 11: Summary of results.

References

[1] S.L. Glashow, Nucl. Phys. **22**, 579 (1961); S. Weinberg, Phys. Rev. Lett. **19**, 1264 (1967); A. Salam, in *Elementary Particle Physics*, ed. by N. Svartholm (Almqvist and Wiksells, Stockholm, 1968), p. 367.

[2] Y. Yamaguchi, Il Nuovo Cimento **43A**, 193 (1966); S.D. Drell and T-M. Yan, Phys. Rev. Lett. **25**, 316 (1970).

[3] L.M. Lederman, and B.G. Pope, Phys. Rev. Lett. **27**, 765 (1971); R.B. Palmer, E.A. Paschos, N.P. Samios, and Ling-Lie Wang, Phys. REv. D **14**, 118 (1972); C. Quigg, Rev. Mod. Phys. **49**, 297 (1977).

[4] G. Altarelli, K. Ellis, M. Greco, and G. Martinelli, Nucl. Phys. **B246**, 12 (1984); G. Altarelli, K. Ellis, and G. Martinelli, Z. Phys. C. **27**, 617 (1985).

[5] F. Abe, et al., Nucl. Instr. and Meth. **A271** (1988) 387.

[6] The CDF coordinate system defines Z along the proton-beam direction, θ as the polar angle, and ϕ as the azimuthal angle. The pseudorapidity, η, is defined $\eta = -\ln(\tan(\frac{\theta}{2}))$

[7] L. Balka, et al., Nucl. Instr. and Meth. **A267** (1988) 272.

[8] F. Abe, et al., submitted to Phys. Rev. D.

[9] Y. Fukui, et al., Nucl. Instr. and Meth. **A267** (1988) 280.

[10] G. Brandenburg, et al., Nucl. Instr. and Meth. **A267** (1988) 257.

[11] S. Bertolucci, et al., Nucl. Instr. and Meth. **A267** (1988) 301.

[12] W. Carithers, et al., to be submitted to Nucl. Instr. and Meth.

[13] S. Cihangir, et al., Nucl. Instr. and Meth. **A267** (1988) 249.

[14] P. Hurst, Ph.D. thesis, University of Illinois, 1990 (unpublished).

[15] F. Snider, et al., Nucl. Instr. and Meth. **A268** (1988) 75.

[16] F. Bedeschi, et al., Nucl. Instr. and Meth. **A268** (1988) 50.

[17] F. Abe, et al., to be submitted to Nucl. Instr. and Meth.

[18] D. Amidei, et al., Nucl. Instr. and Meth. **A269** (1988) 51.

[19] G.W. Foster, et al., Nucl. Instr. and Meth. **A269** (1988) 93.

[20] M. Miller, Ph.D. Thesis, University of Pennsylvania, 1989 (unpublished).

[21] We do not use this definition of E_T in our calculation of the isolation. We use the cluster E_T for this calculation, defined from the calorimeter position, the event vertex, and the beam direction.

[22] K. Yasuoka, et al., Nucl. Instr. and Meth. **A267** (1988) 315.

[23] R.G. Wagner (unpublished), based on calculations by F. Berends et al., Z. Phys. C **27**, 155 (1985); F. Berends and R. Kleiss, Z. Phys. C **27**, 365 (1985).

[24] J. Proudfoot, for the Proceedings of the Workshop on Calorimetry for the Superconducting Supercollider, ANL-HEP-CP-89-40-mc (microfiche) March 1989.

[25] E. Kearns, Ph.D. Thesis, Harvard University, 1990 (unpublished).

[26] Note that this threshold is in tower energy, not tower transverse energy.

[27] A.D. Martin, R.G. Roberts, and W.J. Stirling, Mod. Phys. Lett. A 4, 1135 (1989).

[28] D. Duke and J. Owens, Phys. Rev. D **30**, 49 (1984).

[29] E. Eichten, I. Hinchliffe, K. Lane, and C. Quigg, Rev. Mod. Phys. **56**, 579, (1984).

[30] F. Paige and S.D. Protopopescu, ISAJET Monte Carlo Version 6.21, BNL Report No. BNL38034, 1986 (unpublished).

[31] Ian Hinchliffe (private communication). We used Version 3.08.

[32] U. Amaldi, et al., Phys. Rev. D **36**, 1385 (1987).

[33] G. Altarelli, et al., Nucl. Phys. **246B**, 12 (1984).

[34] The transverse mass is defined to be $\sqrt{E_T \not{E}_T(1-\cos\alpha)}$, where α is the azimuthal angle between the electron E_T and $\not{E}_T$.

[35] F. Abe, et al., submitted to Phys. Rev. D.

[36] F. Abe, et al., Phys. Rev. Lett. **62**, 613 (1989).

[37] If the event fractions (corrected for efficiencies) seen in data are used rather than the expected fractions, the value for ϵ_Z is 0.81 ± 0.05, where the increase in the uncertainty comes from the limited statistics of the data sample.

[38] K. Sliwa, in Proceedings of the 25th Moriond Conference, Hadronic Session, Les Arcs, France, March 1990 (to be published).

[39] G. Altarelli, et al., Nucl. Phys. **B308** 724 (1988).

[40] M. Bozzo, et al., Phys. Lett. **147B** 392 (1984).

[41] J. Gannon, et al., "Flying Wires at Fermilab", Proc. 1989 IEEE Part. Acc. Conf., Chicago (1989), p. 68.

[42] C.D. Moore, et al., "Single Bunch Intensity Monitoring System using an Improved Wall Current Monitor", Proc. 1989 IEEE Part. Acc. Conf., Chicago (1989), p. 1513.

[43] C. Grosso-Pilcher and S. White, Fermilab Note FN-550, Oct. 1990.

[44] We wish to thank the Fermilab Accelerator Division, especially N. Gelfand, for the help in understanding the accelerator data.

[45] D. Johnson, Fermilab Technical Memo TM-1554, Jan. 1989.

[46] We have taken f_{DA} from Table 1 of reference [40] and interpret it as the fraction of the total inelastic cross section seen in the UA4 trigger counters.

[47] We have used $\frac{\sigma_{el}}{\sigma_{tot}} = 0.215$, $\sigma_{tot} = 59.5 \pm 1.4 \pm 1.2$ mb, and $f_{DA} = 0.827$.

[48] S. Belforte, private communication.

[49] K. Ellis, in Proceedings of the Eighth Topical Workshop on Proton-Antiproton Physics, Castiglione, Italy, September 1989 (to be published).

[50] J. Alitti, et al., CERN-EP/90-20, Feb. 1990, submitted to Z. Phys. C.

[51] F. Abe, et al., Phys. Rev. Lett. **62**, 1005 (1989).

[52] J. Alitti, et al., CERN-EP/90-22, Feb. 1990, submitted to Phys. Lett. B.

[53] F. Abe, et al., Phys. Rev. Lett. **64**, 157 (1990).

[54] F. Halzen and M. Mursula, Phys. Rev. Lett. **51**, 857 (1983); K. Hikasa, Phys. Rev. D **29**, 1939 (1984); N.G. Deshpande et al., Phys. Rev. Lett. **54**, 1757 (1985); A.D. Martin, R.G. Roberts, and W.J. Stirling, Phys. Lett. **189B**, 220 (1987); E.L. Berger, F. Halzen, C.S. Kim, and S. Willenbrock, Phys. Rev. D **40**, 83 (1989).

[55] A.D. Martin, W.J. Stirling, and R.G. Roberts, Phys. Lett. **228B**, 149 (1989).

[56] We use $\Gamma(Z^0 \rightarrow e^+e^-) = 82.8 \pm 0.6$ MeV; see W.F.L. Hollik, DESY Report No. 88-188, 1988 (unpublished).

[57] F. Dydak, in Proceedings of the 25th International Conference on High Energy Physics, Singapore, August, 1990 (to be published).

[58] We used the method of the Particle Data Group, M. Aguilar, et al., Phys. Lett. **204B**, (1988), for extracting limits in the case of bounded physical regions.

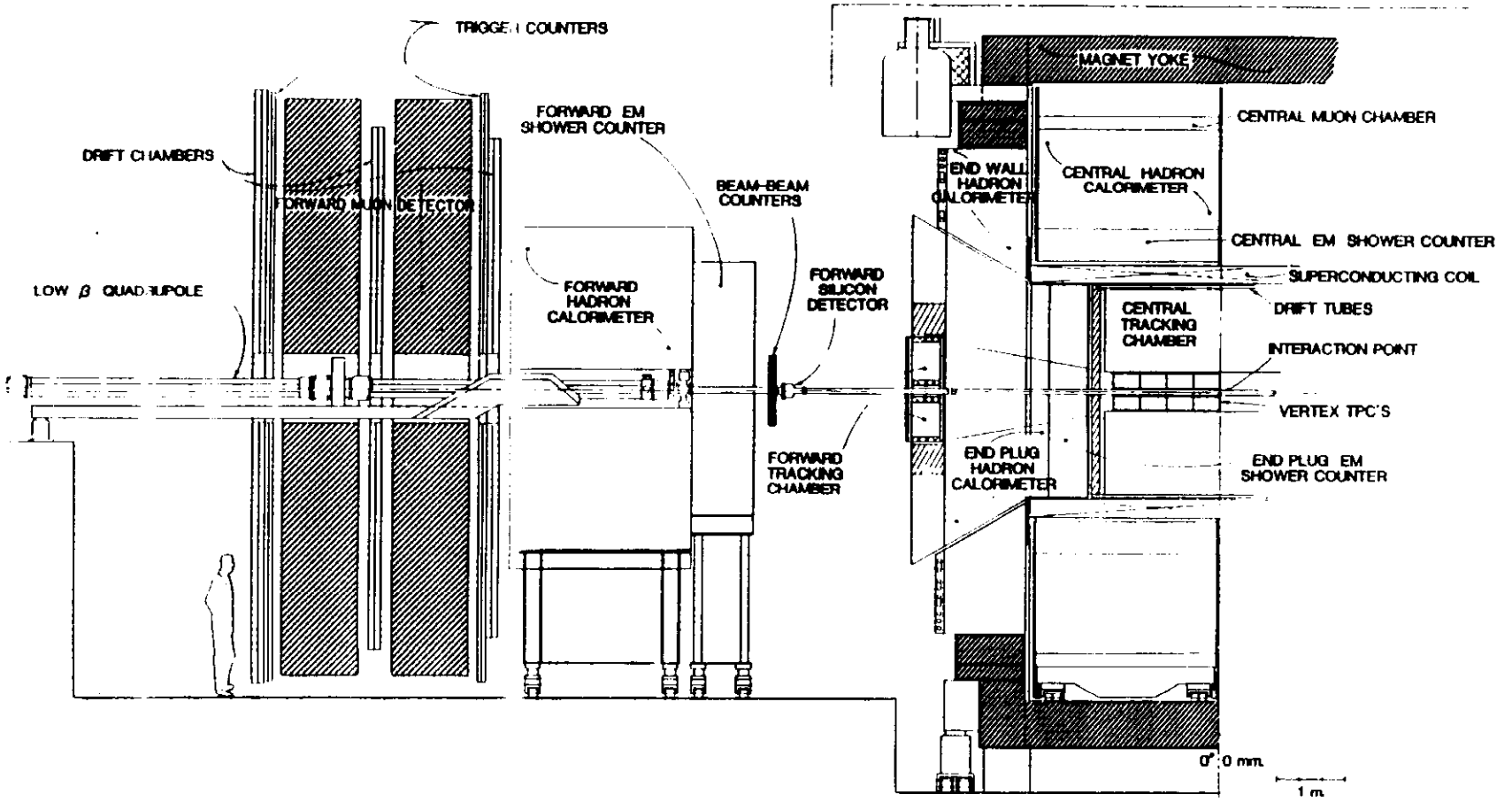

Figure 1: A side view of one half of the CDF detector. It is symmetric about the $\eta = 0$ plane.

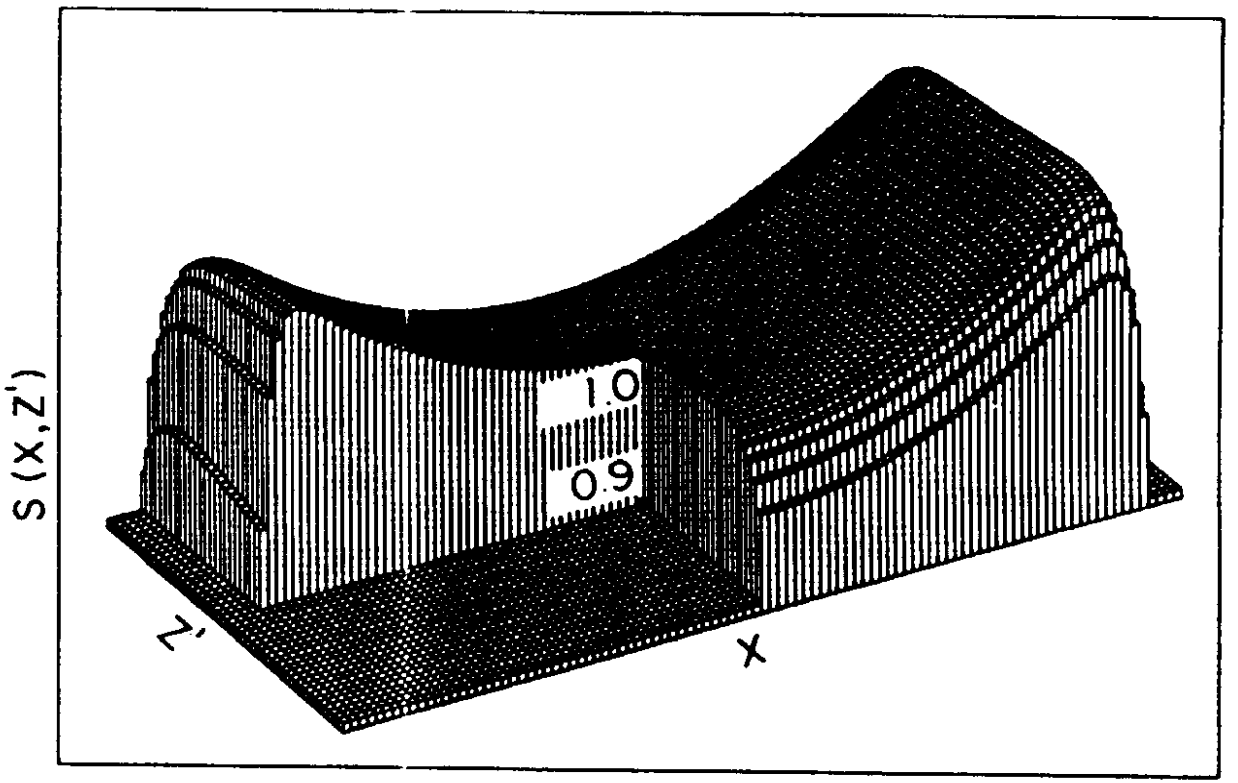

Figure 2: Relative response in a central calorimeter tower. The Z' axis is in the beam direction and the X axis is in the azimuthal direction. The point labeled 1.0 is the point at which the tower is calibrated – the vertical scale gives the relative response.

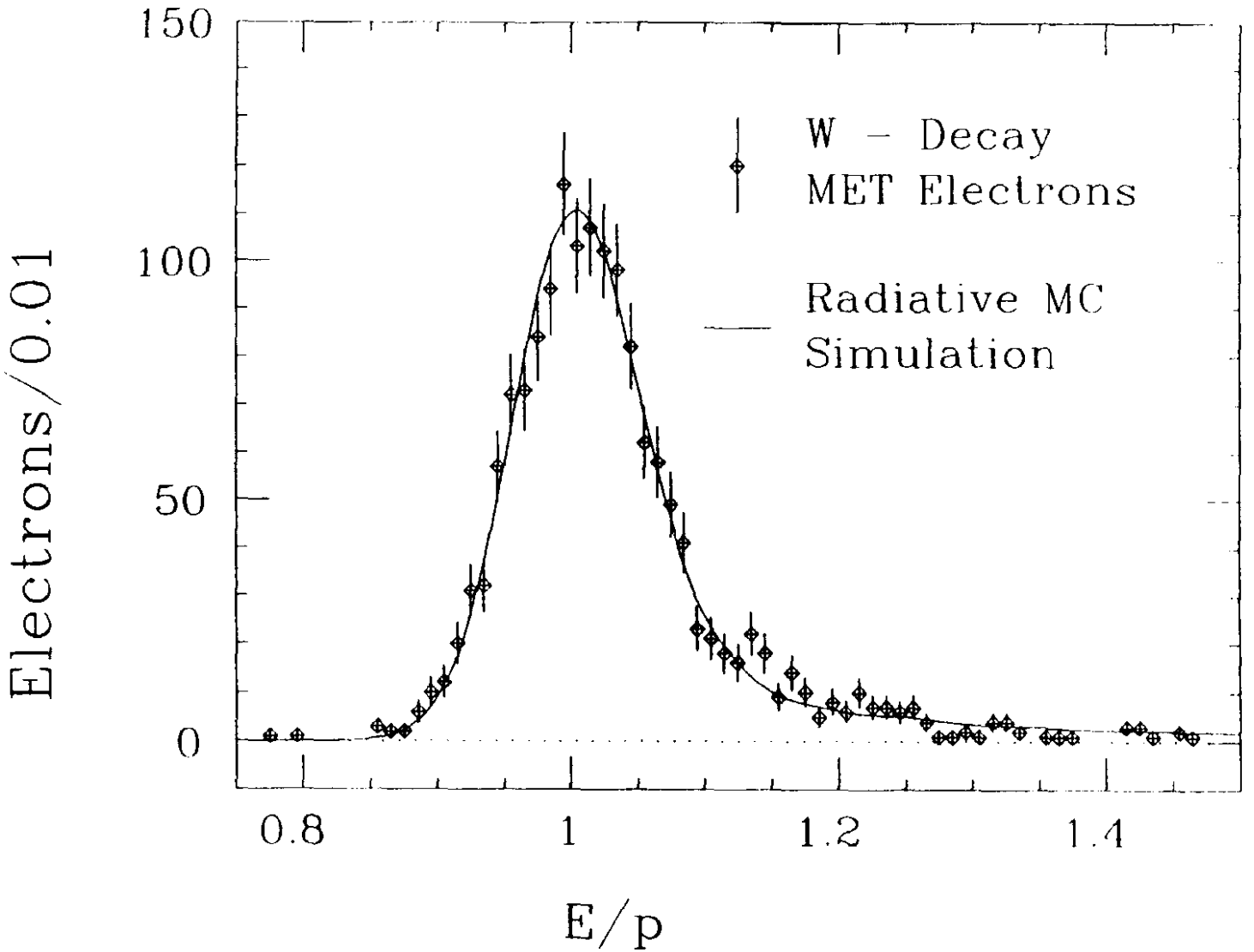

Figure 3: E/p distributions from data and a radiative Monte Carlo. The overall response scale is set by a comparison of these two distributions.

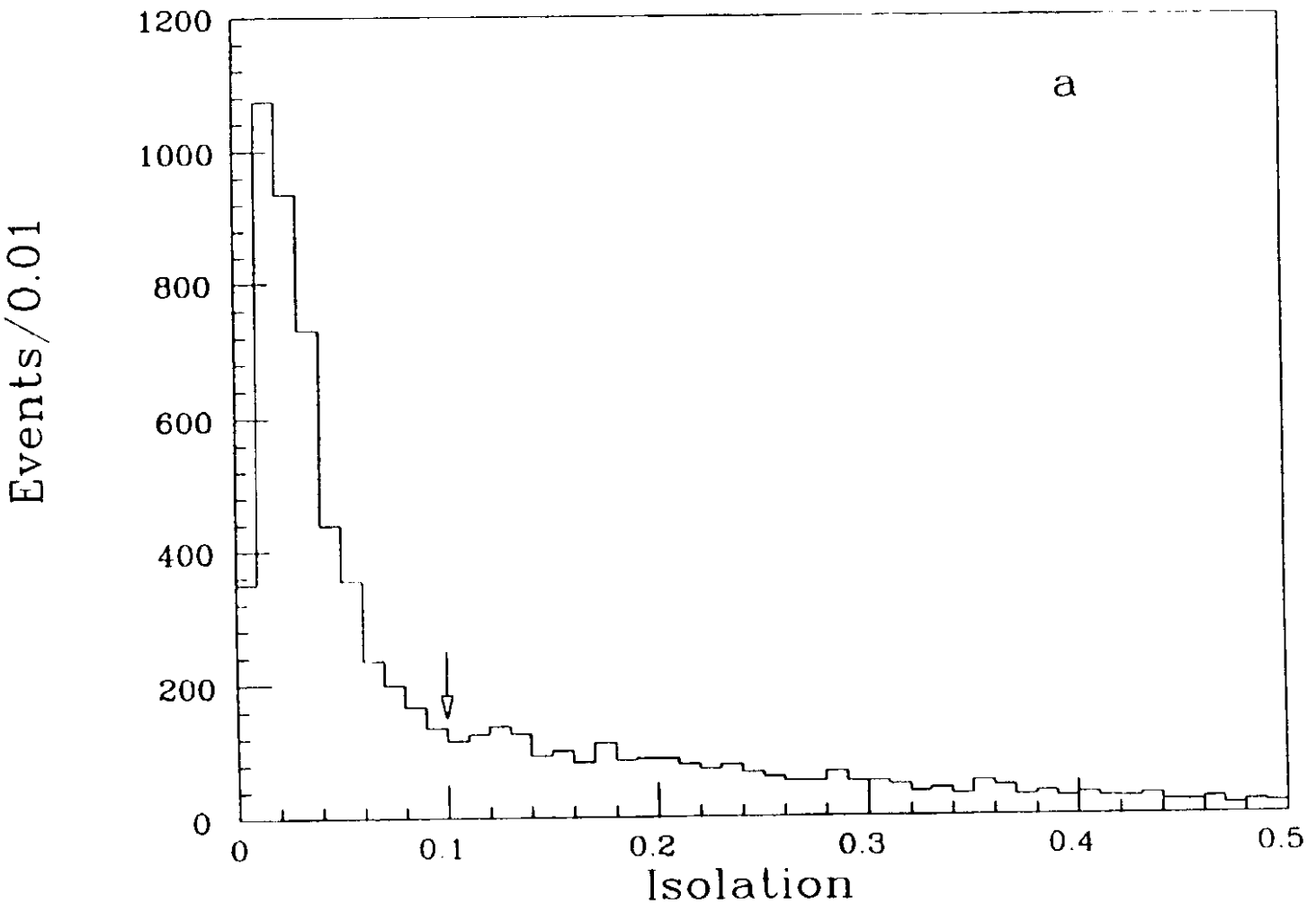

Figure 4: Distributions of the variables used in the central electron selection. These are the distributions after all cuts but the one plotted have been applied. The arrows represent the cut values.

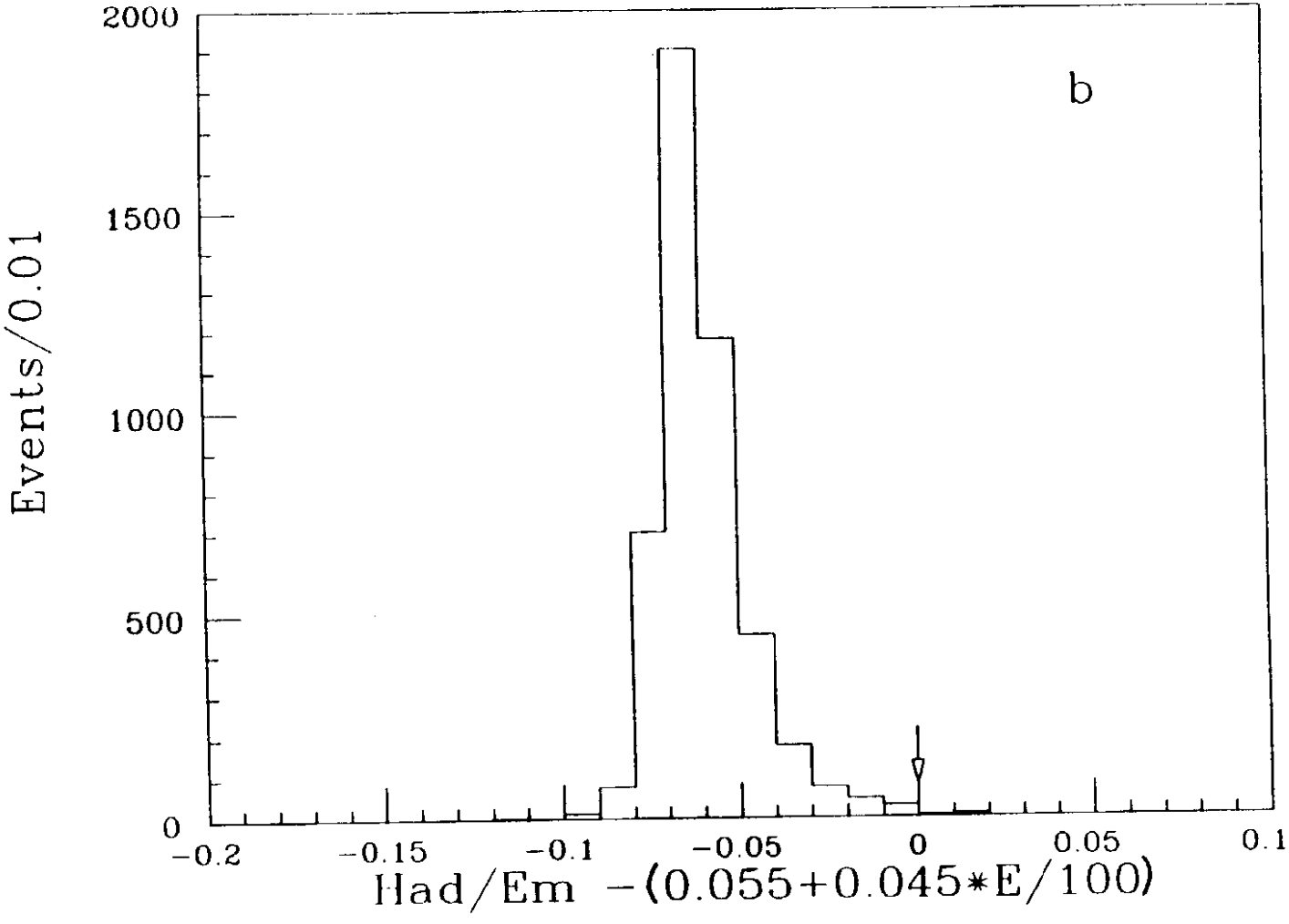
b
2000
1500
1000
500
0
Events/0.01
−0.2
−0.15
−0.1
−0.05
0
0.05
0.1
Had/Em −(0.055+0.045*E/100)

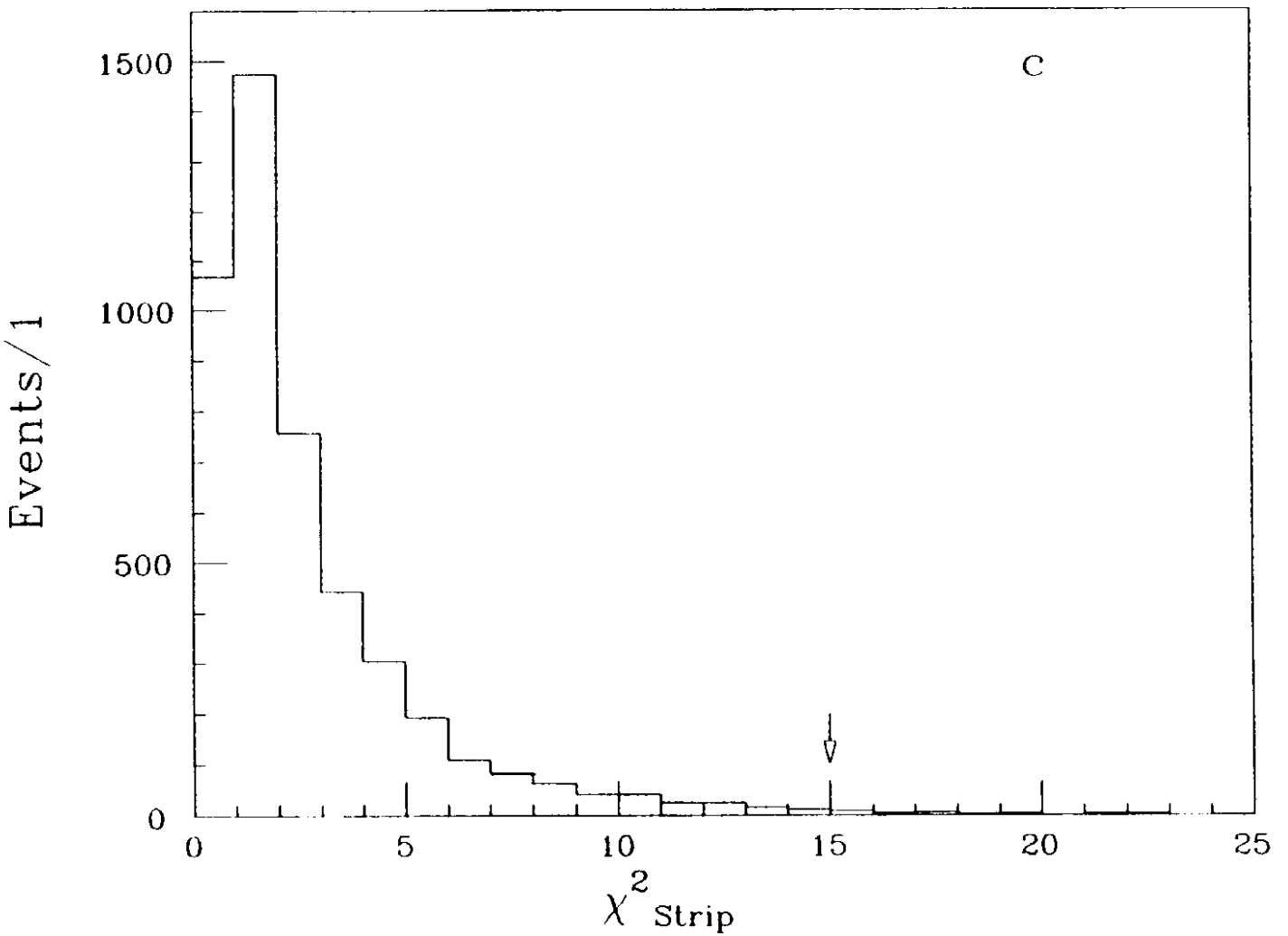
C
1500
1000
500
0
Events/1
0
5
10
15
20
25
χ^2_{Strip}

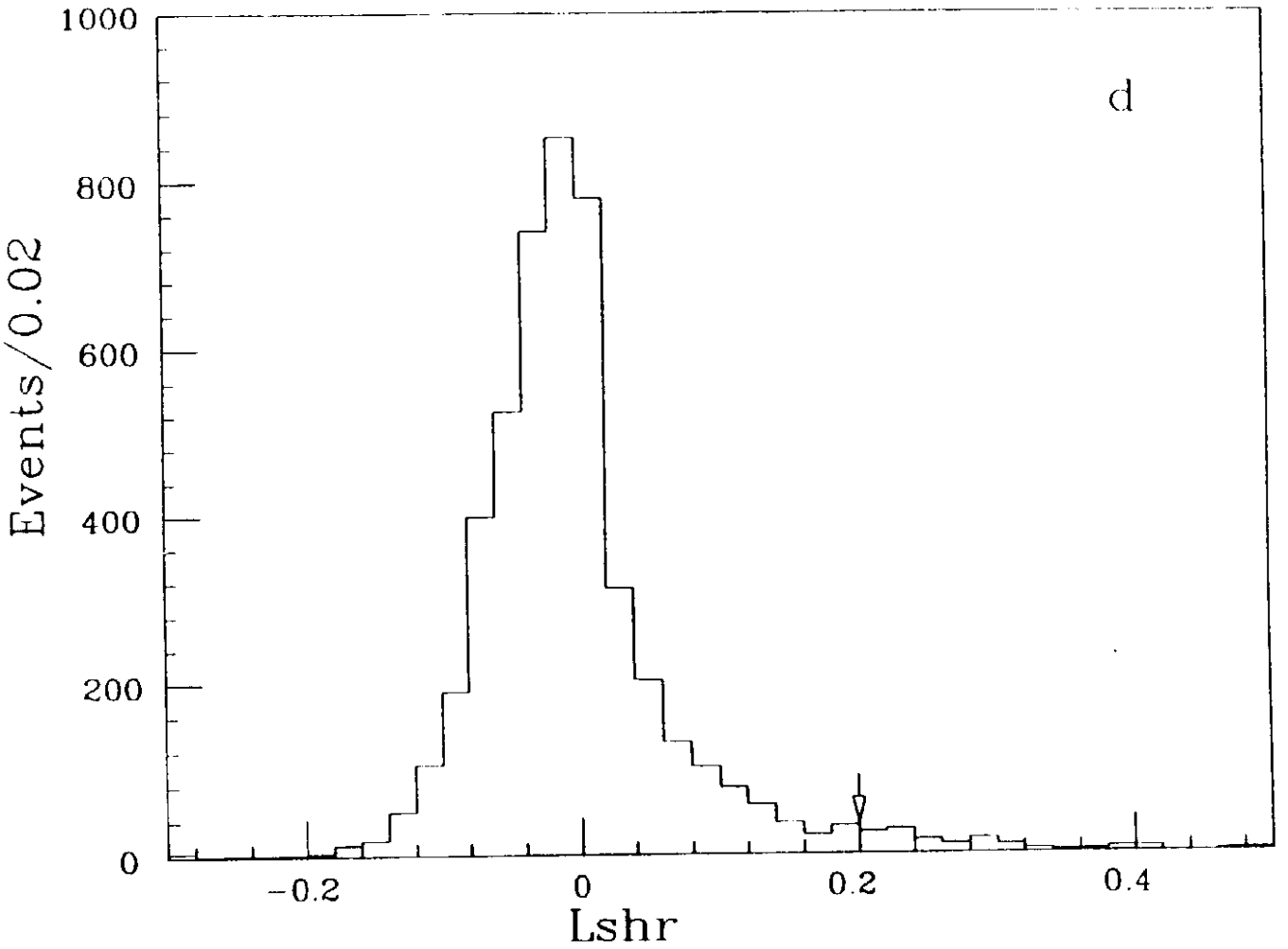
1000
800
600
400
200
0
Events/0.02
d
−0.2
0
0.2
0.4
Lshr

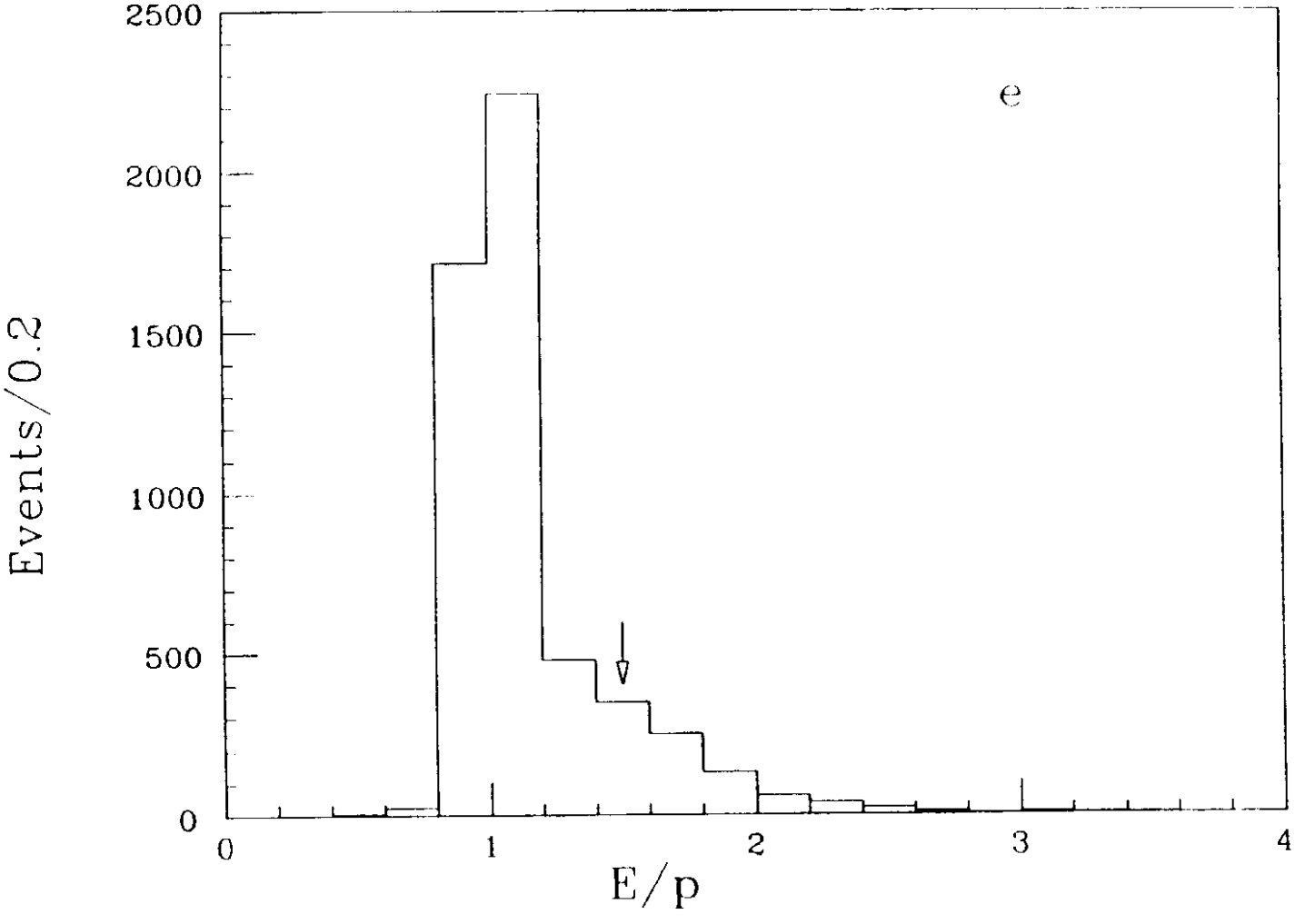
2500
2000
1500
1000
500
0
Events/0.2
0
1
2
3
4
E/p
e

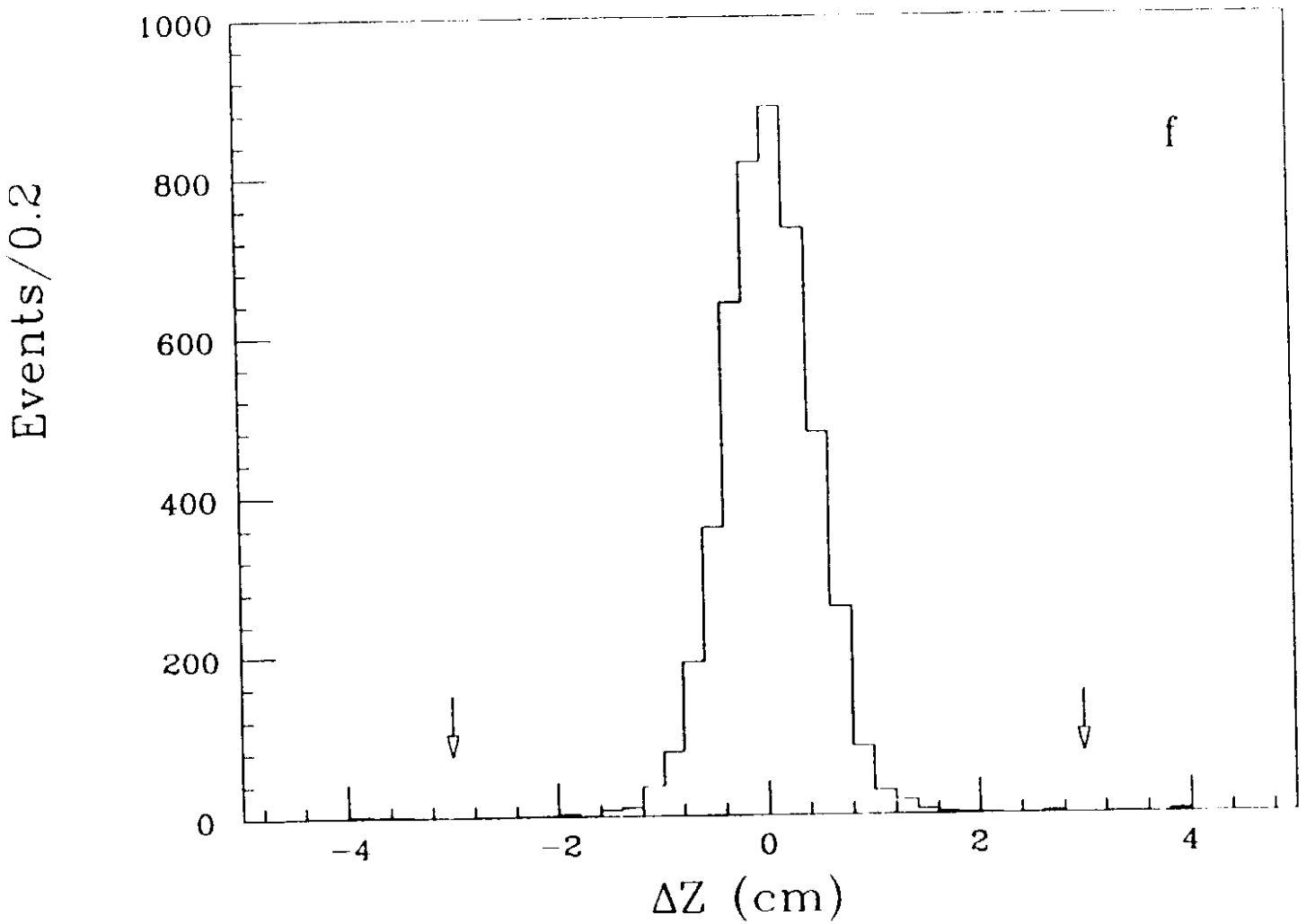
1000
800
600
400
200
0
Events/0.2
f
−4
−2
0
2
4
ΔZ (cm)

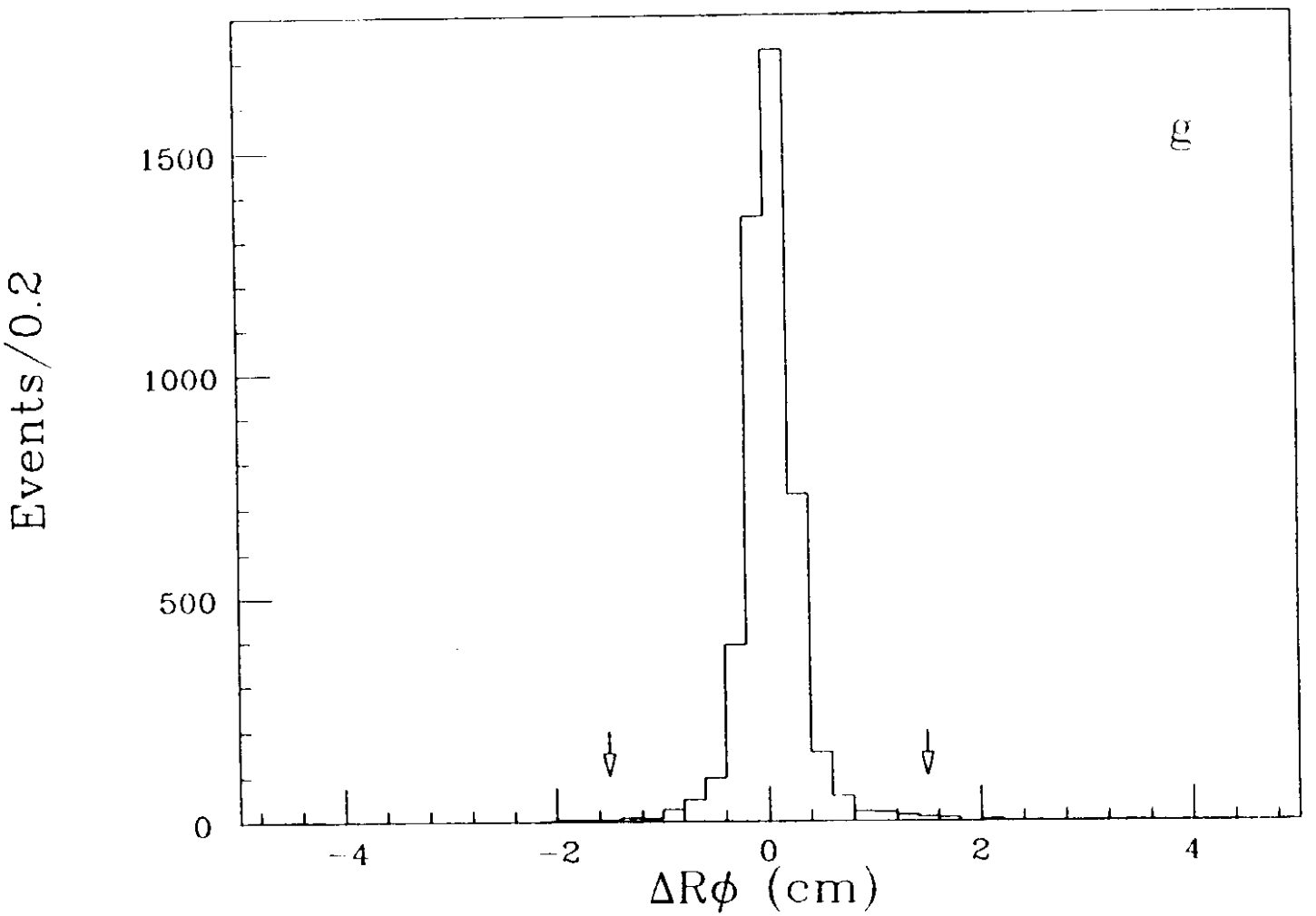
g
1500
1000
500
0
Events/0.2
−4
−2
0
2
4
ΔRφ (cm)

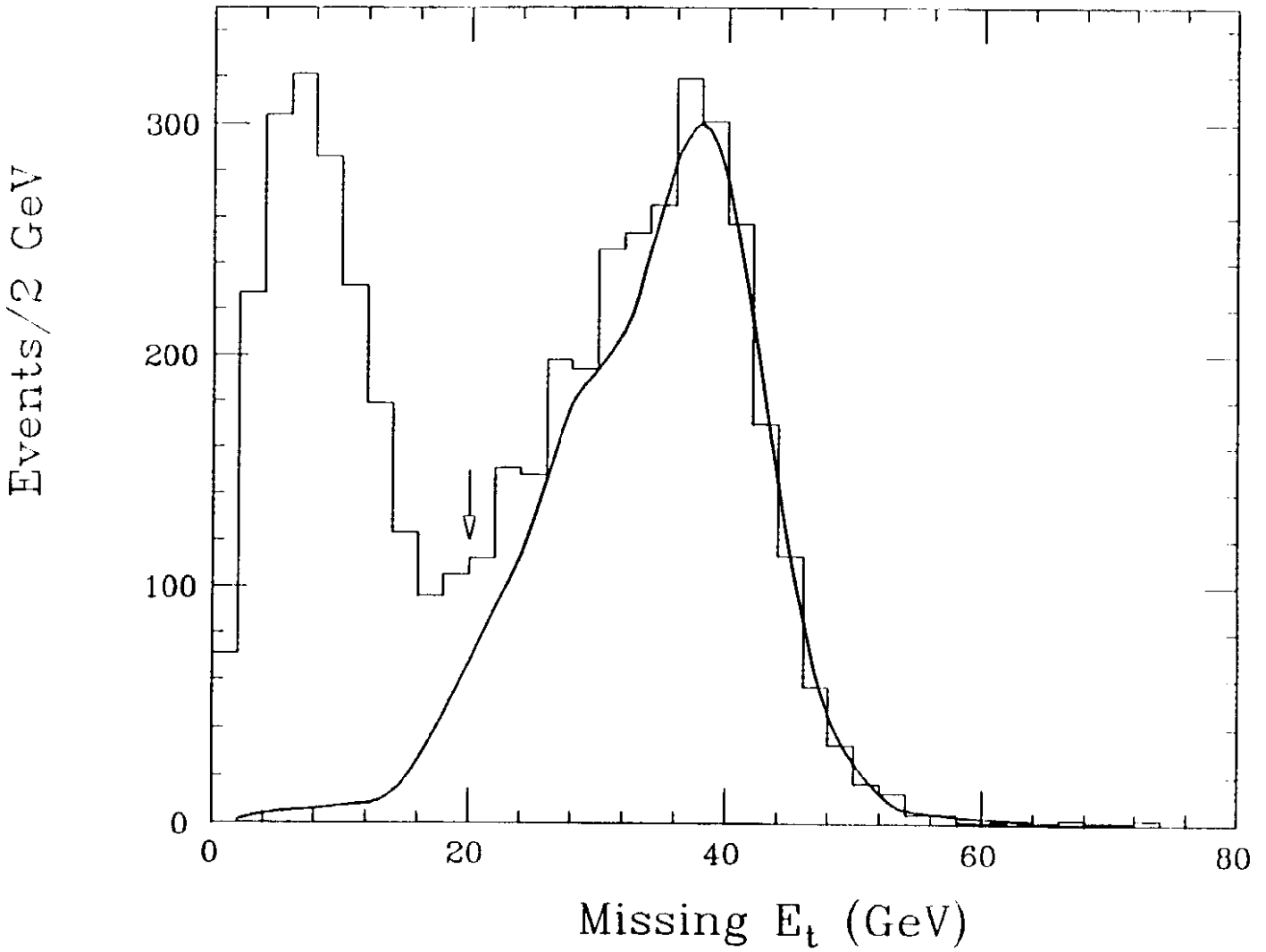

Figure 5: The $\not\!\!E_T$ distribution for events in the good central electron sample. The curve is a Monte Carlo prediction for W events with an electron with $E_T > 20$ GeV in the central fiducial region. We require $\not\!\!E_T > 20$ GeV for the W sample.

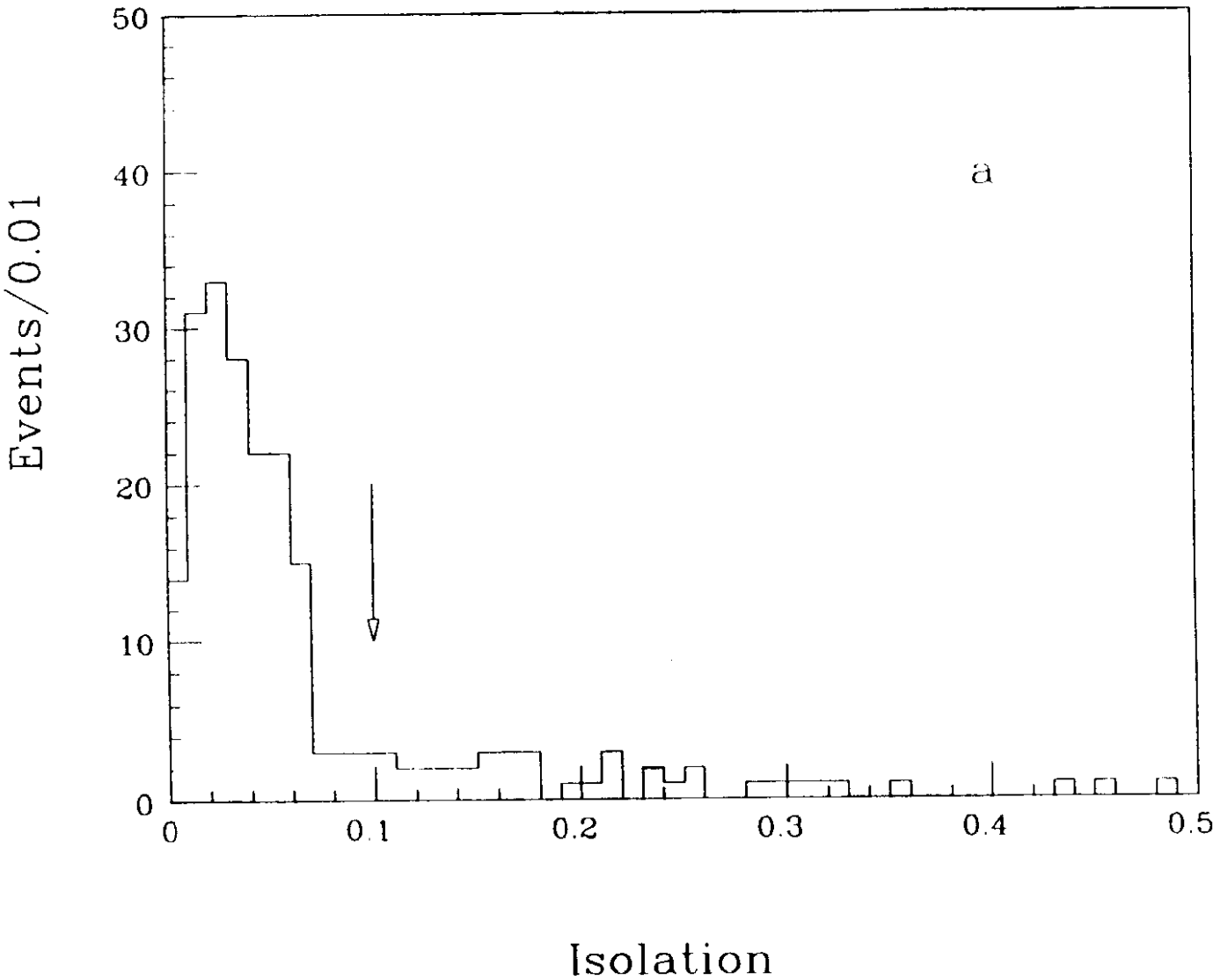

Figure 6: Distributions of the variables used in the second electron selection. These are the distributions after all cuts but the one plotted have been applied. The arrows represent the cut values.

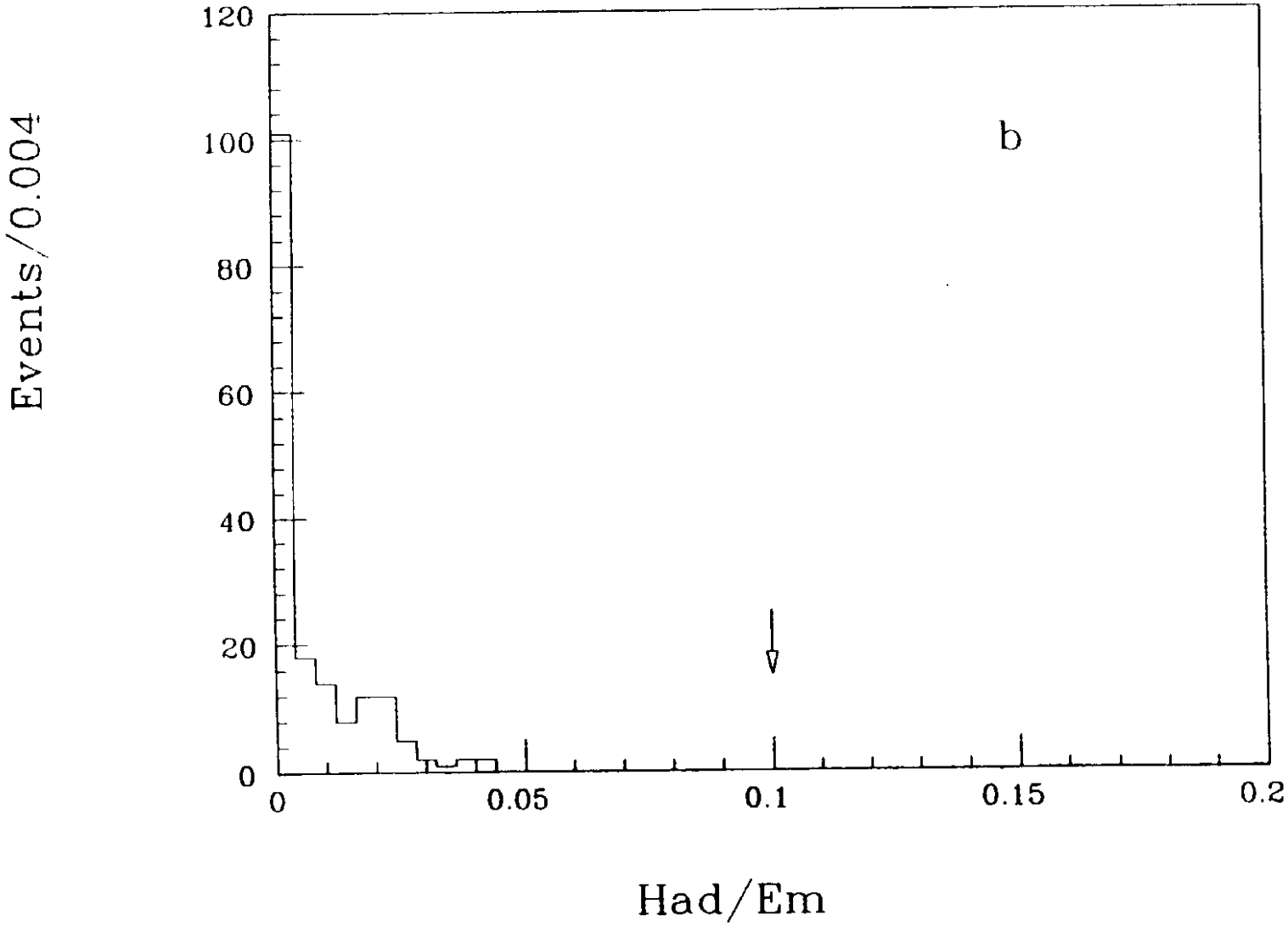
Events/0.004
120
100
80
60
40
20
0
0
0.05
0.1
0.15
0.2
b
Had/Em

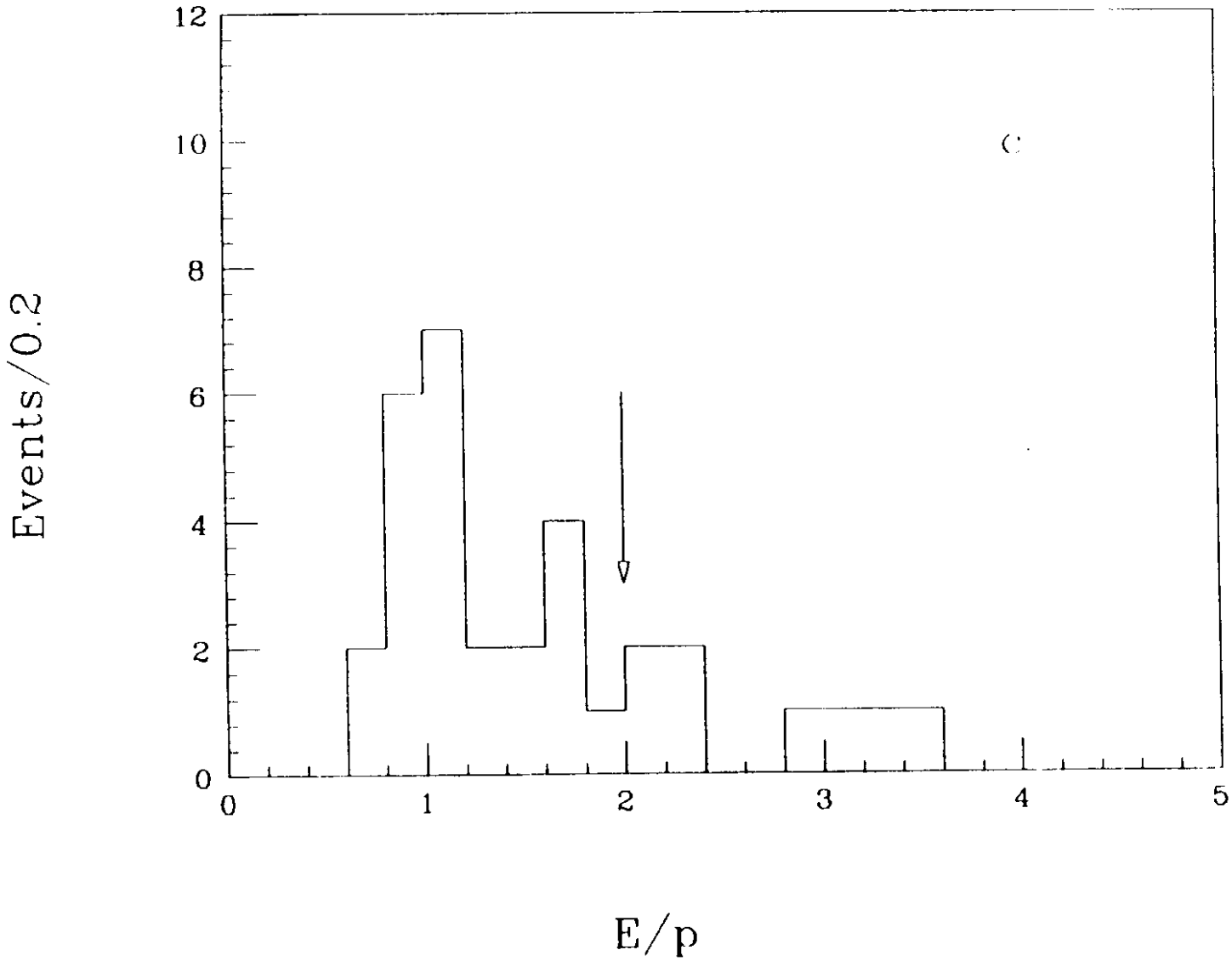
Events/0.2
E/p
0
2
4
6
8
10
12
0
1
2
3
4
5

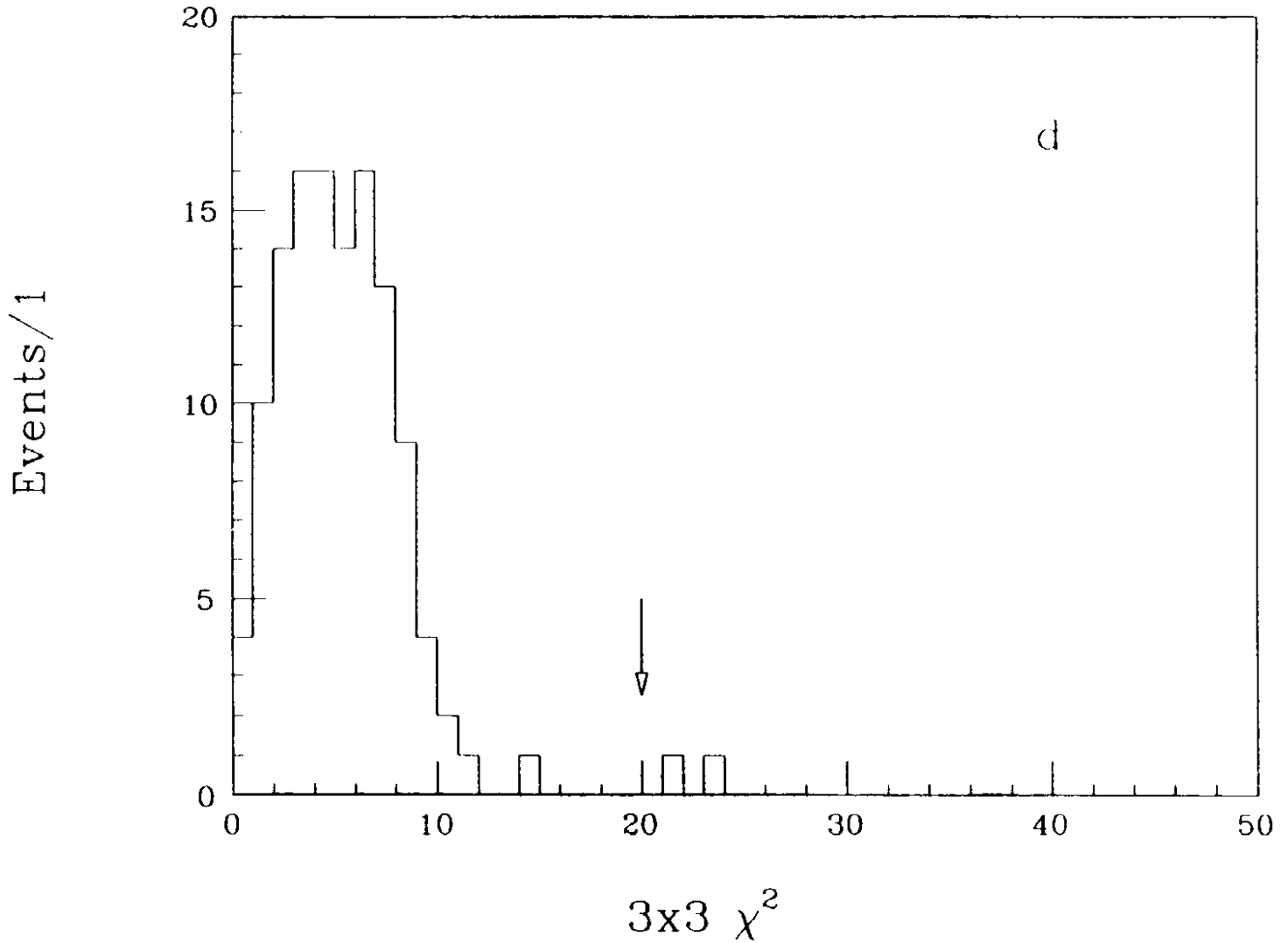
d
Events/1
3x3 χ^2
0
5
10
15
20
0
10
20
30
40
50

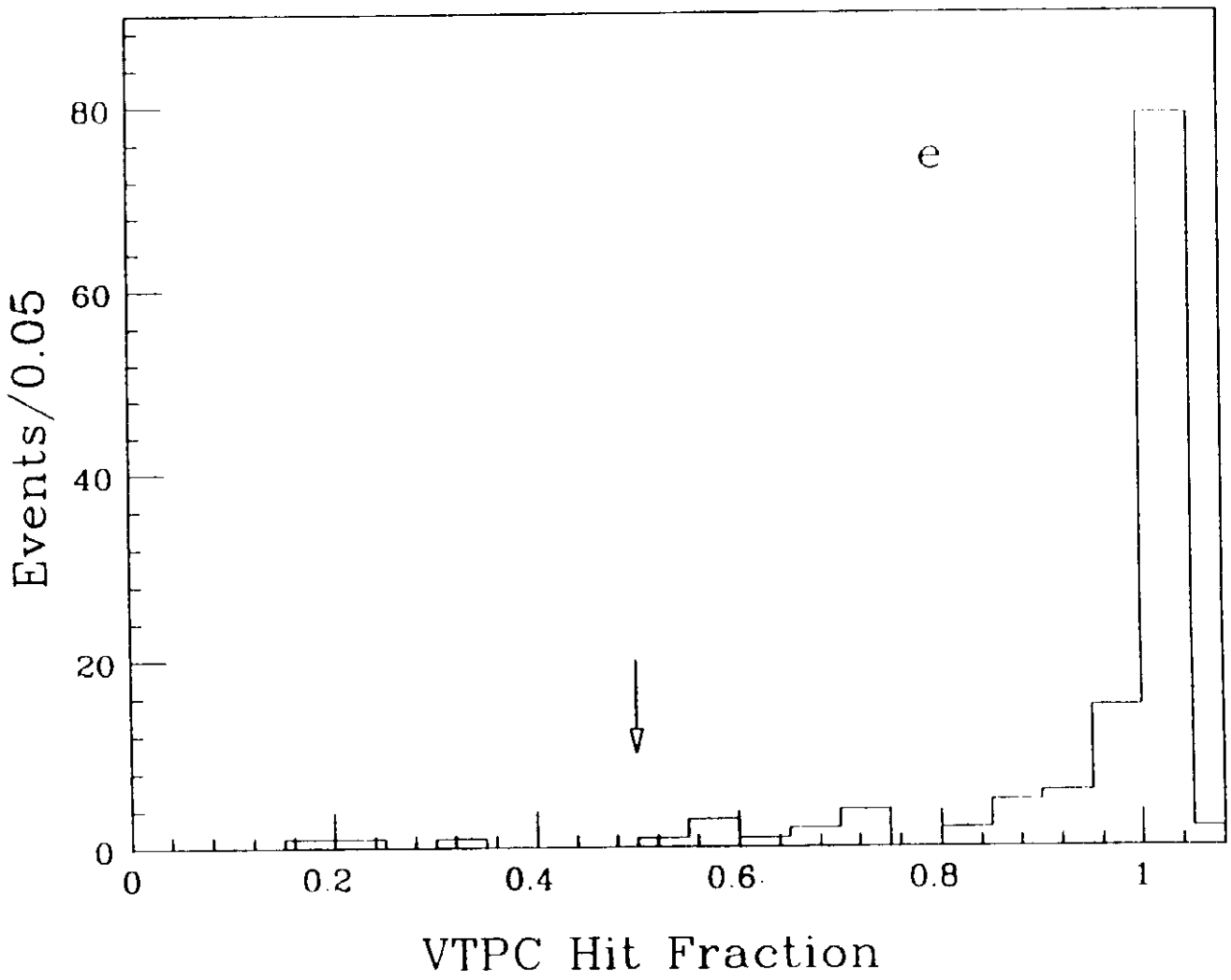
e
Events/0.05
80
60
40
20
0
0
0.2
0.4
0.6
0.8
1
VTPC Hit Fraction

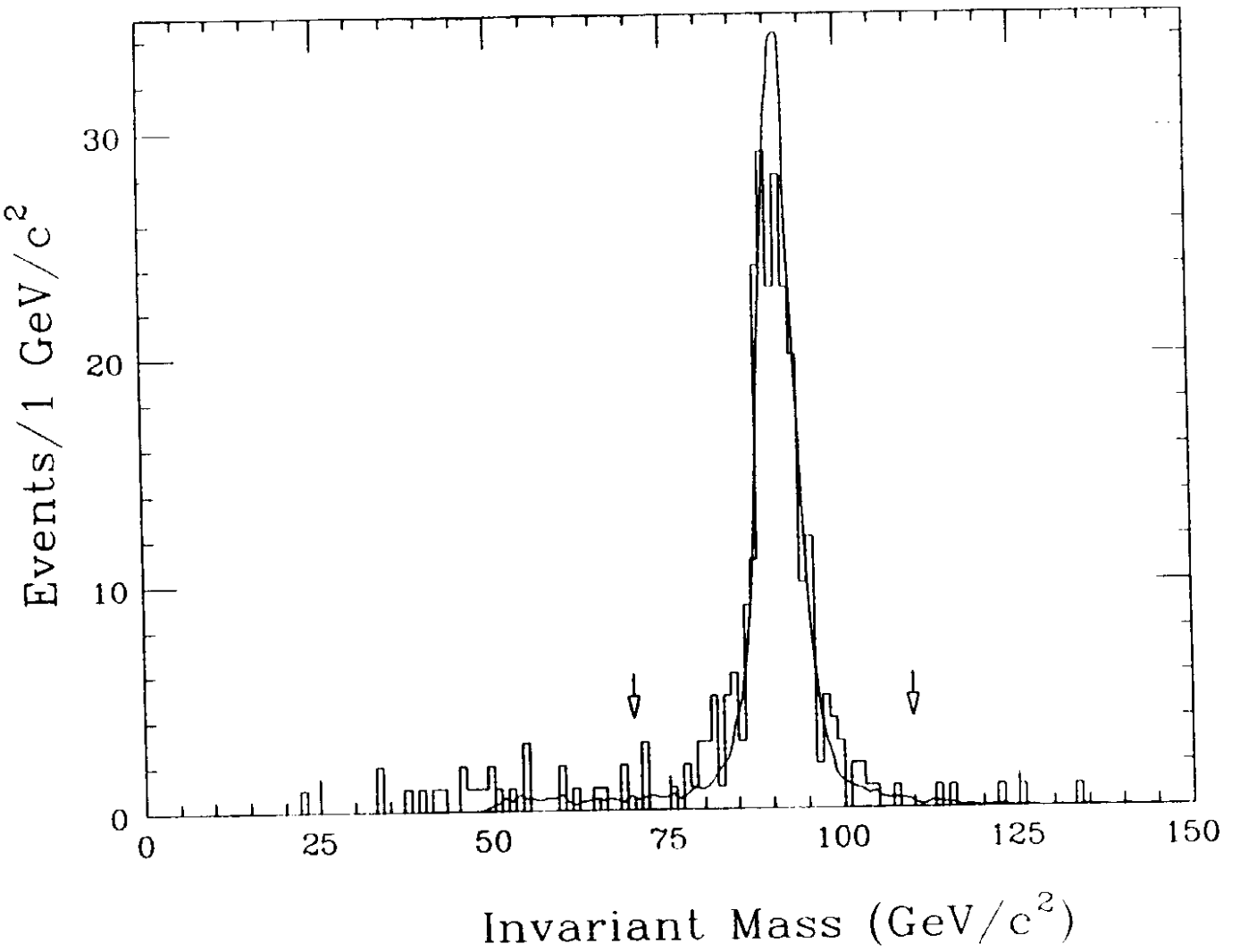

Figure 7: Invariant mass distribution for events with two electrons. In the Z^0 selection, we require the mass be in the window 70 - 110 GeV/c^2. The curve is from a $Z^0 + \gamma$ Monte Carlo between 50 - 150 GeV/c^2 with resolution effects (but no radiation effects) included.

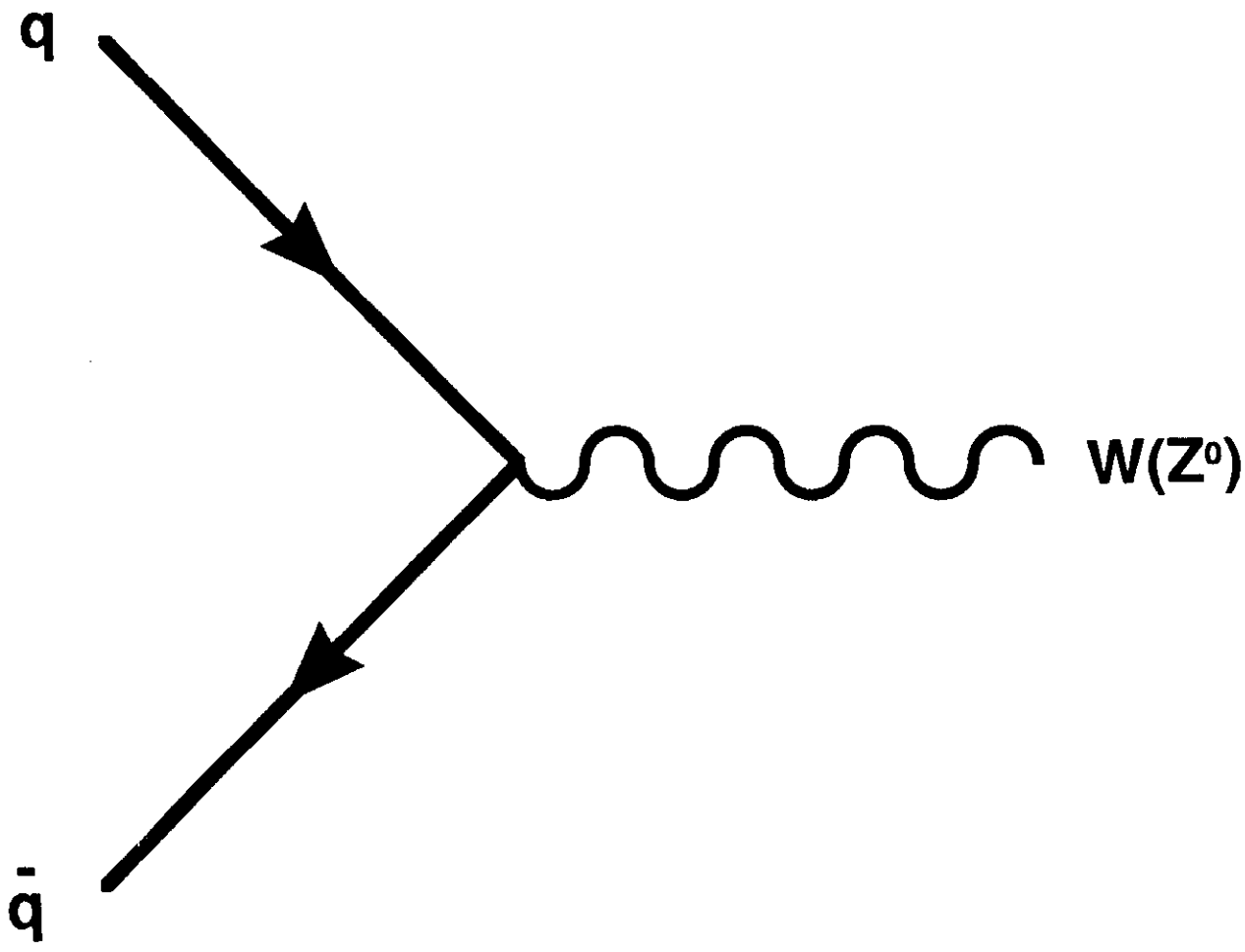

Figure 8: One quadrant of the CDF detector in η - ϕ space. The good fiducial regions for electrons are shaded.

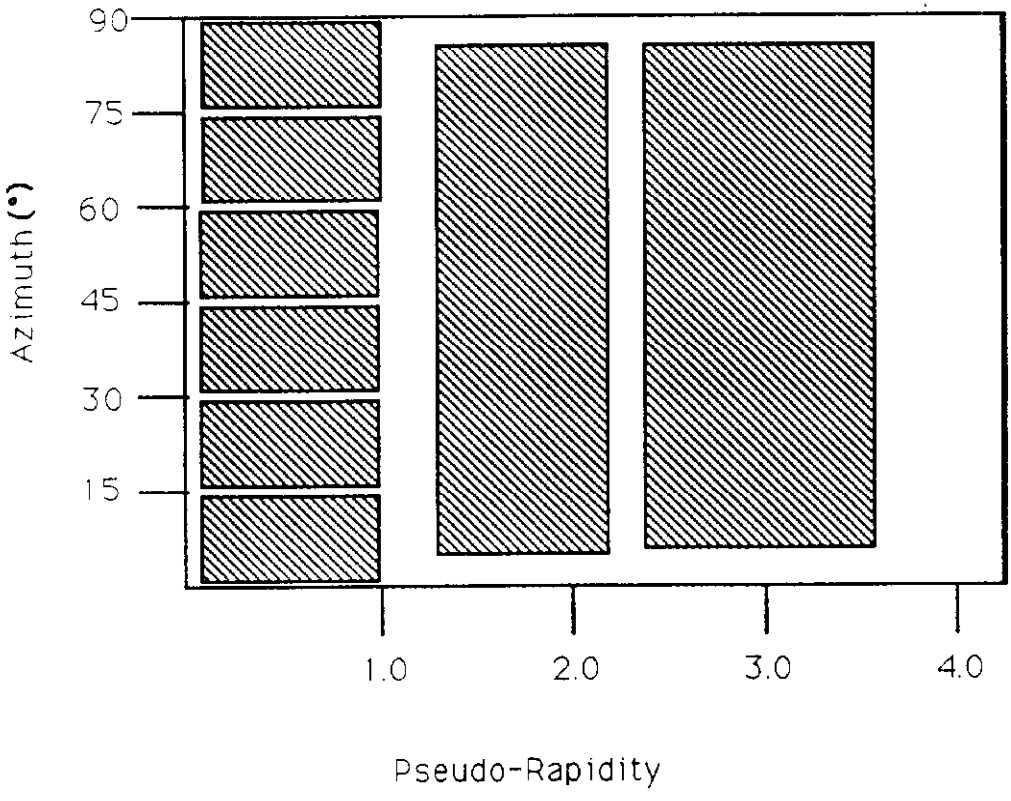

Figure 9: Feynman diagram used to generate W and Z^0 bosons in the zeroth order Monte Carlo.

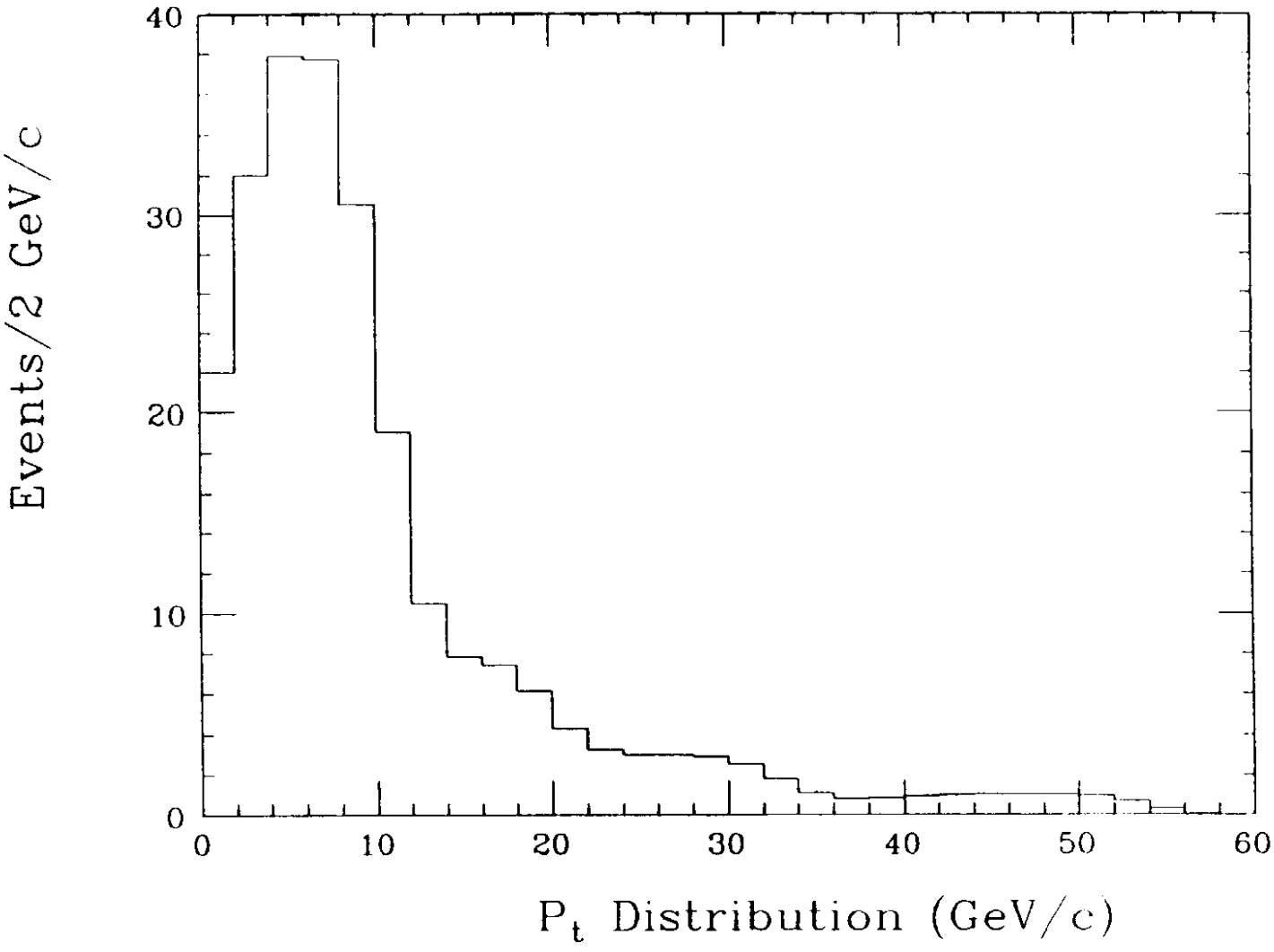

Figure 10: P_T distribution input to the zeroth order Monte Carlo.

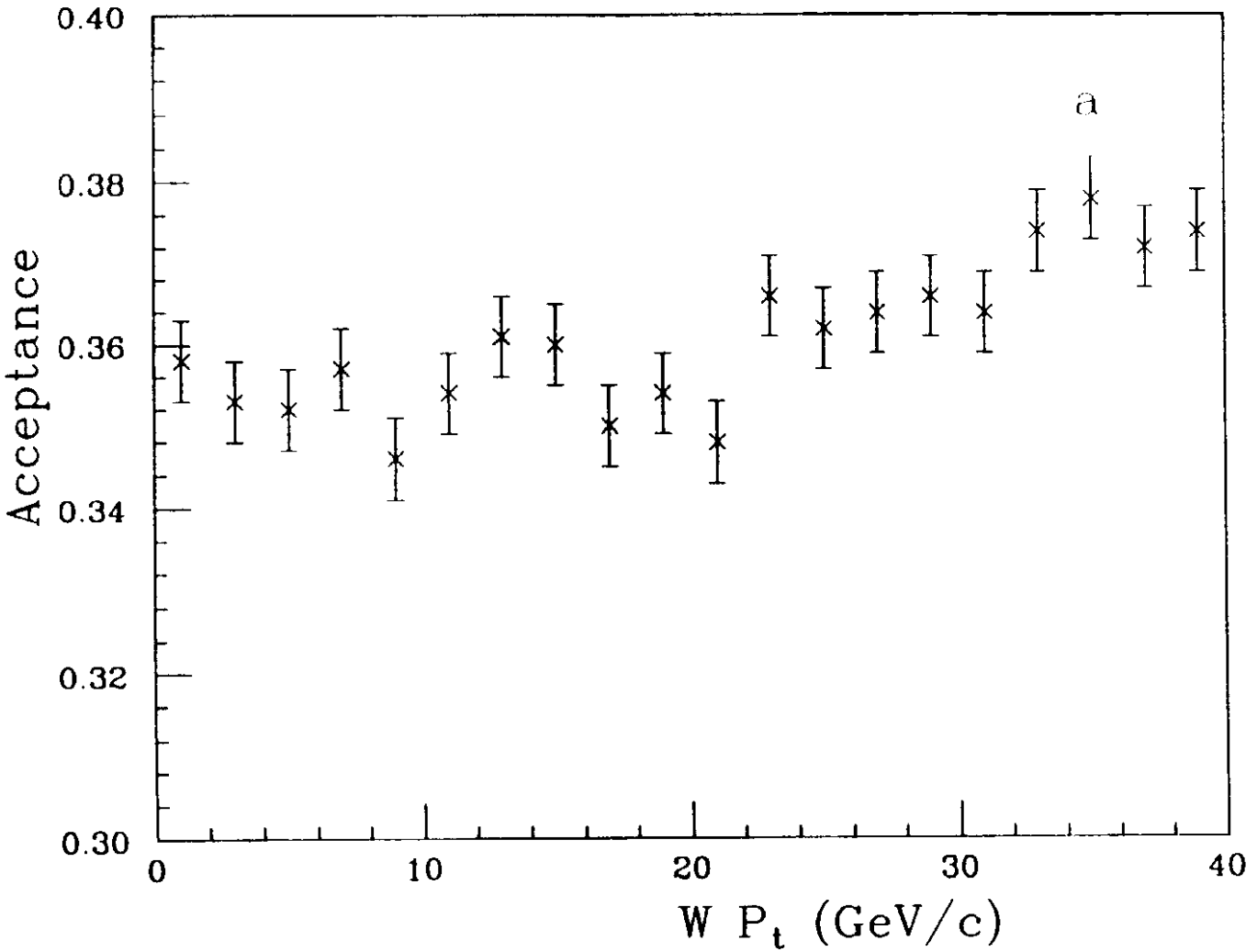

Figure 11: Example Feynman diagrams used to generate W and Z^0 bosons in the higher order Monte Carlo.

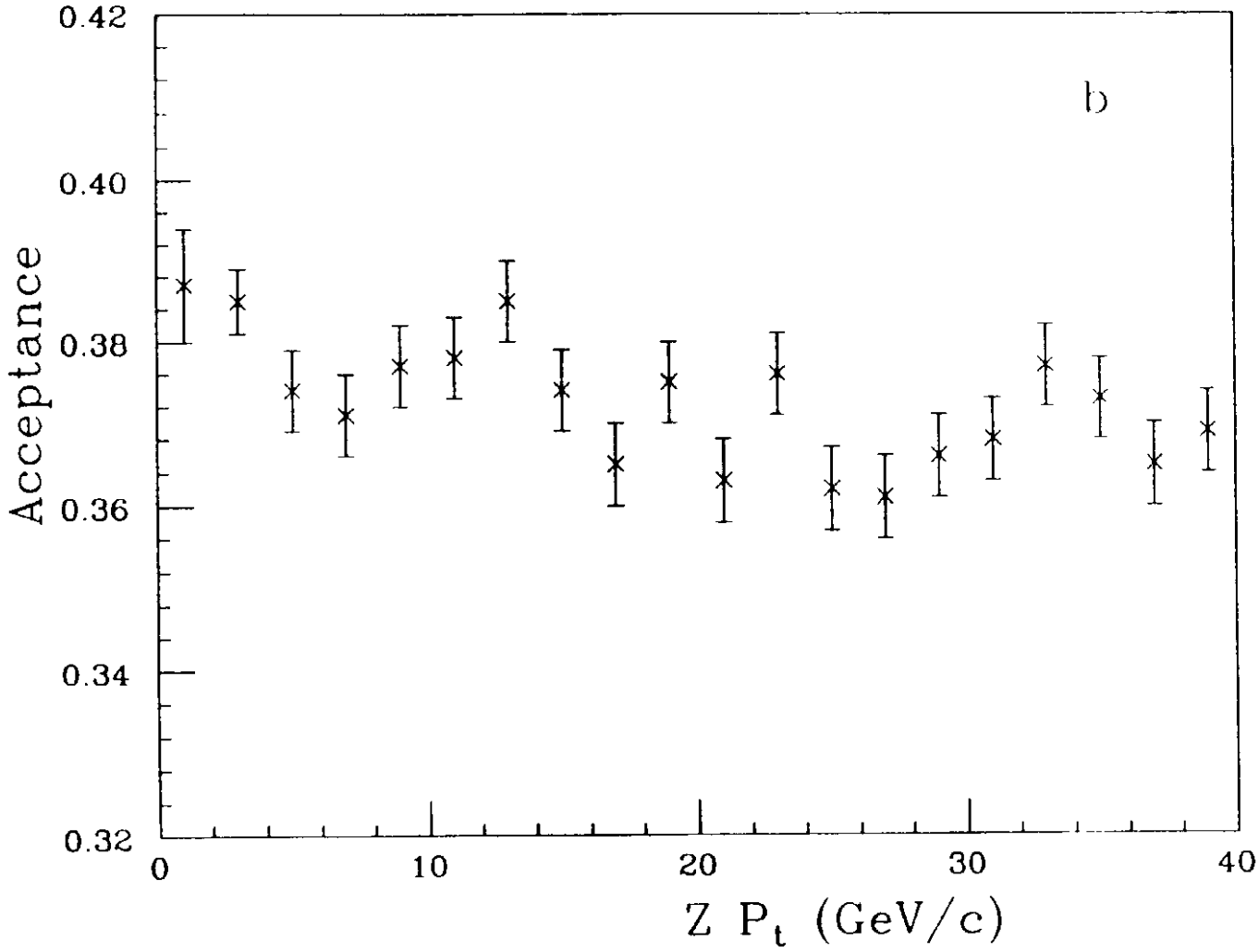
0.42
0.40
0.38
0.36
0.34
0.32
Acceptance
b
0
10
20
30
40
Z P_t (GeV/c)

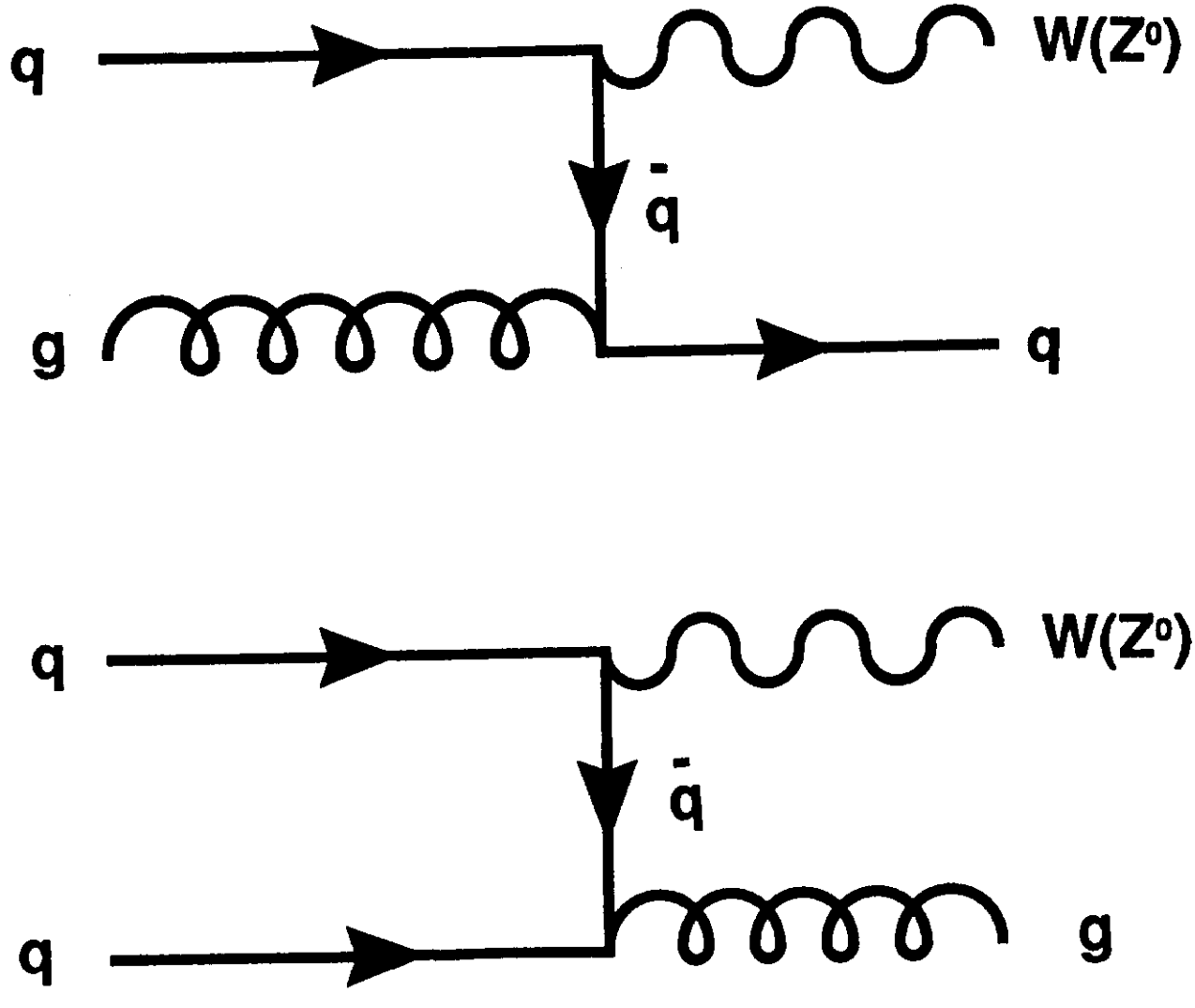

Figure 12: The acceptance for W and Z^0 events as a function of the boson p_T. The majority of the data has $p_T < 20.0$ GeV/c.

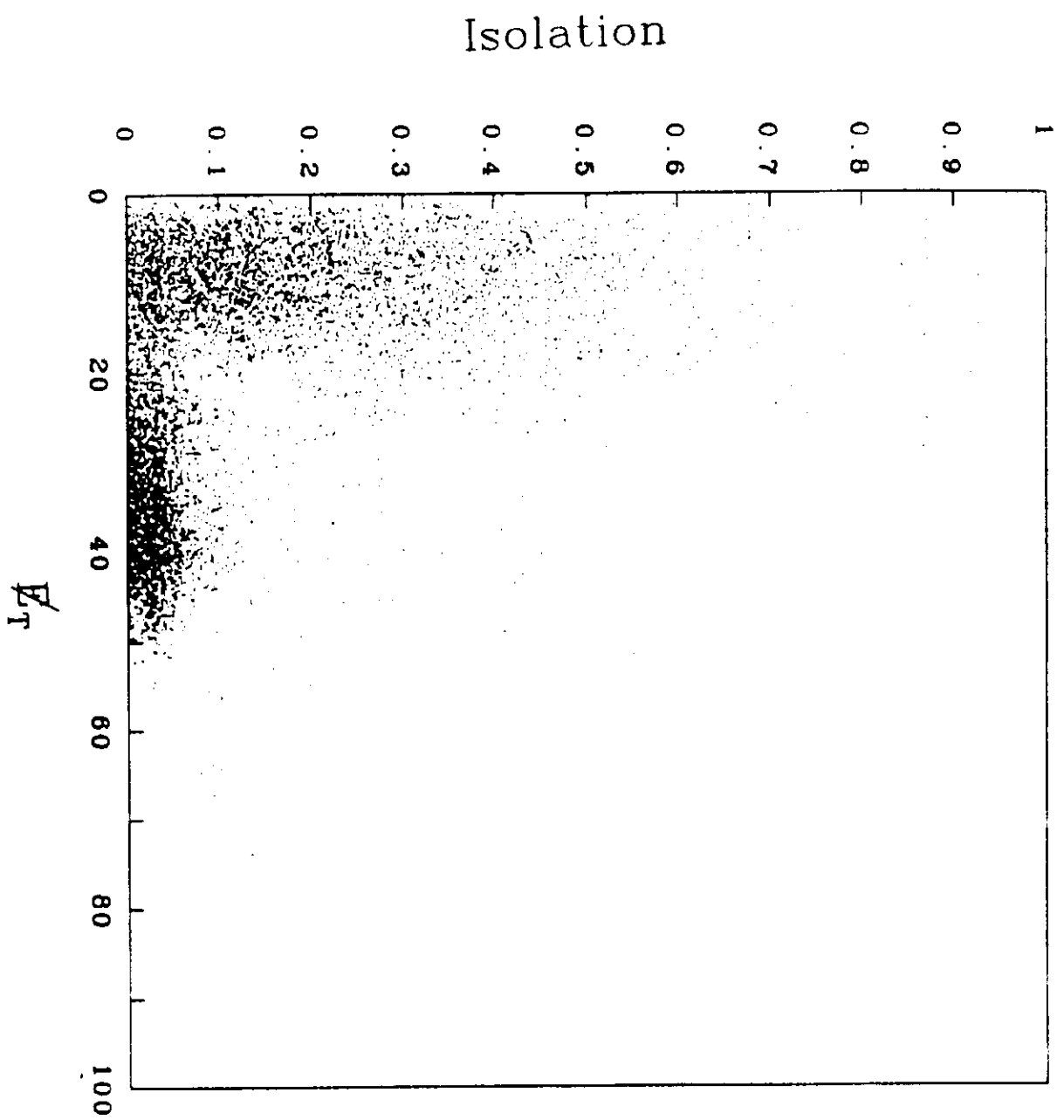

Figure 13: $\not\!\!E_T$ vs. *Iso* for the common central electron sample, where we have not used an *Iso* requirement. The clustering with $\not\!\!E_T > 20$ GeV and $Iso < 0.1$ is the W sample.

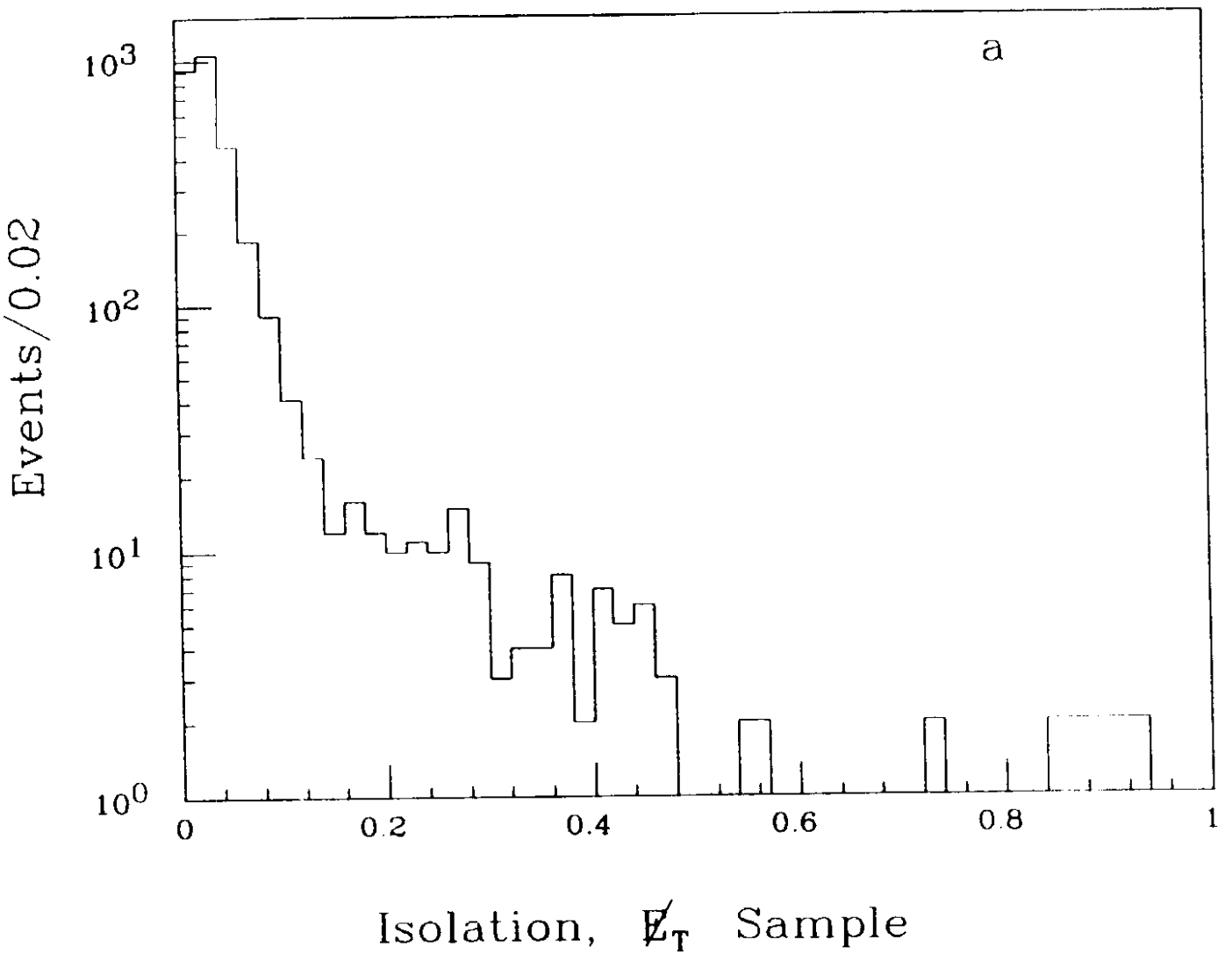

Figure 14: Isolation distributions for the samples used in estimating the W background. (a) is for the $\not\!\!E_T > 20$sample, (b) is for control sample 1, and (c) is for control sample 2.

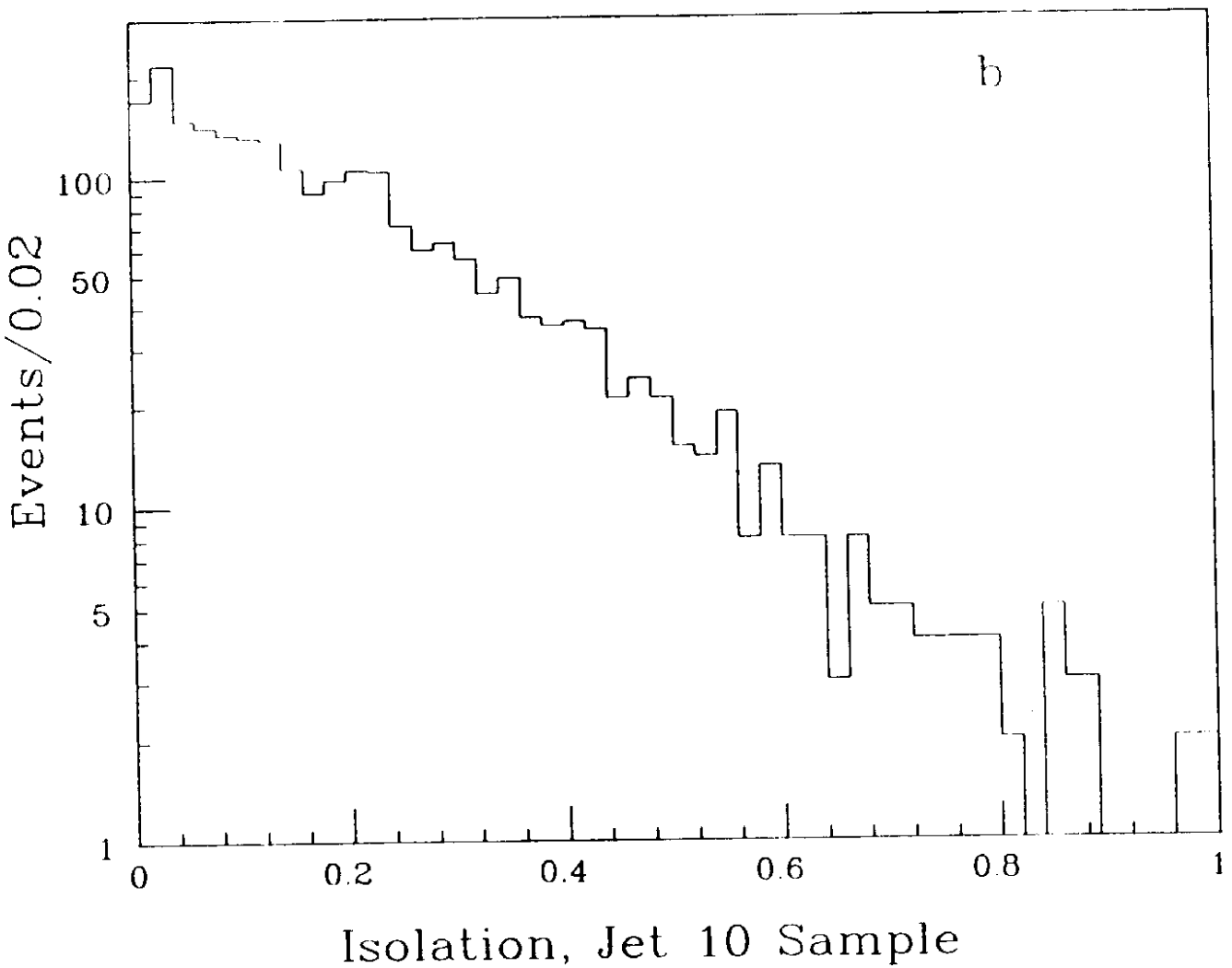
b
Events/0.02
100
50
10
5
1
0
0.2
0.4
0.6
0.8
1
Isolation, Jet 10 Sample

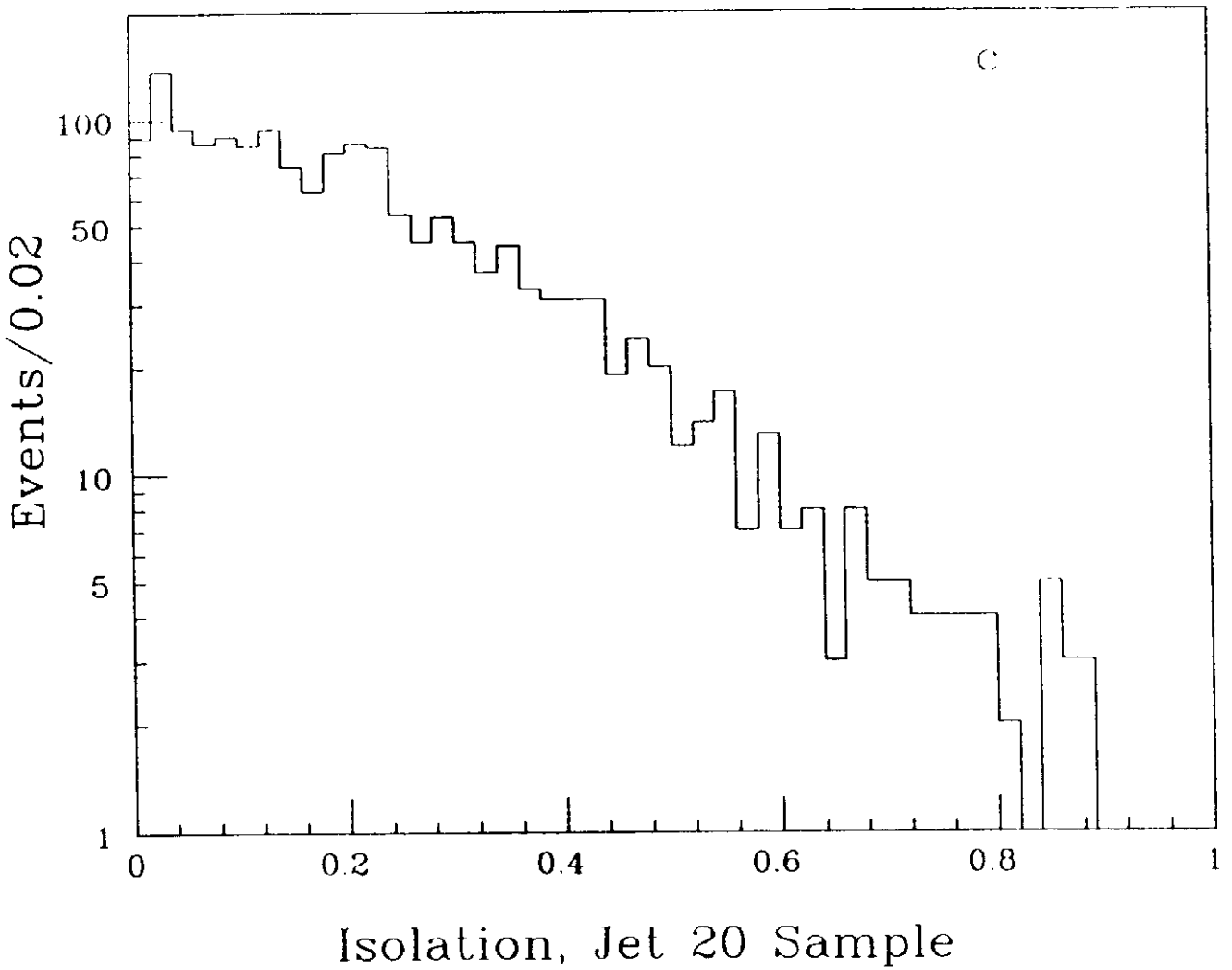
C
100
50
10
5
1
Events/0.02
0
0.2
0.4
0.6
0.8
1
Isolation, Jet 20 Sample

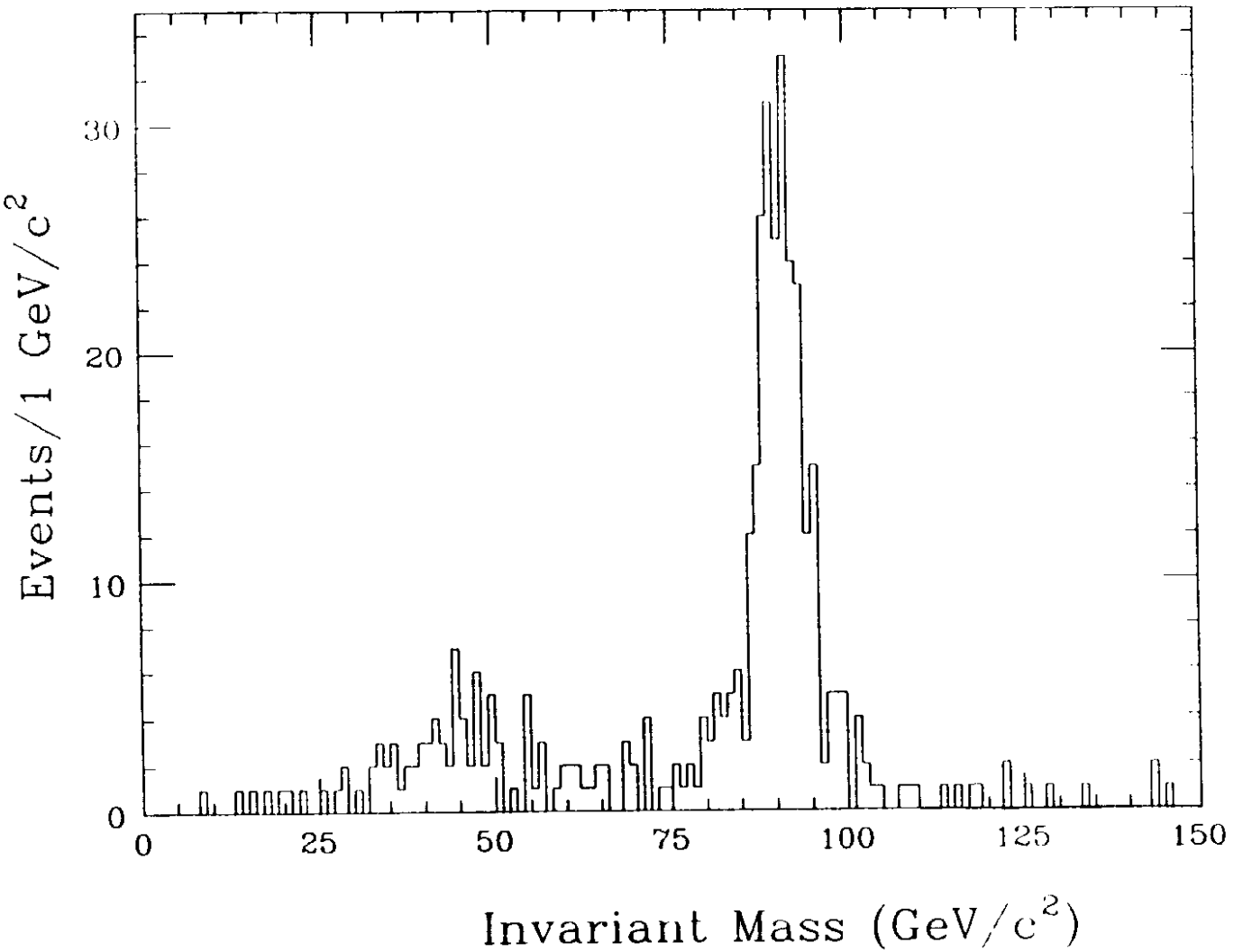

Figure 15: Invariant mass distribution for events with two electron candidates passing all but the *Iso* requirements.

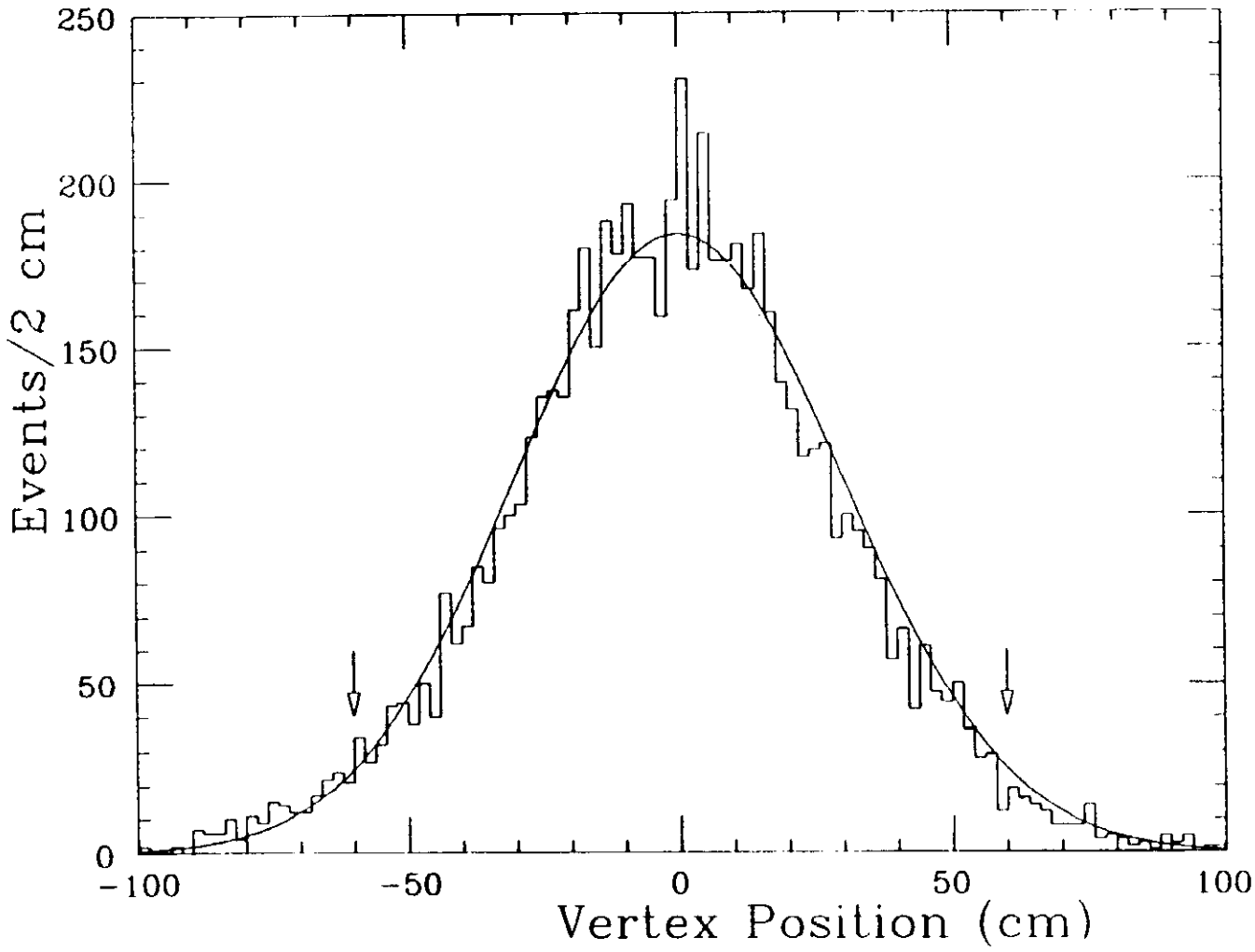

Figure 16: The vertex distribution for central electron clusters. The curve is a Gaussian with mean = 0 and σ = 30 cm, normalized to the same area.

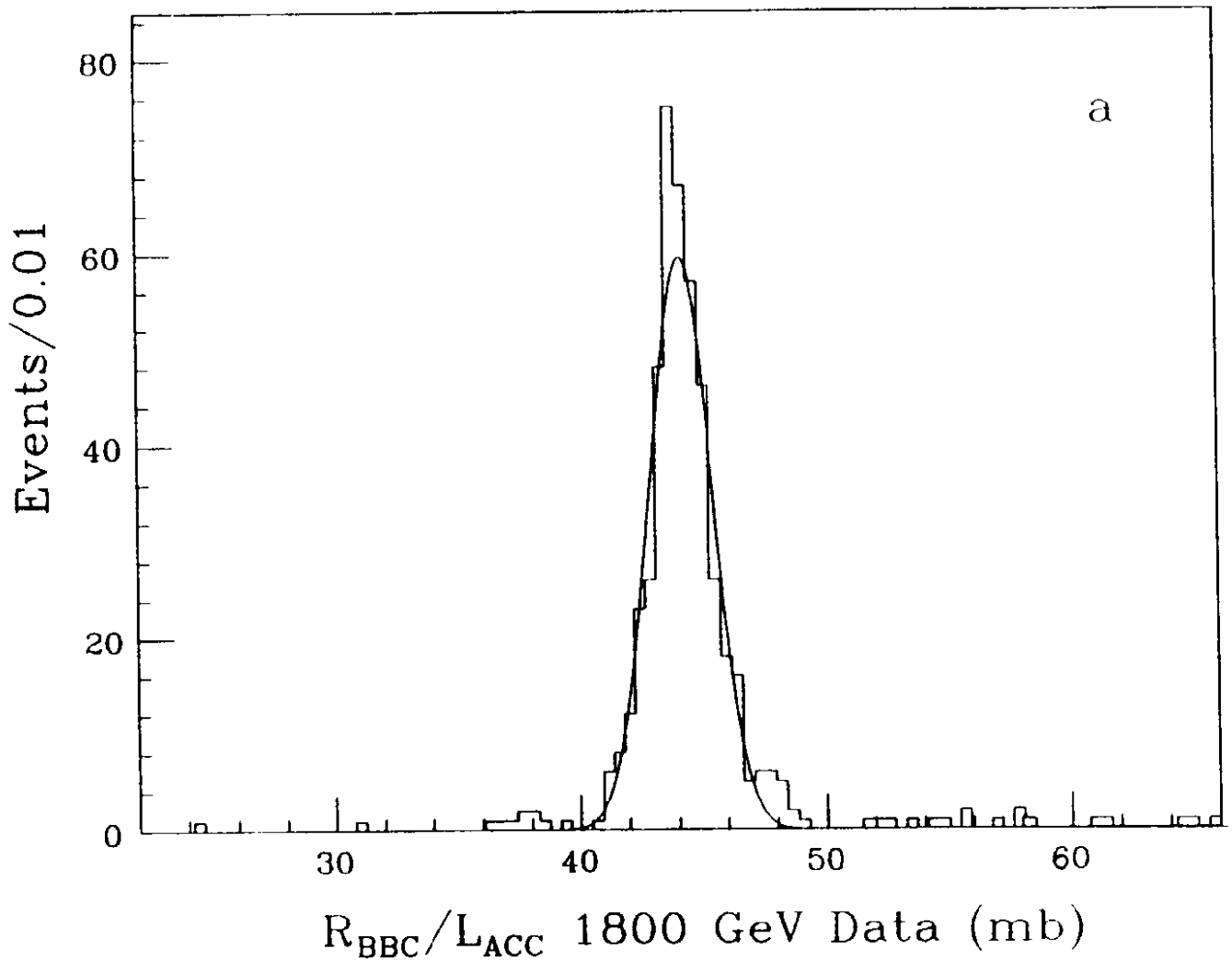

Figure 17: (a) Distribution of $\frac{R_{BBC}}{L_{acc}}$ for $\sqrt{s} = 1800$ GeV. The curve is a fitted Gaussian with $\bar{x} = 44.16$ mb and $\sigma = 1.28$ mb. (b) Distribution of $\frac{R_{BBC}}{L_{acc}}$ for $\sqrt{s} = 546$ GeV. The curve is a fitted Gaussian with $\bar{x} = 33.17$ mb and $\sigma = 0.30$ mb.

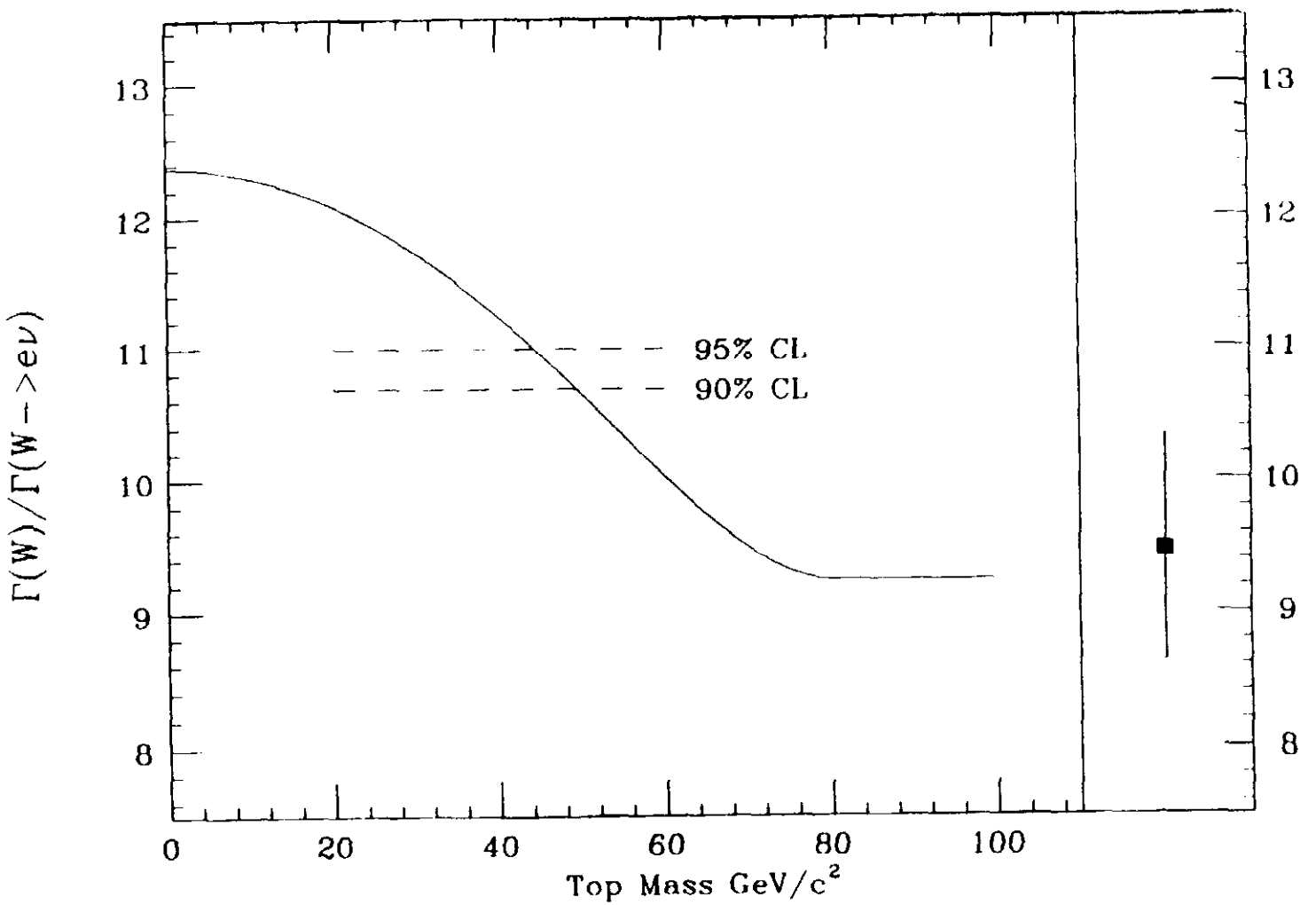

Figure 22: The predicted value for $\Gamma(W)/\Gamma(W \rightarrow e\,\nu)$ as a function of the top-quark mass for $M_W = 80.0$ GeV/c^2 and $\alpha_s = 0.13$. The value calculated from equation 13 with 90% and 95% C.L. limits is shown. We use this ratio since it depends only weakly on the W mass.

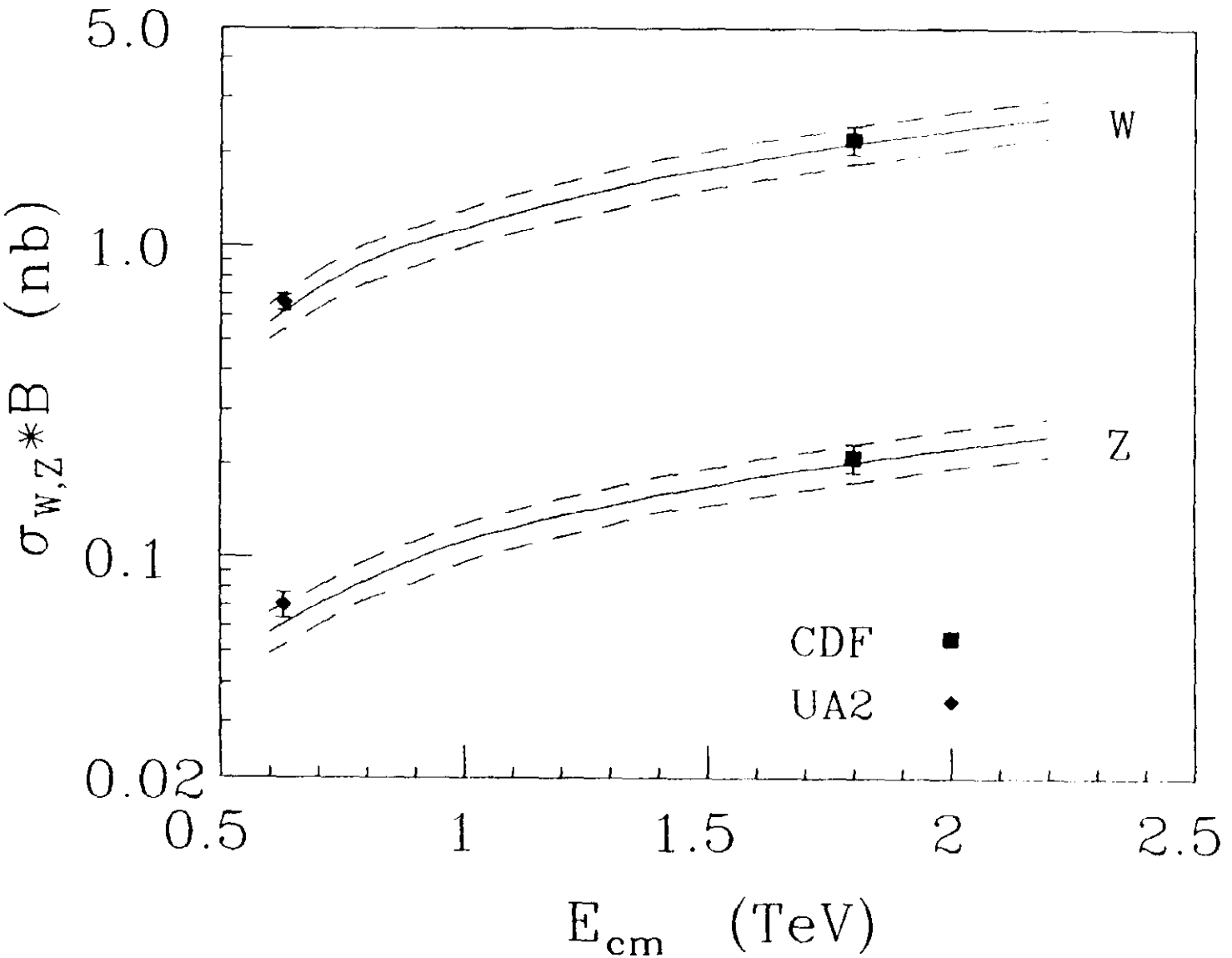

Figure 21: Comparison of experimental measurements with theoretical predictions [49]. The dashed lines indicate the 1σ error limits for the theoretical curve. Recent measurements by the UA2 collaboration are also plotted [50].

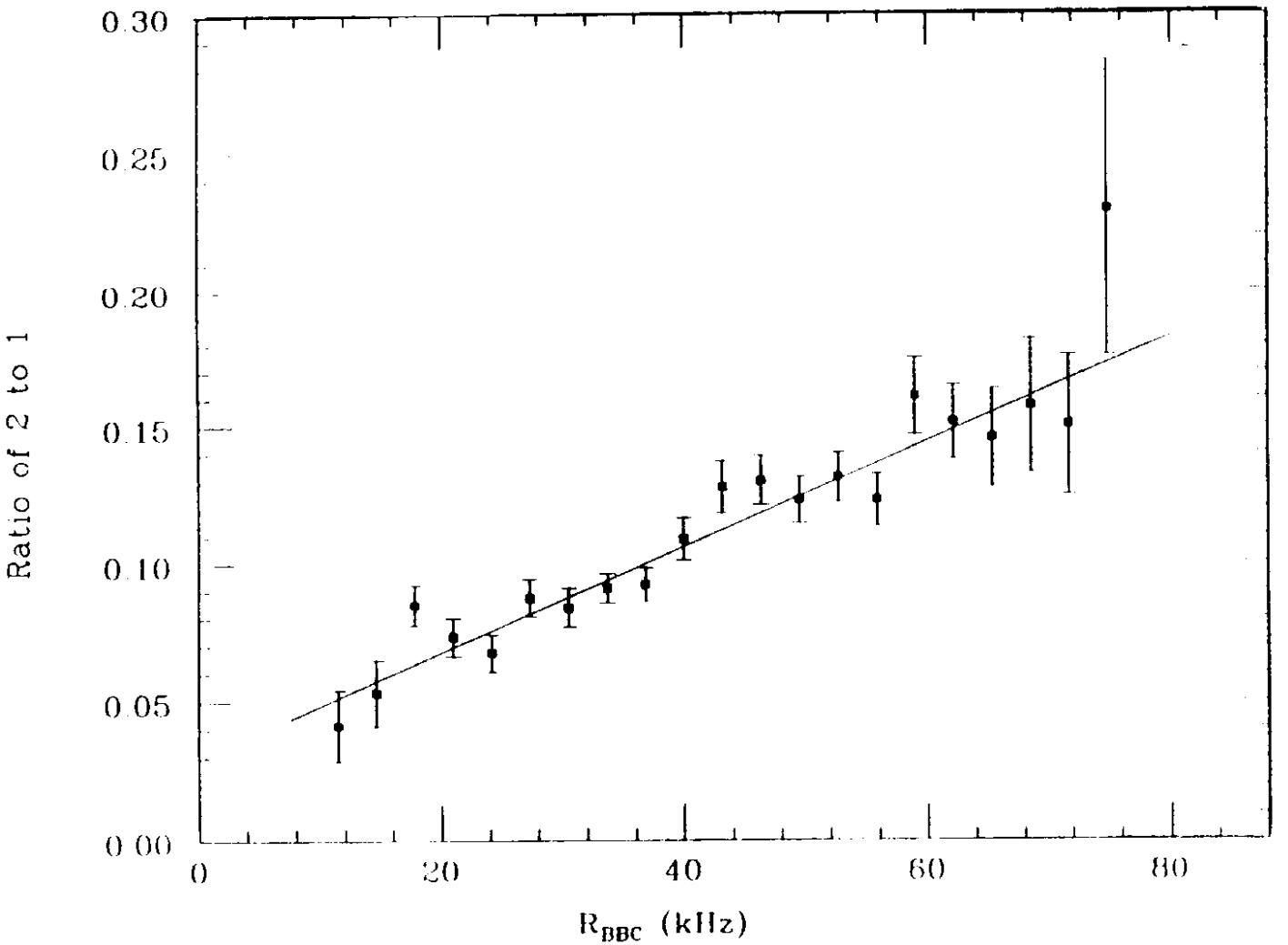

Figure 20: The ratio of events with 2 vertices to events with 1 vertex as a function of R_{BBC}. The number of events with 2 vertices has been corrected for vertex finding inefficiencies.

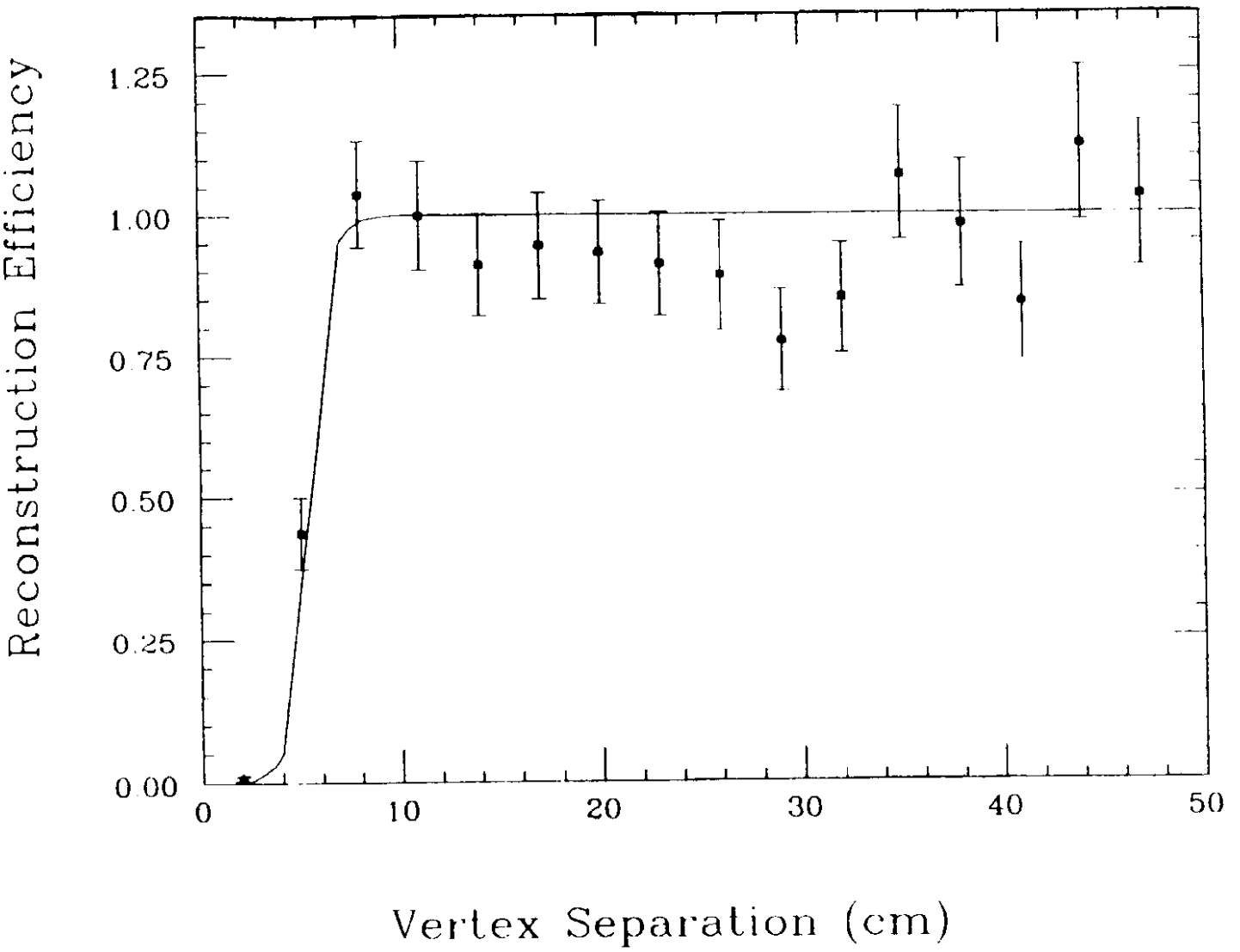

Figure 19: The secondary vertex finding efficiency as a function of vertex separation.

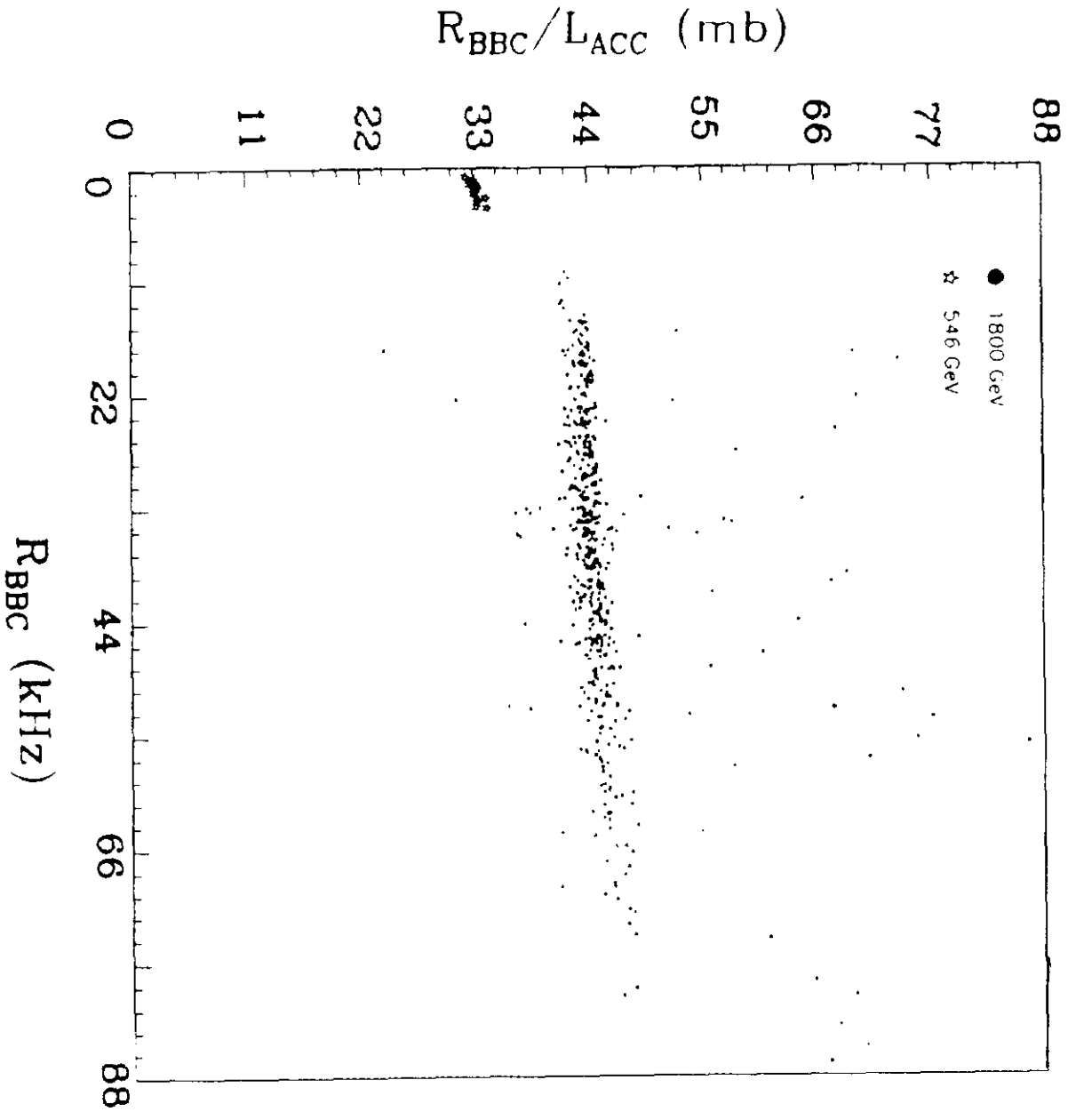

Figure 18: The ratio $\frac{R_{BBC}}{L_{acc}}$ as a function of the instantaneous luminosity. Data from accelerator fills with $\sqrt{s} = 546$ GeV and $\sqrt{s} = 1800$ GeV are plotted, with the 546 GeV data the cluster at the lower left.

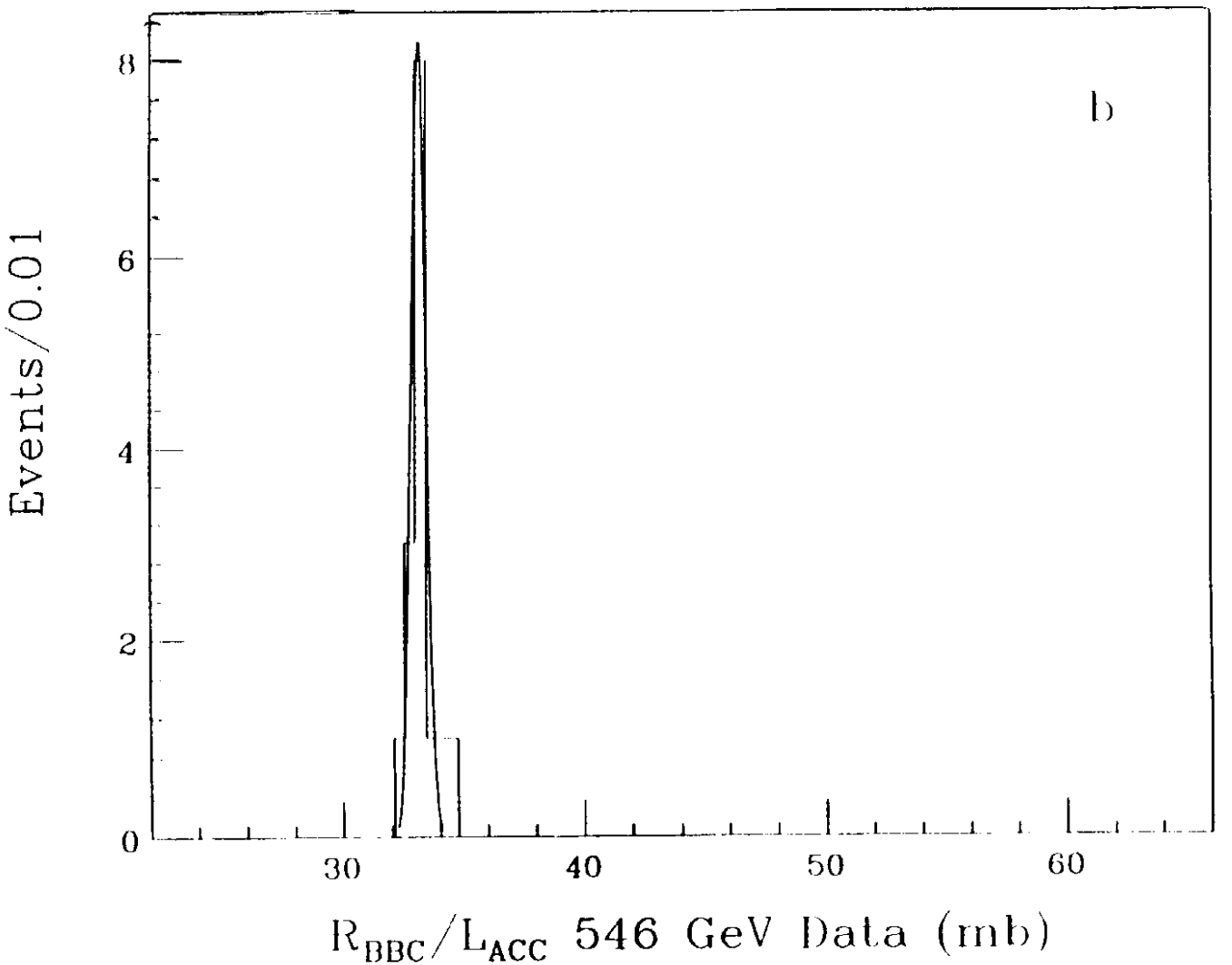
b
Events/0.01
0
2
4
6
8
30
40
50
60
R_{BBC}/L_{ACC} 546 GeV Data (mb)